

1



2

CVD diamond applications for particle detection and identification in radiation-hard environments

3

4

5

6

Matevž Červ
Vienna University of Technology

7

8

A thesis submitted for the degree of
Doctor of technical sciences

9

10

Geneva 2016

¹¹ Contents

12	1 Introduction	1
13	1.1 Fundamental research	2
14	1.2 Research institutes	3
15	1.3 The Large Hadron Collider	6
16	1.4 The ATLAS experiment	7
17	1.5 Particle detectors	9
18	1.5.1 Semiconductor detectors	9
19	1.5.2 Diamond sensors	11
20	2 Signal formation in diamond	13
21	2.1 Principles of signal formation in semiconductors	14
22	2.1.1 Signal induction by moving charges	16
23	2.1.2 Shockley-Ramo theorem	17
24	2.1.3 Radiation-induced electrical pulses	18
25	2.1.4 Signal charge fluctuations	19
26	2.2 Carrier transport in a diamond sensor	19
27	2.3 Electronics for signal processing	23
28	2.3.1 Signal preamplifiers	23
29	2.3.1.1 Current-sensitive amplifier	23
30	2.3.1.2 Charge-sensitive amplifier	24
31	2.3.1.3 Analogue electronic noise	24
32	2.3.2 Analogue-to-digital converters	25
33	2.3.3 Digital signal processing	27
34	3 Diamond irradiation study	29
35	3.1 Measurement setup	30
36	3.1.1 Preamplifiers	30
37	3.1.1.1 Calibration	31
38	3.1.2 Diamond samples	32
39	3.1.3 Readout devices	33
40	3.1.4 Setup for the efficiency study using β particles	34
41	3.1.5 Room temperature α -TCT setup	34
42	3.1.6 Cryogenic α -TCT setup	35
43	3.2 Charged particle pulses and spectra	36

CONTENTS

44	3.3	Radiation limitations	38
45	3.3.1	Quantifying radiation damage in diamonds	39
46	3.3.1.1	Irradiation with a $\pi_{300 \text{ MeV}}$ beam	39
47	3.3.1.2	Charge collection efficiency and charge collection dis- tance	40
48	3.3.1.3	Irradiation damage factor	41
50	3.3.2	Long-term measurement stability	43
51	3.3.2.1	β long-term stability	43
52	3.3.2.2	α long-term stability	44
53	3.4	Temperature limitations	50
54	3.4.1	Temperature-variant α -TCT before irradiation	50
55	3.4.2	Temperature-variant α -TCT after irradiation	51
56	3.4.2.1	Collected charge as a function of temperature	53
57	3.4.2.2	Charge trapping	55
58	3.5	Conclusion	59
59	4	Charge monitoring	
60		<i>The ATLAS Diamond Beam Monitor</i>	61
61	4.1	Luminosity measurements	62
62	4.2	Diamond pixel module	63
63	4.2.1	Sensors	64
64	4.2.2	Front-end electronics	65
65	4.3	Module assembly and quality control	67
66	4.3.1	Assembly	67
67	4.3.2	Testing	68
68	4.3.3	Installation and commissioning	70
69	4.4	Performance results	71
70	4.4.1	Source tests	71
71	4.4.2	Test beam results	73
72	4.5	Operation	74
73	4.5.1	Positioning	74
74	4.5.2	Data taking during collisions	75
75	4.6	Conclusion	77
76	5	Current monitoring	
77		<i>Real-time particle identification</i>	79
78	5.1	Motivation	80
79	5.2	Requirements	80
80	5.3	Device specifications	81
81	5.4	Pulse parameters	81
82	5.5	Applications	83
83	5.6	Description of the firmware	84
84	5.6.1	Design constraints	84

CONTENTS

85	5.6.2 Analysis module	85
86	5.6.3 Area and width measurement	87
87	5.6.3.1 Vector cleaning	88
88	5.6.3.2 Algorithm	89
89	5.7 Control and data interface	91
90	5.7.1 Software	91
91	5.7.2 Data readout	91
92	5.8 Performance results	92
93	5.8.1 Comparison between the charge- and current-sensitive spec-	
94	troscopy	93
95	5.9 Source calibration	96
96	5.9.1 Source measurements – scatter plots	98
97	5.9.1.1 ^{241}Am source	98
98	5.9.1.2 ^{90}Sr and ^{60}Co source	103
99	5.10 Applications in neutron instrumentation	107
100	5.10.1 Thermal neutron flux monitoring	107
101	5.10.1.1 Measurements	108
102	5.10.1.2 Results and discussion	109
103	5.10.1.3 Conclusion	109
104	5.10.2 Fusion power monitoring	109
105	5.10.2.1 Measurements	110
106	5.10.2.2 Results and discussion	111
107	5.10.2.3 Conclusion	111
108	5.10.3 Fast and thermal neutron monitoring	113
109	5.10.3.1 Measurements	113
110	5.10.3.2 Results and discussion	115
111	5.10.3.3 Conclusion	115
112	5.11 Conclusion	116
113	Bibliography	117

¹¹⁴ List of Figures

¹¹⁵ 1.1	The Standard model [20].	2
¹¹⁶ 1.2	The TRIGA MARK II neutron reactor [14].	4
¹¹⁷ 1.3	The calorimeter in the n-ToF area [18].	5
¹¹⁸ 1.4	The Large Hadron Collider [19].	7
¹¹⁹ 1.5	The ATLAS Experiment [38].	8
¹²⁰ 1.6	The Insertable B-Layer – a silicon particle tracker installed in the ATLAS experiment in 2014 [34].	10
¹²¹ 1.7	A pCVD diamond pad detector [22].	11
¹²³ 2.1	In the equivalent electrical circuit diagram the electron-hole creation and drift can be modelled as a current source with a capacitor in parallel.	15
¹²⁴ 2.2	Stopping power for muons according to the Bethe-Bloch formula []	16
¹²⁵ 2.3	A point-like charge inducing current in a conductive plane.	17
¹²⁷ 2.4	Charge carrier drift in diamond for β/γ and for α particles crossing the sensor at $t = 0$	18
¹²⁸ 2.5	Calculated intrinsic energy resolution for silicon and diamond.	20
¹³⁰ 2.6	Left figure shows a profile of a diamond sensor only with an externally applied electric field. In the figure on the right a uniformly distributed space charge is added in the diamond, contributing to the internal electric field distribution. The induced current signal is proportional to the electrical field. d is the thickness of the diamond sensor.	22
¹³¹ 2.7	Impurities and non-uniformities in the crystal lattice due to radiation damage.	22
¹³⁷ 2.8	Simplified equivalent circuits of a current and charge amplifier.	23
¹³⁸ 2.9	Input and output signal of the current amplifier.	24
¹³⁹ 2.10	Input and output signal of the charge amplifier.	25
¹⁴⁰ 2.11	Input signal digitisation and quantisation error.	26
¹⁴¹ 2.12	An example of a Xilinx Virtex 5 FPGA [12] and an FE-I4 and FE-I3 ASIC chip [21].	28
¹⁴³ 3.1	Diagram of a diamond detector readout chain.	30
¹⁴⁴ 3.2	Amplifiers used for the charge and current measurements.	31
¹⁴⁵ 3.3	Two scCVD diamond samples: A IIa 1scdhq (left) and an E6 S37 (right).	32
¹⁴⁶ 3.4	Positioning of the α -source on top of the sensor carrier.	35

LIST OF FIGURES

147	3.5	Superimposed and averaged pulses (left figures, current amplifier) and distributions of deposited energy (right figures, charge amplifier) for three types of radiation. Note the scale on the X axis of the distributions.	37
148	3.6	Diamond radiation damage - a model based on displacements per atom [25]. The figure shows the DPA as a function of the kinetic energy for protons, neutrons and pions. Added are data points for protons and pions by RD42 [35] and one data point for pions measured in the scope of this study.	40
149	3.7	The figure shows the CCD for S37, S79 and S52 at a range of bias voltage settings.	41
150	3.8	The charge collection distance at 1 V/ μm bias voltage for the three diamond samples is plotted as a function of the received radiation dose. It is compared to the RD42 data for pion irradiation. The data points are about 15–25 % lower than expected from the RD42 data [35].	42
151	3.9	Relative increase of charge collection over time due to priming with the ^{90}Sr radioactive source. The charge collection for the non-irradiated S37 stays constant. The bias voltage for this measurement is 1 V/ μm .	44
152	3.10	Relative decrease of the collected charge as a function of the received α dose for non-irradiated and irradiated diamond samples.	45
153	3.11	The signal of the irradiated and primed S79 deteriorates with time for both polarities. Every plot contains 60 superimposed pulses.	47
154	3.12	Deterioration of the pulse shapes with time.	48
155	3.13	Comparison of the five procedures for the “healing” process for an irradiated diamond that had been exposed to α radiation with a rate of 10^1 s^{-1} , with the bias voltage switched on, for at least 30 minutes.	49
156	3.14	Varied bias voltage at a fixed temperature.	51
157	3.15	Several data points between 4 K and 295 K at a bias voltage of $\pm 500 \text{ V}$.	52
158	3.16	Varied bias voltage at a fixed temperature for an irradiated sample. .	54
159	3.17	After irradiation: several data points between 4 K and 295 K at a bias voltage of $\pm 500 \text{ V}$	55
160	3.18	Collected charge for electrons as a function of temperature.	56
161	3.19	Collected charge for holes as a function of temperature.	56
162	3.20	This figure shows the charge carrier lifetime as a function of temperature. The data points between 75 K and 150 K are omitted. The fit function only works well on signals with a well pronounced decaying top.	57
163	3.21	This figure shows the carrier lifetime averaged over all temperatures and plotted as a function of the π irradiation dose.	58
184	4.1	Diamond detectors installed in high-energy physics experiments in the last decade, sorted by the active sensor area. The first four detectors from the left are radiation monitors whereas the right two are pixel trackers.	62
185			
186			
187			

LIST OF FIGURES

188	4.2	DBM module, top-down view. Visible is the flexible PCB with signal and power connections, the silicon sensor and a part of the FE-I4. Wire bonds from the PCB to the FE-I4 and to the sensor are also visible.	63
189	4.3	A pCVD wafer. The golden dots on the surface are the electrodes that are applied during the qualification test. The wafer is measured across the surface to find the regions with the highest efficiency.	64
190	4.4	FE-I4 layout, top-down view. The pink area are pixels grouped into columns, the green area below is the common logic and the red strip at the bottom are the wire bond pads.	65
191	4.5	Schematic of an analog pixel. Courtesy of the FE-I4 collaboration.	66
192	4.6	An assembled DBM module.	68
193	4.7	Module production with time.	69
194	4.8	Occupancy and pseudo-efficiency scans for the silicon (left) and dia- mond sensor (right) to check for disconnected regions and estimate the sensor's efficiency. Shadows of the electronic components are clearly visible because fewer electrons were able to traverse through such a higher amount of material.	72
195	4.9	Measurements of pseudo-efficiency and disconnected regions for all modules that went through the QC procedure.	73
196	4.10	An efficiency study of a prototype DBM diamond module in a test beam. The statistics are low (~ 10 hits/pixel) as the data was collected during a short run.	74
197	4.11	This photo highlights four telescopes installed onto the nSQPs and around the pipe.	75
198	4.12	Position of the DBM in the ATLAS experiment.	75
199	4.13	Occupancy of individual modules during collisions. Only 16 modules were taking data.	76
200	4.14	A diagram showing the radial distance R_0 and longitudinal distance Z_0 of the trajectory from the interaction point at the minimal distance d . Z is the axis along the beam line. Three module planes intercept a particle and reconstruct its trajectory.	77
201	4.15	These two plots show two parameters of particle tracks recorded by one of the DBM telescopes: radial and longitudinal distance of the projected tracks from the interaction point.	78
222	5.1	A pulse and its parameters.	82

LIST OF FIGURES

223 5.2	Form Factor is the ratio between the measured area (a) and the calculated area ($A \times BW$) of the pulse. The calculated area is significantly larger than the measured area for a triangular triangular pulse, but less so for the rectangular one. The red and blue dot in the right plot are the value entries of the two pulses shown. The red and blue oval shapes depict the regions for the values expected from triangular and rectangular pulses. By carefully choosing the linear qualifier (dashed line) and taking only the entries below the cut rectangular pulses can be identified.	82
232 5.3	Firmware design structure.	84
233 5.4	Code design plan.	85
234 5.5	A sample pulse. The first vector shows which samples are above the width measurement height. The second vector is a clean vector. The third line shows the position of the maximum amplitude. The vector cleaning algorithm starts from the maximum amplitude and continues in both ways along the vector.	88
239 5.6	This block counts the remaining binary ones in the clean vectors and outputs this value as the pulse width.	88
240 5.7	This block masks the input data with the clean vector and sums the remaining samples.	89
244 5.8	Vector cleaning routine outputs two vectors - one forward in time and one back in time from the peak of the pulse.	89
245 5.9	One logic step in the algorithm chain before and after Karnaugh minimisation.	90
247 5.10	Vector is divided into two 16-bit logic chains. The algorithm logic is then run on the two chains separately. The results are then merged into one 32-bit clean vector by using a set of AND gates.	90
250 5.11	Abstraction levels of the controller software.	91
251 5.12	This figure shows the capability of the device to analyse all arriving pulses for a range of input frequencies. The highest achievable rate with zero lost pulses is $5 \times 10^6 \text{ s}^{-1}$	93
254 5.13	These diagrams show the linearity of the measurements and their stability with respect to analog noise.	94
256 5.14	Spectrum of a $^{148}\text{Gd}^{239}\text{Pu}^{241}\text{Am}^{244}\text{Cm}$ source using a Cx and a C2 amplifier.	95
258 5.15	Accumulated pulses for all runs.	97
259 5.16	^{241}Am , e^- collection. Qualifier: FWHM. Optional qualifiers: Amplitude, Form Factor.	100
261 5.17	^{241}Am , h^+ collection. Qualifier: FWHM.	101
262 5.18	^{241}Am area histograms for electron and hole collection.	102
263 5.19	^{90}Sr scatter plots.	104
264 5.20	^{60}Co scatter plots.	105
265 5.21	Energy distributions for γ and β particles.	106

LIST OF FIGURES

266	5.22 Thermal neutrons, photons. Qualifier: FWHM.	109
267	5.23 Energy spectrum after applied qualifiers reveals the tritium and α peak	110
268	5.24 ^{239}Pu Be. Qualifiers: BW-FWHM, FWHM, Form Factor	112
269	5.25 ^{239}Pu Be, energy distribution of the neutrons interacting in the ballistic centre.	113
270	5.26 Fast neutrons, thermal neutrons, photons. Qualifiers: BW-FWHM, FWHM, Form factor, Slope.	114
271	5.27 Energy spectrum in CROCUS before and after applied qualifiers . . .	115
272		
273		

²⁷⁴ Chapter 1

²⁷⁵ Introduction

²⁷⁶ Curiosity is the driving force behind the development of human civilisation. Over centuries, scientists have discovered new methods for understanding Nature and the fundamental mechanisms governing the Universe, using continually improving research methods and technology to peer ever deeper into the heart of matter.

²⁸⁰ After the initial discovery of atoms, their underlying structure was soon revealed to be that of a positively charged core surrounded by a cloud of orbiting electrons. ²⁸¹ The atomic nucleus was subsequently decomposed into protons and neutrons, which ²⁸² themselves were found to consist of three tiny quarks. Studying these minuscule ²⁸³ building blocks of visible matter has made it possible to understand more about the ²⁸⁴ intricate complexities of the Universe, and the mechanisms that guide its behaviour ²⁸⁵ and evolution.

²⁸⁷ Discoveries of this magnitude would not have been possible without the technologies developed to carry out such experiments. On one hand, the energy of the ²⁸⁸ experimental devices has been increasing continually, allowing smaller and smaller ²⁸⁹ distance scales to be probed. On the other hand, the devices used to observe and ²⁹⁰ measure the phenomena created in these experiments have had to be designed with ²⁹¹ improved precision, speed and durability.

²⁹³ Keeping these factors in mind, the goal of this work was to find “the perfect material”. Diamond proved to be a worthy contender, offering both outstanding ²⁹⁴ electrical and mechanical properties which make it the material of choice for a number ²⁹⁵ of applications in experimental physics. However, much remains to be learned about ²⁹⁶ its behaviour, and this thesis adds a small piece to the shimmering mosaic of diamond ²⁹⁷ research efforts.

²⁹⁹ The first chapter introduces some of the leading particle physics research institutes, and describes how their research is carried out. The second chapter discusses ³⁰⁰ the properties of diamond detectors used in high energy particle physics experiments. ³⁰¹ A diamond sensor irradiation study is presented in chapter 3. The conclusions of this ³⁰² study, which define the constraints for the two diamond detector applications, are ³⁰³ presented in the final two chapters.

1.1. FUNDAMENTAL RESEARCH

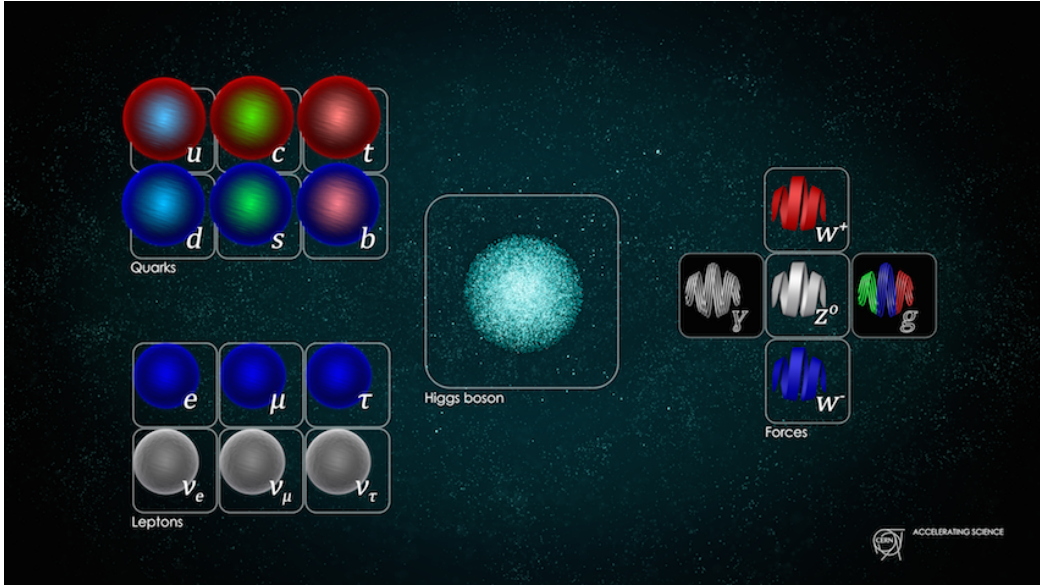


Figure 1.1: The Standard model [20].

305 1.1 Fundamental research

306 The aim of fundamental research is to define scientific theories and verify them to
307 improve our understanding of the universe. It does not in itself focus on applying
308 this research by developing products and is not meant to create a direct return on
309 investment. Instead, it expands the overall knowledge of the human kind - by making
310 the results freely available to the general public.

311 Particle physics research peers into the smallest constituents of the universe, dis-
312 secting the atoms into quarks and electrons, catching cosmic rays and figuring out
313 what dark matter is made of. Particle physicists want to explain the phenomena
314 surrounding us by studying the fundamental particles and the mechanisms govern-
315 ing their interactions. By understanding this, we would be able to answer difficult
316 questions; How did the universe begin? What is the invisible force (dark matter,
317 dark energy) pushing the galaxies apart from each other? Where does mass come
318 from? Why is there almost no antimatter in the universe? In this effort, scientists
319 have formed several theories. One of them, the Standard Model of particles, is cur-
320 rently the most successful theory to describe the constituents of matter and their
321 interactions.

322 **The Standard Model** (SM) is a physics theory developed in the 1970's [37]. It
323 was designed to explain the current experimental results. As such, it was also able to
324 predict new discoveries and was a driving force for the scientists to invest time and
325 money in developing new experiments. To date, it is by far the most established and
326 verified physics theory. It explains how the basic building blocks of matter – *fermions*
327 – interact with each other via mediators of interactions called *bosons*. There are two
328 main families of fermions - *quarks* and *leptons*, as shown in figure 1.1. Each group

329 consists of six members divided into three *generations*, the first being the lightest and
330 most stable and the last the heaviest, which are the most unstable. The nature around
331 us is made up of the stable particles – those from the second or third generations can
332 only be found in cosmic rays or produced artificially using particle accelerators.

333 Quarks have a spin of 1/2 and a charge of either +2/3 (up, charm, top) or -1/3
334 (down, strange, bottom) while the leptons have a spin of 1/2 and a charge of either 1
335 (electron, muon, tau) or 0 (electron neutrino, muon neutrino, tau neutrino). Leptons
336 only exist individually – they do not cluster. Quarks, however, immediately form a
337 cluster of either two (unstable), three (more stable) or five (unstable). Two up and
338 one down quark make up a proton whereas two down and one up quark make up a
339 neutron.

340 In addition to fermions, each particle has its corresponding antiparticle – a particle
341 with the same mass but the opposite charge. If an antiparticle hits a particle, they
342 annihilate each other, producing energy in form of photons.

343 Bosons are the carriers of force that mediate weak (W^+ , W^- and Z bosons), strong
344 (gluons) and electromagnetic (photons) interactions. The weak interaction is respon-
345 sible for the radioactive decay of subatomic particles, thus playing an essential role in
346 nuclear fusion – a process taking place in the stars. The electromagnetic interaction
347 works at a macroscopic level – it allows particles to interact via electric and magnetic
348 fields. The strong interaction is effective at femtometer distances and it governs how
349 quarks interact and bind with each other. An additional boson is the Higgs boson
350 discovered at CERN in 2012 []. It is a representation of the Higgs mechanism, which
351 gives rise to the mass (or lack thereof) of all the particles in the Standard Model.

352 1.2 Research institutes

353 This section gives a short overview of some of the institutes and collaborations car-
354 rying out fundamental physics research. These facilities were used for the research
355 carried out for this thesis.

356 **CERN** (European Centre for Nuclear Research) [5] is the largest particle physics
357 laboratory in the world, straddling the Swiss-French border just outside Geneva. It
358 was established in 1954 to bring the war-torn Europe together by means of funda-
359 mental scientific research. Today, its 22 member state countries and several observer
360 states contribute approximately 1 billion CHF annually to fund the research and de-
361 velopment. More than 10000 scientists, engineers, technicians, students and others
362 from all around the globe work at CERN on many projects in research fields ranging
363 from particle to nuclear physics. The scope is to probe the fundamental structure of
364 the universe and to understand the mechanisms governing it. Therefore CERN’s main
365 function is to provide the infrastructure for high-energy physics experiments. These
366 are carried out using large machines called particle accelerators. These instruments
367 boost beams of particles to high energies before making them collide with each other

1.2. RESEARCH INSTITUTES

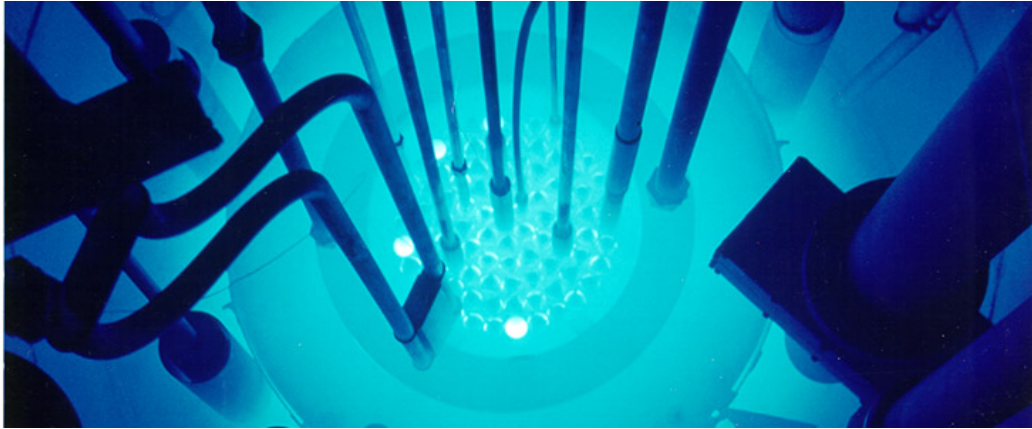


Figure 1.2: The TRIGA MARK II neutron reactor [14].

368 or with stationary targets. The resulting collisions are recorded by particle detectors
369 and later analysed by physicists. To carry out research on the smallest constituents
370 of matter, their dynamics and structure, very high energies are needed. This is why
371 the most powerful accelerators are used for fundamental research. The largest accel-
372 erators at CERN are the Proton Synchrotron [], the Super Proton Synchrotron [36]
373 and the Large Hadron Collider, described in 1.3.

374 **Atominstitut, Vienna** (ATI) [1], an institute for atomic and subatomic physics,
375 was established in 1958 in Vienna as an inter-university institute. It houses around
376 200 people involved in a broad range of research fields: quantum, particle, neutron,
377 nuclear, radiation and reactor physics, quantum optics etc. As of 2002 the ATI is
378 part of the University of Technology in Vienna.

379 Its central facility is *TRIGA MARK II* [11], a neutron reactor used for training,
380 research and isotope production. It is one of 40 such reactors worldwide, produced by
381 the Californian company General Atomic in the early 60's. It is capable of continuous
382 operation at a maximum output power of 250 kW. The reactor core consists of 3 kg
383 of 20 % enriched uranium (^{235}U). The fuel moderator rods are mostly made up of
384 zirconium with low percentage of hydrogen and uranium. Both the core and the rods
385 are immersed in a pool of water as shown in figure 1.2 for the purpose of cooling
386 and radiation protection. The surrounding concrete walls are 2 m wide with an
387 added graphite layer for improved shielding. Four main experimental apertures for
388 neutron beam are placed radially through the walls. All exits are heavily shielded to
389 prevent the people from being exposed to radiation, but still leaving enough space
390 to set up experiments. Apart from the beam apertures, there are several other exits
391 and components, e.g. a thermal column for generation of thermal (low energetic)
392 neutrons.

393 **n-ToF** (neutron Time-of-Flight) [8] is a scientific collaboration with the aim of study-
394 ing neutron-nucleus interactions. Over 30 institutes are active members of this col-
395 laboration, among them Atominstitut in Vienna. The n-ToF experiment is located at

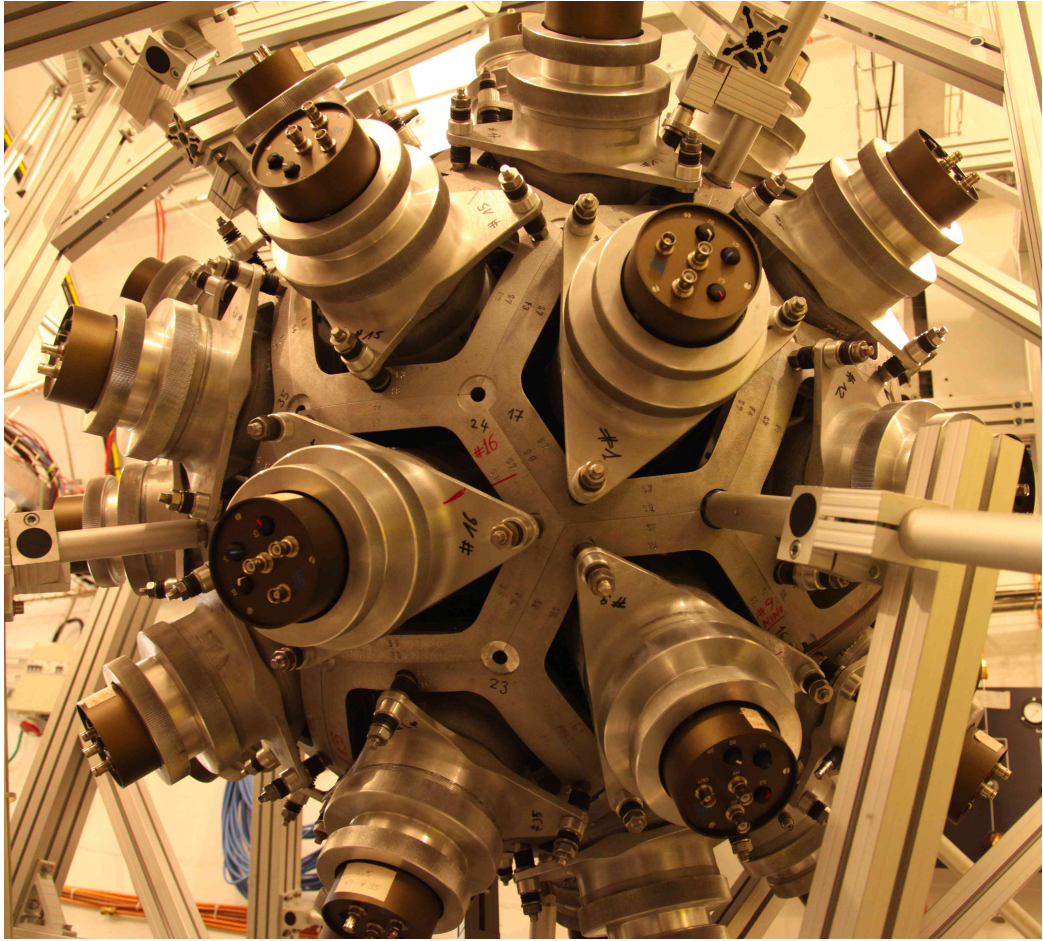


Figure 1.3: The calorimeter in the n-ToF area [18].

396 CERN where the experiments are carried out in a 200 m long experimental area. The
 397 knowledge stemming from the experimental results can then be applied in various
 398 fields ranging from nuclear technology and cancer therapy to astrophysics.

399 A pulsed beam of highly energetic protons (20 GeV/c) is produced by the Proton
 400 Synchrotron (PS) and aimed at a fixed lead spallation target. Each proton hitting
 401 the target produces around 300 neutrons of various energies. Initially highly energetic
 402 neutrons are slowed down by the target and by a slab of water placed behind it. This
 403 broadens their energy spectrum, which then ranges from meV (thermal neutrons) to
 404 GeV (fast neutrons). The neutrons are then sent through a 185 m long evacuated pipe
 405 to the experimental area, where they collide with another target or a sample. The
 406 radiation created by the collisions is detected by a set of dedicated detectors around
 407 the interaction point, as shown in figure 1.3. Having different energies, neutrons
 408 travel with different speeds, highly energetic ones reaching the target faster than
 409 those with low energies. The analysis of collisions with a precise timing allows for a
 410 determination of the interaction probability with the sample material as a function
 411 of energy of the incident neutrons.

412 1.3 The Large Hadron Collider

413 A particle accelerator is a machine that accelerates beams of charged particles such
414 as protons, electrons, ions etc. It generates electric fields that add kinetic energy
415 to the particles, speeding them up. It then uses magnets to retain them within a
416 defined trajectory and inside the evacuated beam pipe. The trajectory can be either
417 linear (linear accelerators or LINACs) or circular (circular or cyclic accelerators). The
418 former accelerate particles in a straight line, therefore the acceleration process only
419 occurs once. The latter can accelerate particles many times while keeping them in
420 orbit, but need a LINAC to pre-accelerate the particles before being injected in the
421 loop.

422 Particle accelerators are used in numerous fields ranging from fundamental and
423 material research, cancer treatment to industrial applications, such as biomedicine
424 and material processing. Several types of accelerators exist: electrostatic accelerators,
425 LINACs, cyclotrons, synrocyclotrons, synchrotrons, synchrotron radiation sources
426 and fixed-field alternating gradient accelerators (FFAGs).

427 The Large Hadron Collider (LHC, figure 1.4) at CERN is the largest particle
428 collider in the world. It was build between 1998 and 2008 and was first successfully
429 started in 2010 and operated until 2013 when it underwent a two-year long upgrade.
430 Its second operational cycle started at the beginning of 2015.

431 The LHC is a 27 km long circular machine set up in a tunnel deep under the
432 surface, ranging from 50 to 175 m below ground. It accelerates two proton beams to
433 the energy of 6.5 TeV per beam before it makes them collide with each other with
434 the energy of 13 TeV at four different interaction points around its circumference.
435 Hair-thin particle beams are guided inside two evacuated pipes with a \sim 5 cm radius
436 by means of magnetic field. Coils made up of a superconductive material are wound
437 around the pipes in special patterns. When cooled down to -271 °C using liquid he-
438 lium, they become superconductive; the resistivity of the material drops significantly,
439 minimising the heat dissipation despite high electric currents. These produce strong
440 magnetic fields which bend the particles and keep them in a circular trajectory.

441 The protons travel bunched together in groups of 10^{11} per bunch. These bunches
442 are accelerated when traversing the radio-frequency (RF) cavities with the frequency
443 of the electromagnetic field equal to 400 MHz. This oscillating field creates 2.5 ns
444 long buckets – compartments for the bunches. Only one out of ten buckets is filled, so
445 the bunches are spaced at 25 ns. This defines the machine's clock (40 MHz) as well as
446 the maximum rate of collisions - the bunches travelling in the opposite direction cross
447 at the intersections 40 million times per second. Around 20 collisions occur during
448 every bunch crossing, yielding the maximum collision rate of the order of 10^9 s^{-1} . The
449 number of collisions will increase in the following years; the number of particles per
450 bunch will be increased and the transverse spread of the bunches will be decreased.
451 The bunch density will therefore be increased, which will in turn increase the collision
452 probability – the cross-section. The original design number of collisions accumulated
453 over the years of operation is presented in the form of integrated luminosity [] and is

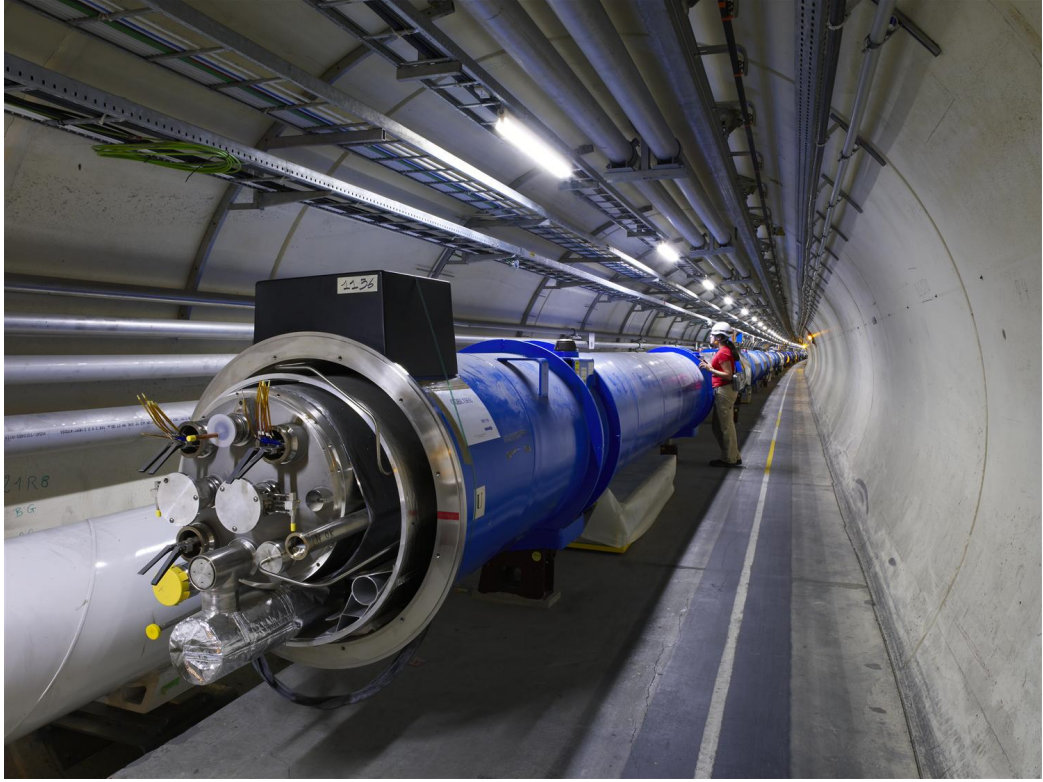


Figure 1.4: The Large Hadron Collider [19].

454 of the order of 300 fb^{-1} (inverse femtobarn). After the planned upgrades in 2020, the
455 High-Luminosity LHC [] will achieve up to 3000 fb^{-1} .

456 1.4 The ATLAS experiment

457 ATLAS (short for A Toroidal Lhc ApparatuS, figure 1.5) [] is a particle physics
458 experiment at CERN. Its purpose is to verify current theories and to search for new
459 discoveries by observing and analysing high energy proton-proton collisions produced
460 by the LHC. It is the biggest experiment at CERN by dimensions (45 m in length
461 and 26 m in height) and the number of people involved (more than 3000 physicists
462 and engineers). The ATLAS experiment consists of a number of detectors, each
463 designed to measure a specific property of the particles and photons produced during
464 the collision. The closest to the collision point is the Inner Detector (ID), which
465 consists of scintillating elements, a Transition Radiation Tracker and of the several
466 layers of highly spatially segmented semiconductor sensors, which record single points
467 of the incident particles. These points are later reconstructed into particle tracks. In
468 addition, a strong magnetic field of 2 T curves the paths of the charged particles, which
469 in turn allows the ID to identify an individual particle's charge and momentum. The
470 next two parts are the electromagnetic and tile calorimeter. These detectors weigh
471 a few thousand tonnes and measure the energy that the particles deposit in the

1.4. THE ATLAS EXPERIMENT

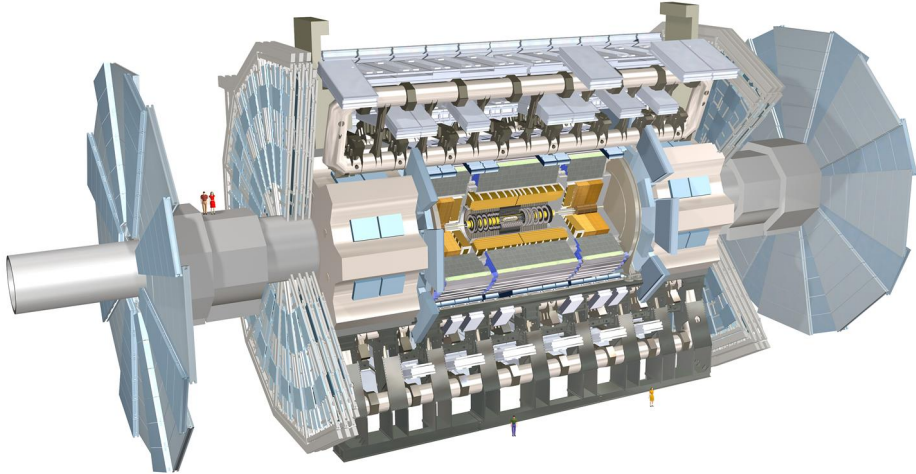


Figure 1.5: The ATLAS Experiment [38].

material. The only particles that make it through the calorimeters are neutrinos and muons. The former cannot be detected with the detectors in ATLAS. The latter however are detected by the Muon Spectrometer, a set of large detector plates placed all around the calorimeters. The last is the superconductive magnet which provides the magnetic field to allow the Muon Spectrometer to measure muon momenta. The ID has its own set of magnets that are used for the same purpose. To sum up, the Inner Detector measures the charge and momenta of the particles, the calorimeters measure their energies, the Muon Spectrometer measures muon tracks and momenta and the magnets provide magnetic fields, which curve the trajectories of the charged particles, allowing for identification of particle momenta.

The ATLAS detector has been designed to measure every collision taking place in its core. With 25 ns between collisions, this makes up 40 million collisions per second. The maximum realistic achievable rate of recording is approximately 100 kHz [38]. A recorded collision is referred to as an event. Every event holds information acquired by all the detectors within ATLAS. This amounts to approximately $\sim 10^6$ channels of data, yielding an event size of approximately 10 MB. Therefore the data rate at the maximum achievable rate is 3 TB/s. To reduce the amount of data stored a special classification system with a complex trigger logic, which is in place to decide which events should be stored and analysed further. It reaches a decision in the order of tens of microseconds after an event. If this is the case, the data acquisition system triggers the readout of the entire detector. This way the recorded event rate is reduced from 100 kHz to ~ 500 Hz.

A complex Trigger and Data Acquisition system (TDAQ) is in place to distribute

495 the clock signal, configure the detectors, perform data acquisition and handle the
496 output data. The data are then stored at the CERN computer centre and distributed
497 across the globe by means of the GRID – a distributed data analysis and data storage
498 system.

499 1.5 Particle detectors

500 Particle detectors, or radiation detectors, have first come into use at the end of the
501 19th century. At that time Wilhelm Röntgen used a photographic plate onto which
502 he shone X-rays. Soon after, in 1912, Victor F. Hess discovered cosmic rays during
503 a balloon flight. This paved the way for development of particle detectors. A cloud
504 chamber was designed – a chamber filled with a supersaturated vapour of water or
505 alcohol. If a highly energetic particle traversed the chamber, the mixture ionised,
506 creating condensation nuclei. These traces were visible and were photographed. The
507 particle detectors developed later relied on different types of interaction between the
508 incident particles and the detector material, e.g. transition radiation, Cherenkov ra-
509 diation and ionisation. The bubble chamber invented in 1952 used a superheated
510 transparent liquid – a liquid heated just below its boiling point. A particle ionised
511 the liquid, forming microscopic bubbles along its trajectory. Then followed the spark
512 chamber and the wire chamber where the particle ionised the gas, causing a spark
513 between two parallel plates at a high potential difference. These are nowadays used
514 in a handful of experiments and may often be seen in museums as showcases. Next
515 were ionisation chambers, which measured the induced current of the free ionised
516 charges moving in an externally applied electric field. Finally in the 1960s, semicon-
517 ductor detectors were introduced. Their principle of operation is similar to that of an
518 ionisation chamber, with the difference that a semi-conductive material is used as an
519 ionisation medium instead of gas. Nowadays an ensemble of several types of detectors
520 is used as a specialised detector system. Many considerations need to be taken into
521 account when designing such a system: detector geometry, segmentation, event rate,
522 efficiency, readout, support structures, cabling, cooling, cost etc.

523 Particle detectors can be divided in two groups: tracking detectors and calorime-
524 ters. The former are designed to measure particle momentum, charge, origin and
525 direction of flight, with a minimal impact on their flight path or energy with the aim
526 to optimise the spatial resolution. The calorimeters, on the other hand, measure the
527 energy of the particles by stopping them. This means they need to be heavy and
528 dense. A typical physics experiment nowadays consists of a tracking detector en-
529 closed by a calorimeter. This way the energy, charge and momentum can be derived
530 for every particle created in the collision.

531 1.5.1 Semiconductor detectors

532 Semiconductor is a class of solids whose electrical conductivity is between that of a
533 conductor and that of an insulator. Semiconductor particle detectors are devices that

1.5. PARTICLE DETECTORS



Figure 1.6: The Insertable B-Layer – a silicon particle tracker installed in the ATLAS experiment in 2014 [34].

use a semiconductor to detect radiation. They work on the principle of an ionisation chamber. An incident particle ionises the atoms in the crystal lattice. The charges are freed if the deposited energy is higher than the energy band gap (i.e. the energy needed to excite an electron from its steady state to the conductance band). The freed charge carriers start drifting in an externally applied electric field, inducing current on the electrodes.

A number of semiconductor materials exist, each with a different band gap. Germanium (Ge) for instance has a band gap of 0.67 eV, which means that most of the electrons at the room temperature are already in an excited state due to thermal excitation. The thermally excited electrons moving through the material are referred to as leakage current. This current is also present in silicon with an energy gap of 1.12 eV. To reduce this effect the semiconductor sensors are doped with donors and acceptors, forming a diode. The diode is then inversely biased to deplete the material of all moving charges. Doped silicon fulfils most of the needs for particle physics requirements and is therefore the most widely used material for particle detection.

Semiconductor detectors are most widely used for tracking applications, like the Insertable B-Layer shown in figure 1.6 [39], which was installed in ATLAS Experiment in 2014. First, they can be produced in thin layers to minimise the impact on the path of the incident particles. Second, their low sensor capacitance allows for a fast signal response. Third, they are highly efficient and highly resistant to radiation damage. Finally, the industrial processes allow for a fine spatial segmentation, which in turn improves the track resolution of a detector system.

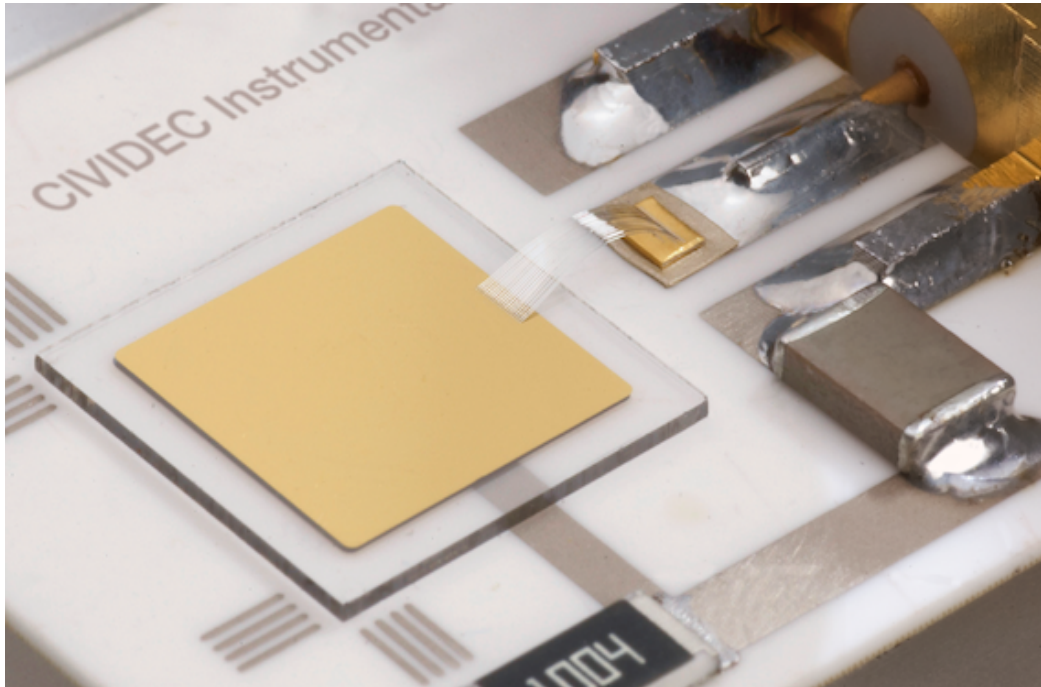


Figure 1.7: A pCVD diamond pad detector [22].

556 Semiconductor sensors come in several configurations. The simplest type is a pad
557 – a single plate with two electrodes. Pads are used for particle counting and radiation
558 monitoring. Next is a strip detector, a more finely segmented detector made out of
559 long parallel sensing areas or strips. Normally each strip has its own signal line for
560 readout. Usually the strip detectors are used in pairs – one detector is placed on top
561 of the other at an angle to increase spatial resolution in both axes. The third and
562 the most finely segmented is a pixel detector, consisting of a 2D array of independent
563 sensing areas. In tracking applications, pixel detectors are used where the need for a
564 high detection resolution and granularity requirement is the highest. Due to their high
565 production cost and a high number of signal channels, they can only cover limited
566 areas. Strip detectors can be used to cover larger areas in several consecutive layers.

567 1.5.2 Diamond sensors

568 Diamond has been known for over two millennia, valued for its mechanical properties
569 and its appearance. When the procedures for its synthesis were discovered, diamond
570 made its way to a broad range of industries which exploit its optical and electri-
571 cal properties. The discovery of the Chemical Vapour Deposition (CVD, described
572 below) as a new synthesis process gave rise to a range of new applications. Purer
573 specimens are used in electronics, high-power switching devices, electrochemical sys-
574 tems, radiation sensors, quantum computing etc. Recently it was found that it also
575 exhibits superconductivity [1]. This thesis focuses on the use of diamond for radiation
576 detection.

1.5. PARTICLE DETECTORS

577 Compared to a natural diamond, a CVD diamond used as a particle detector has
578 almost no impurities (foreign atoms like nitrogen or boron). If proper procedures are
579 followed, the diamond lattice can be grown very uniformly. This in turn improves
580 electrical properties of the grown sample. Diamond is an almost perfect thermal
581 and electrical insulator. However, its electrical behaviour is similar to that of a
582 semiconductor. Its high 5.5 eV energy band gap prevents the electrons to be thermally
583 excited to the conduction band. This eliminates the need to dope the diamond to
584 suppress the leakage current. In addition, the gap is too wide for the visible light
585 to excite the electrons. All diamond properties are described in detail in chapter 2.
586 Figure 1.7 shows a diamond pad sensor embedded in a particle detector produced by
587 CIVIDEC Instrumentation GmbH.

588 **Chemical vapour deposition** (CVD) [] is a process where a material is deposited
589 from a gas onto a substrate, involving chemical reactions. It is often carried out
590 under high pressure and high temperatures. It takes place in enclosed chambers
591 called furnaces with careful regulation of the temperature, pressure and gas mixture.
592 Synthetic diamond is grown at 700–900 °C with a mixture of hydrogen and methane
593 gas. At this temperature the molecules dissociate into carbon and hydrogen atoms.
594 The carbon atoms are the building blocks and are deposited on the surface of the
595 substrate.

596 Under a carefully controlled pressure and temperature conditions with an added abra-
597 sive atomic hydrogen the graphitic bonds break and form into diamond bonds. The
598 speed of the growth can be anywhere between 0.1 and 10 µm per hour. The detector
599 grade samples are grown at a rate of the order of 1 µm per hour. They can grow up to
600 several millimetres in thickness. The width of the samples, however, depends entirely
601 on the substrate used. Diamond can be deposited on various materials: diamond,
602 silicon, tungsten, quartz glass etc. The substrate material must be able to withstand
603 the high temperatures during the CVD process. The diamond substrate does not
604 need any surface pre-treatment. Carbon atoms form bonds with atoms in the exist-
605 ing crystal structure. This is the homo-epitaxial growth where the newly deposited
606 atoms retain the orientation of the structure in the substrate. Other non-diamond
607 substrates, however, need to be pre-treated, usually by being polished using diamond
608 powder. Some powder particles remain on the surface, acting as seeds for the growth
609 of small crystals or grains. These grains grow and at some point merge with the
610 adjacent ones, making up a compact material. The lower side is later polished away.
611 These diamonds are called *polycrystalline* (pCVD) whereas those grown on a diamond
612 substrate are *single crystal* (sCVD) diamonds. The area of the former can be large -
613 up to 0.5 m² or more compact 15 cm² in the case of detector grade diamonds. The
614 sCVD diamonds, on the other hand, can currently only measure up to 1.5 cm².

615

Chapter 2

616

Signal formation in diamond

617 This chapter describes the fundamentals of signal formation in a diamond sensor,
618 as well as its use as a particle detector. This is described in section 2.1 where the
619 principles of energy deposition are explained. Then the current signal shapes of
620 different types of radiation are shown. Later on the internal lattice defects that affect
621 the signal are described. The final section contains the description of the remaining
622 part of the signal chain – signal amplifiers, digitisers and devices for signal processing.
623 Noise contributions are discussed at every stage of the signal chain.

624 Ionisation is the main signal generation mechanism in diamond, silicon and other
625 semiconducting materials. A semiconductor sensor converts the energy deposited
626 by an incident energetic particle to an electrical signal. In particular, the particle
627 ionises the atoms in the lattice, freeing electrons and holes, which then drift towards
628 positively and negatively charged electrodes due to an externally applied electrical
629 field, inducing an electrical signal on the electrodes.

630 Silicon is currently considered as the industry standard for particle detection.
631 However, there are several disadvantages of using silicon instead of diamond, due
632 to significant differences in the material properties. In particular, the properties of
633 silicon change significantly with radiation. Due to radiation-induced lattice defects,
634 which act as charge traps, the charge collection efficiency is decreased. The defects
635 are also responsible for the increase of the leakage current, increasing the shot noise
636 eventually leading to a thermal runaway. The same is true for diamond, but on a
637 smaller scale.

638 Table 5.2 compares the properties of diamond and silicon. Some of these values
639 are revisited and used in the course of this thesis.

2.1. PRINCIPLES OF SIGNAL FORMATION IN SEMICONDUCTORS

Property	Diamond	Silicon
Band gap energy E_g (eV)	5.5	1.12
Electron mobility μ_e ($\text{cm}^2 \text{ V}^{-1} \text{ s}^{-1}$)	1800	1350
Hole mobility μ_h ($\text{cm}^2 \text{ V}^{-1} \text{ s}^{-1}$)	1200	450
Breakdown field (V cm^{-1})	10^7	3×10^5
Resistivity ($\Omega \text{ cm}$)	$> 10^{11}$	2.3×10^5
Intrinsic carrier density (cm^{-3})	$< 10^3$	1.5×10^{10}
Mass density (g cm^{-3})	3.52	2.33
Atomic charge	6	14
Dielectric constant ϵ	5.7	11.9
Displacement energy (eV/atom)	43	13 – 20
Energy to create an e-h pair (eV)	13	3.6
Radiation length (cm)	12.2	9.6
Avg. signal created/ μm (e)	36	89

Table 2.1: Comparison diamond – silicon [?, 28].

2.1 Principles of signal formation in semiconductors

Particles can interact with the sensor in several ways, e.g. via bremsstrahlung [], elastic or inelastic scattering (e-h pair production) or nuclear reactions. Bremsstrahlung is radiation created when a particle is decelerated due to interaction with the electric field of the core of an atom. Elastic scattering is deflection of the particle's trajectory due to the pull from the nucleus without depositing any energy in it. This is in principle an unwanted effect in semiconductors as it deteriorates the spatial resolution of the sensor. Inelastic scattering is the interaction through which an atom is ionised and an electron-hole pair is created. All these effects are competing and are dependent on the particle's mass, momentum etc.

Semiconductors are materials with a conductance between that of insulators and that of metals – of the order of $10^{25} \Omega^{-1} \text{ cm}^{-2}$. They can be made up of atoms with four electrons in their valence band (e.g. silicon–Si, carbon–C or germanium–Ge) or as combinations of two or more different materials (e.g. gallium arsenide–GaAs). The atoms in the lattice form valence bonds with adjacent atoms, making solid crystal structures.

The valence bonds between atoms in the crystal lattice can break apart if sufficient external energy is deposited. The electron that was forming the bond is excited into the conductance band, leaving behind a positively charged ion with a vacancy – a hole – in its valence band, as shown in figure 2.1a. A free electron-hole pair is thus created. The free electron travels through the crystal until it is recombined with another hole. Similarly, the hole also travels through the material. Its positive charge attracts a bound electron in the vicinity, which breaks from the current bond and moves to the vacancy, leaving a new hole behind. The process continues, making it look like the hole is traveling through the material [].

The electrons need to absorb a certain energy to get to get ionised. The minimal

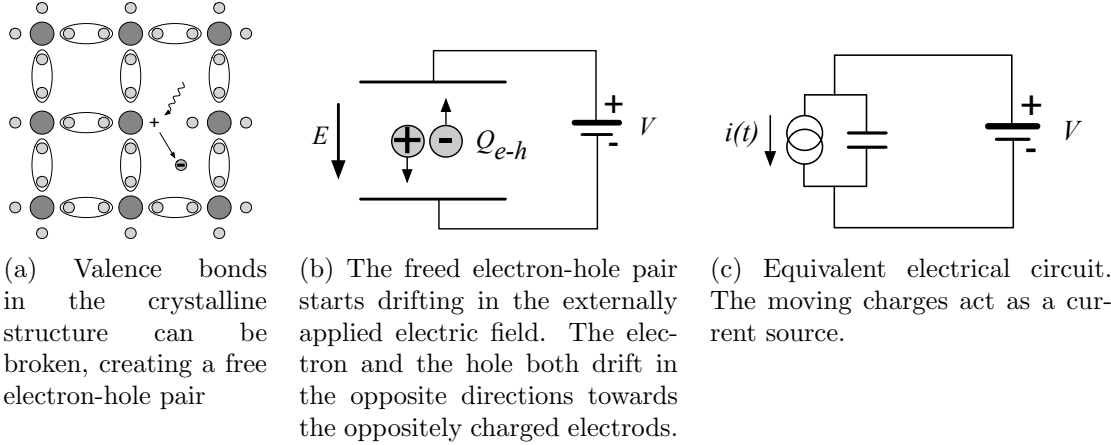


Figure 2.1: In the equivalent electrical circuit diagram the electron-hole creation and drift can be modelled as a current source with a capacitor in parallel.

transferred energy required to excite an electron in a semiconductor is equal to the energy gap E_g . Typical widths of the forbidden gap are 0.7 eV in Ge, 1.12 eV in Si, 1.4 eV in GaAs and 5.5 eV in diamond. Due to the small band gap in semiconductors a significant amount of electrons already occupies the conduction band at room temperature (RT) due to thermal excitation, according to the probabilistic distribution.

The intrinsic carrier concentration n_i in semiconductors is given as

$$n_i = T^{3/2} \cdot \exp\left(-\frac{E_g}{2k_B T}\right) \quad (2.1)$$

wherein $k_B = 1.381 \times 10^{-23} \text{ m}^2 \text{ kg s}^{-2} \text{ K}^{-1}$ is the Boltzmann constant, E_g is the energy band gap of the semiconductor and T is the temperature in K.

If an external electric field is applied to the crystalline structure, the free electrons and holes drift toward the positive and negative potential, respectively, as shown in figure 2.1b. While drifting, the charges couple with the electrodes, inducing current in the circuit, which is explained by the Shockley–Ramo theorem below. Upon reaching the electrodes the charges stop inducing the current. The equivalent electrical circuit is shown in figure 2.1c.

Mean energy loss of a particle traversing the detector as a function of the momentum is given with the the Bethe-Bloch equation []:

$$-\left\langle \frac{dE}{dx} \right\rangle = \frac{4\pi}{m_e c^2} \cdot \frac{n z^2}{\beta^2} \cdot \left(\frac{e^2}{4\pi\epsilon_0} \right)^2 \cdot \left(\ln \left(\frac{2m_e c^2 \beta^2}{I \cdot (1 - \beta^2)} \right) - \beta^2 \right) \quad (2.2)$$

The resulting function for a muon is shown in figure 2.2. At a momentum of around 300 MeV/c the particle deposits the lowest amount of energy. That is called a minimum ionising particle or a MIP.

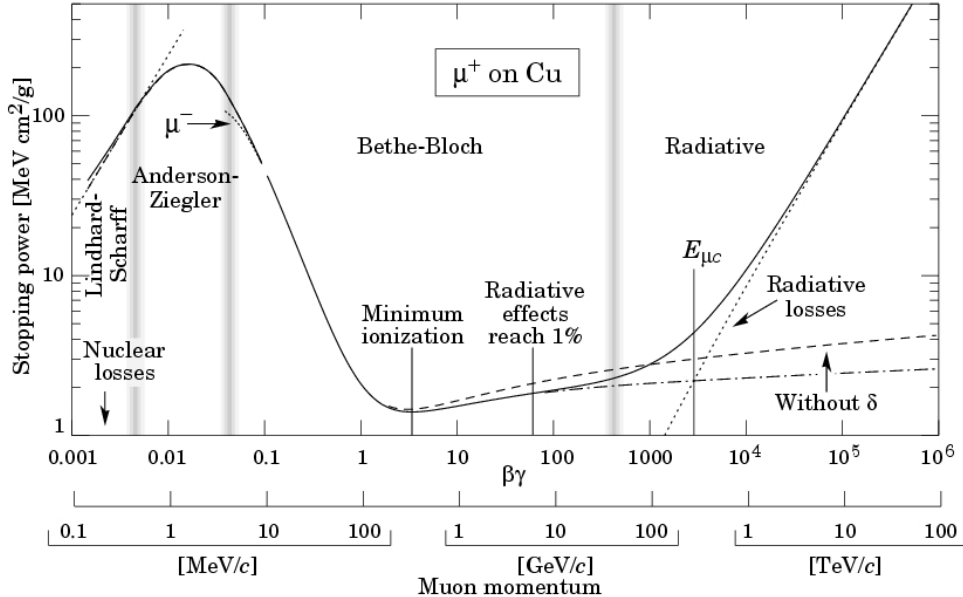


Figure 2.2: Stopping power for muons according to the Bethe-Bloch formula [].

688 2.1.1 Signal induction by moving charges

689 The signal induction in a conducting plane by a point-like charge, which couples with
 690 an electrode, is derived in [16]. The electrode can in this case be modelled as an
 691 infinite conducting plane. When a point charge q is created (e.g. an electron-hole
 692 pair created via ionisation), its electrostatic field lines immediately couple with the
 693 electrode, as seen in figure 2.3a. The electric field on the metal surface due to a
 694 point-like charge q at the distance z_0 is

$$E_z(x, y) = \frac{q z_0}{2\pi\epsilon_0(x^2 + y^2 + z_0^2)^{\frac{3}{2}}} \quad E_y = E_z = 0. \quad (2.3)$$

695 A mirror charge appears on the conducting plane, with a charge density distribution

$$\sigma(x, y) = \epsilon_0 E_z(x, y) = \frac{q z_0}{2\pi(x^2 + y^2 + z_0^2)^{\frac{3}{2}}}. \quad (2.4)$$

696 The charge density integrated over the entire plane yields a mirror charge Q , which
 697 is an opposite of point charge q :

$$Q = \int_{-\infty}^{\infty} \int_{-\infty}^{\infty} \sigma(x, y) dx dy = -q. \quad (2.5)$$

698 The plane is then segmented into infinitely long strips with a width w whereby each
 699 of the strips is grounded, as shown in figure 2.3c. Considering a charge density
 700 distribution 2.4, the resulting mirror charge on a single strip Q_2 directly below the
 701 point charge ($x = 0, y = 0$) yields

$$Q_2(z_0) = \int_{-\infty}^{\infty} \int_{-w/2}^{w/2} \sigma(x, y) dx dy = -\frac{2q}{\pi} \arctan\left(\frac{w}{2z_0}\right) \quad (2.6)$$

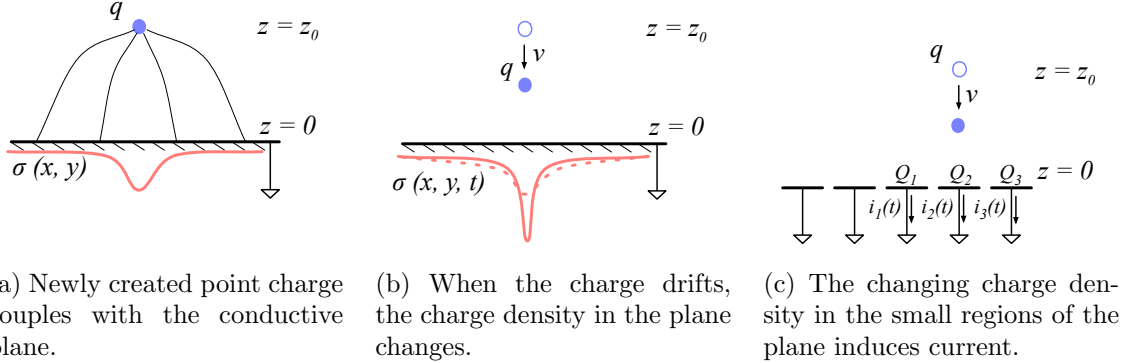


Figure 2.3: A point-like charge inducing current in a conductive plane.

If the charge starts moving towards the conducting plane, the mirror charge density distribution also changes, as shown in figure 2.3b. As a result the $Q_2[z(t)]$ changes with time. The changing charge is in effect an induced electric current $i_2(t)$:

$$i_2(t) = -\frac{d}{dt}Q_2[z(t)] = -\frac{\partial Q_2[z(t)]}{\partial z}\frac{\partial z(t)}{\partial t} = \frac{4qw}{\pi[4z(t)^2 + w^2]}v. \quad (2.7)$$

The movement of the point-like charge therefore induces current in the conducting plane. The induced current is linearly dependent on the velocity of the point-like charge.

2.1.2 Shockley-Ramo theorem

W. Shockley [42] and S. Ramo [40] independently proposed a theory which explains how a moving point charge induces current in a conductor. The Shockley-Ramo theorem can therefore be used to calculate the instantaneous electric current induced by the charge carrier or a group of charge carriers. It can be used for any number of electrodes. It states that the current $I_n^{\text{ind}}(t)$ induced on the grounded electrode n by a point charge q moving along a trajectory $\mathbf{x}(t)$ reads

$$I_n^{\text{ind}}(t) = -\frac{dQ_n(t)}{dt} = -\frac{q}{V_w}\nabla\Psi_n[\mathbf{x}(t)]v(t) = -\frac{q}{V_w}\mathbf{E}_n[\mathbf{x}(t)]v(t), \quad (2.8)$$

where $\mathbf{E}_n(\mathbf{x})$ is the *weighting field* of electrode n in the case where the charge q is removed, electrode n is set to voltage $V_w = 1$ and all other electrodes are grounded. The weighting field is defined as the spatial differential of the *weighting potential*: $\mathbf{E}_n(\mathbf{x}) = \nabla\Psi_n(\mathbf{x})$. In the case of two parallel electrodes, the weighting field is $E_w = -\frac{d\Psi}{dx} = -1/d$, where d is the distance between the electrodes. The resulting induced current is therefore

$$i(t) = \frac{q}{d}v_{\text{drift}}(x, t), \quad (2.9)$$

whereby v_{drift} is the drift velocity of the point-like charge and d is the distance between the electrodes. d is defined by the dimensions of the sensor. The drift velocity is a

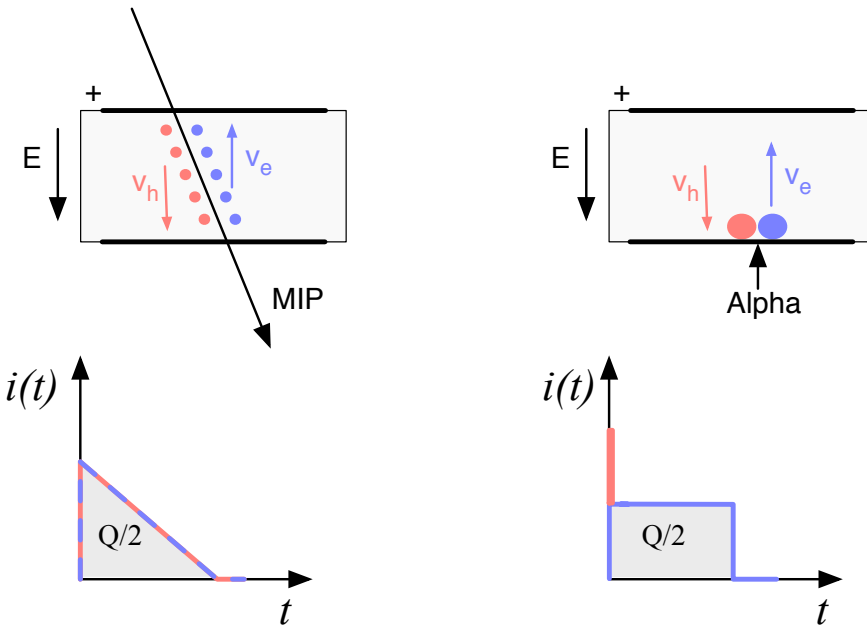


Figure 2.4: Charge carrier drift in diamond for β/γ and for α particles crossing the sensor at $t = 0$.

function of the externally applied electric field, as defined in section 2.2. If the electric field is set to a constant value, the induced current is directly proportional to the drifting charge. Therefore, by measuring the height of the induced current at a specific point of time the number of moving charges can be deduced.

2.1.3 Radiation-induced electrical pulses

When a highly-energetic particle travels through the sensor, it interacts with atoms in the lattice. It ionises the valence electrons, creating electron-hole (e-h) pairs on its way. It can either deposit only a fraction of its energy and exit the sensor on the other side or it can get stopped in the bulk, depositing all of its energy. A special case is when it interacts with the core of the atom in the middle of the sensor via a nuclear interaction. All these various types interactions produce different amounts and different spatial distributions of e-h pairs. The induced electrical current therefore differs for different types of interaction. Two most frequent types are shown in figure 2.4. The first diagram shows the interaction of a minimum ionising particle. The electrons and holes are created all along the trajectory of the particle and immediately start drifting towards the positive and negative electrode, respectively. At the beginning, all charges drift and contribute to the induced current. Those closest to the electrodes have a very short drift path, reducing the induced current. Gradually all the charge carriers reach the electrode. The resulting current signal is a triangular

742 pulse with a sharp rising edge and a linear falling edge. The accumulated charge Q_s
 743 equals to the sum of the contributions of the positive and negative charge carriers.
 744 The second type of interaction happens when the particle is stopped in the diamond
 745 close to the point of entry. Most of its energy is deposited in a small volume close to
 746 the electrode. A cloud of charge carriers is created and the charges with the shorter
 747 path to the electrode disappear almost instantly. The carriers of the opposite charge,
 748 however, start drifting through the sensor to the other electrode. In an ideal diamond
 749 sensor, their velocity is constant throughout the drift up until they are collected at the
 750 opposite electrode. The contribution of the first charge cloud is a peak with a short
 751 time. The cloud drifting through the sensor, on the other hand, induces a current
 752 signal with a flat top. The resulting signal has a shape of a rectangle, with a spike in
 753 the beginning. The accumulated charge Q_s is equal to a half of the deposited charge
 754 by the stopped particle.

755 The two aforementioned types of interactions have well defined signal responses.
 756 Nuclear interactions on the other hand yield various results. The resulting signal
 757 shape depends on the decay products of the interaction, which can be α , β or γ
 758 quanta or other nuclei, inducing a mixed shaped signal.

759 2.1.4 Signal charge fluctuations

760 Two important sensor properties are the magnitude of the signal and the fluctua-
 761 tions of the signal at a given absorbed energy. They determine the relative resolution
 762 $\Delta E/E$. For semiconductors the signal fluctuations are smaller than the simple sta-
 763 tistical standard deviation $\sigma_Q = \sqrt{N_Q}$. Here N_Q is the number of released charge
 764 pairs, i.e. the ratio between the total deposited energy E_0 and the average energy
 765 deposition E_i required to produce an electron-hole pair. [] shows that the standard
 766 deviation is $\sigma_Q = \sqrt{F N_Q}$, where F is the Fano factor [] (0.08 for diamond and 0.115
 767 for silicon []). Thus, the standard deviation of the signal charge is smaller than ex-
 768 pected, $\sigma_Q \approx 0.3\sqrt{N_Q}$. The resulting intrinsic resolution of semiconductor detectors
 769 is

$$\Delta E_{\text{FWHM}} = 2.35\sqrt{F E E_i} \quad (2.10)$$

770 wherein $E_i(Si) = 3.6$ eV and $E_i(C) = 13$ eV. E.g., for an α particle with energy E_α
 771 = 5.486 MeV the calculated resolution in diamond is equal to $\Delta E_{\text{FWHM}} = 5.6$ keV.
 772 This defines the minimum achievable resolution for energy spectroscopy with semi-
 773 conductors. Figure 2.5 shows the resolution limit as a function of energy in silicon
 774 and diamond.

775 2.2 Carrier transport in a diamond sensor

776 This section describes the carrier transport phenomena in diamond. This theory
 777 provides the basis for discussion about the measurements in chapter 3.

778 When the charge carriers are freed in a semiconductor with no concentration
 779 gradient and without an externally applied electric field, they scatter in random

2.2. CARRIER TRANSPORT IN A DIAMOND SENSOR

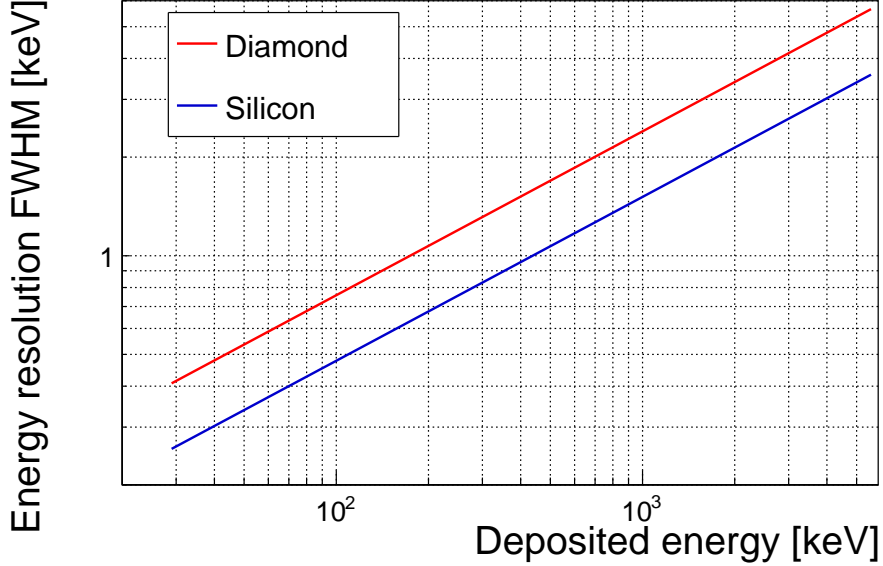


Figure 2.5: Calculated intrinsic energy resolution for silicon and diamond.

780 directions with a thermal velocity v_{th}]. Their integral movement due to thermal
781 excitation equals zero.

782 **Diffusion** Diffusion is caused by the concentration gradient. In its presence the in-
783 tegral movement is in the direction of the lower concentration until an equilibrium is
784 reached. The concentration profile dissolves with time forming a Gaussian distribu-
785 tion with variance $\sigma(t) = \sqrt{Dt}$] .

786 **Drift** Drift is caused by an externally applied electrical field. In that case the car-
787 riers move along the field lines. In a sensor with a high applied field the diffus-
788 ion contribution is negligible.

789 **Drift velocity, saturation velocity and mobility** The charge carriers drift through
790 the diamond bulk with a drift velocity $v_{\text{drift}}(E)$], which is proportional to the electric
791 field E at low electric fields: $v_{\text{drift}} = \mu E$. The proportionality factor μ is defined as
792 the mobility in $\text{cm}^2 \text{V}^{-1} \text{s}^{-1}$.

793 For higher fields and higher velocities, however, the carriers lose more energy to the
794 lattice. They induce increasingly more lattice vibrations (phonon transport). There
795 is a velocity limit above which the carriers cannot reach – velocity saturation. The
796 $v_{\text{sat}}^e = v_{\text{sat}}^h = (14.23 \pm 0.12) \times 10^6 \text{ cm/s}$ for both positive and negative charge carriers
797 has been derived from the measurements in [27].

798 The final equation for v_{drift} is therefore

$$v_{\text{drift}}(E) = \mu(E)E = \frac{\mu_0 E}{1 + \frac{\mu_0 E}{v_{\text{sat}}}} \quad (2.11)$$

799 where μ_0 is the low field mobility and v_{sat} is saturation velocity. The drift velocity can
 800 be retrieved experimentally via the transit time measured with the Transient Current
 801 Technique (TCT). This technique enables the measurement of transit time t_t of the
 802 carriers through the sensor with the thickness d .

$$v_{\text{drift}}(E) = \frac{d}{t_t(E)}. \quad (2.12)$$

803 The velocities for holes and electrons usually differ. In diamond, the holes travel
 804 30 % faster than electrons []. The measurements in chapter 3 empirically confirm this
 805 statement.

806 **Space charge** The Poisson equation shows that

$$\frac{d^2\Phi(x)}{dx^2} = \frac{dE(x)}{dx} = \frac{\rho(x)}{\epsilon} \quad (2.13)$$

807 where $\rho(x)$ is the space charge distribution, E is the electrical field and Φ is the
 808 voltage potential. In an ideal diamond, the externally applied high voltage potential
 809 on the two electrodes decreases linearly through the bulk. The electrical field is
 810 therefore constant throughout the sensor and the space charge distribution across it
 811 equals 0. However, space charge may be introduced in the bulk either by means of
 812 accumulating of charge carriers in the lattice (i.e. charge trapping) or already during
 813 sensor production. The space charge can be either permanent or changing – sometimes
 814 it is possible to reduce it, as is shown in chapter 3. All in all, it is very important to
 815 reduce it because it affects the shape of the electrical signal. Since the drift velocity
 816 of the charge carriers is proportional to the electrical field, the charges change their
 817 velocity while drifting through the space charge region. Figure 2.6 compares the
 818 voltage potential, the electrical field and the space charge for an ideal sensor as well
 819 as for that with a uniformly distributed positive space charge.

820 **Radiation damage** The bonds in the diamond lattice are very strong. However,
 821 when highly energetic particles hit the diamond, they can damage the crystal struc-
 822 ture. Figure 2.7 shows several examples of lattice damage:

- 823 a) foreign interstitial (e.g. H, Li),
- 824 b, c) foreign substitutional (e.g. N, P, B),
- 825 d) vacancy and
- 826 e) self interstitial.

827 These non-uniformities form new energy levels in the forbidden gap – the separation
 828 between the conductive and valence band in which the electrons. These intermediate
 829 levels are referred to as charge traps because they can trap moving charge carriers.
 830 The energy level of the trapped carriers is reduced from the conduction band to
 831 the energy level of the trap. Different types of lattice damage have different energy

2.2. CARRIER TRANSPORT IN A DIAMOND SENSOR

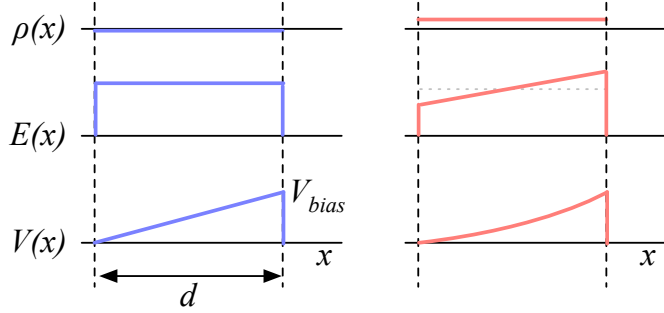


Figure 2.6: Left figure shows a profile of a diamond sensor only with an externally applied electric field. In the figure on the right a uniformly distributed space charge is added in the diamond, contributing to the internal electric field distribution. The induced current signal is proportional to the electrical field. d is the thickness of the diamond sensor.

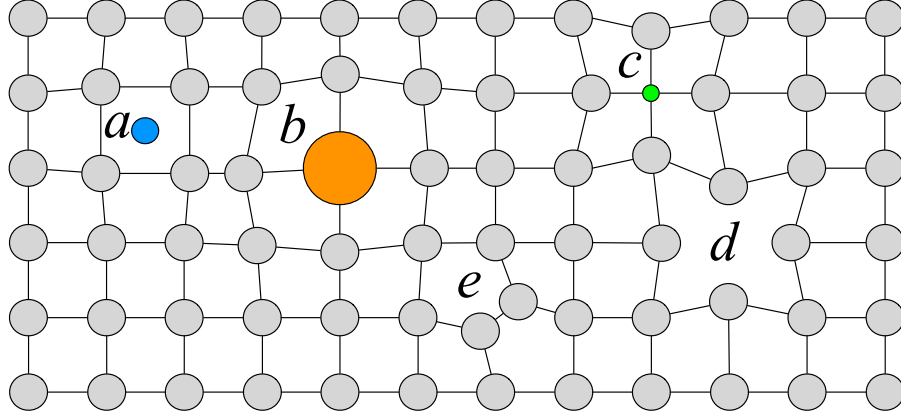


Figure 2.7: Impurities and non-uniformities in the crystal lattice due to radiation damage.

832 levels. The carriers trapped in an energy level close to the conduction band have a
 833 high probability of being thermally excited back into the conduction band whereby
 834 they continue drifting towards the electrode. Their activation energy is therefore low.
 835 Those trapped in a deep trap close to the middle of the forbidden gap need a much
 836 higher activation energy, which in turn increases the average time to their release due
 837 to thermal excitation.

838 The trapped carriers do not contribute to the overall induced current on the elec-
 839 trodes. The more charges are trapped along their drift path, the lower current is
 840 induced on the electrodes.

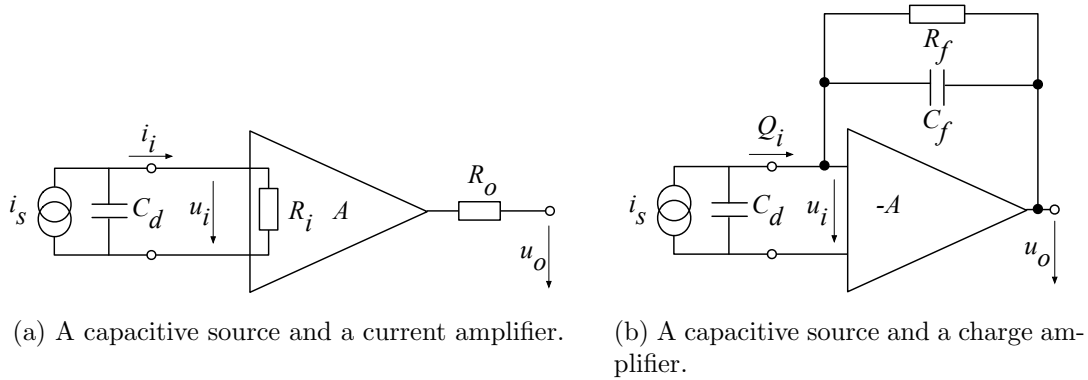


Figure 2.8: Simplified equivalent circuits of a current and charge amplifier.

841 2.3 Electronics for signal processing

842 This section describes the electronics of a detector, starting with a description of
 843 signal amplifiers and then discussing the digitisation and signal processing. All these
 844 stages are necessary to extract information from the sensor. First, the signal has to be
 845 amplified. Then it is digitised and finally processed in a specially designed processor
 846 or a logic unit.

847 2.3.1 Signal preamplifiers

848 The signal charge generated in the sensor by a single energetic particle is of the order
 849 of fC. The induced current range is typically between 10^{-8} A (β, γ radiation) and
 850 3×10^{-7} A (α radiation). Signals as low as these have to be pre-amplified before
 851 processing. Depending on the measurement, several types of signal amplifiers can be
 852 used. The preamplifiers are designed to minimise electronic noise while maximising
 853 gain, thus maximising the signal-to-noise ratio (SNR). In addition, a high bandwidth
 854 limit is preferred to minimise the information loss due to signal shape deformation.
 855 A critical parameter is the total capacitance, i.e. the sensor capacitance together
 856 with the input capacitance of the preamplifier. The SNR improves with a lower
 857 capacitance. Several types of amplifiers can be used, all of which affect the measured
 858 pulse shape. Two preamplifiers are used most commonly, a current and a charge
 859 sensitive amplifier. Both are described in detail below.

860 2.3.1.1 Current-sensitive amplifier

861 Figure 2.8a shows the equivalent circuit of a capacitive source and a current amplifier.
 862 An amplifier operates in current mode if the source has a low charge collection
 863 time t_c with respect to the $R_i C_d$ time constant of the circuit. In this case the sensor
 864 capacitance discharges rapidly and the output current i_o is proportional to the in-
 865 stanceous current i_i . The amplifier is providing a voltage gain, so the output signal

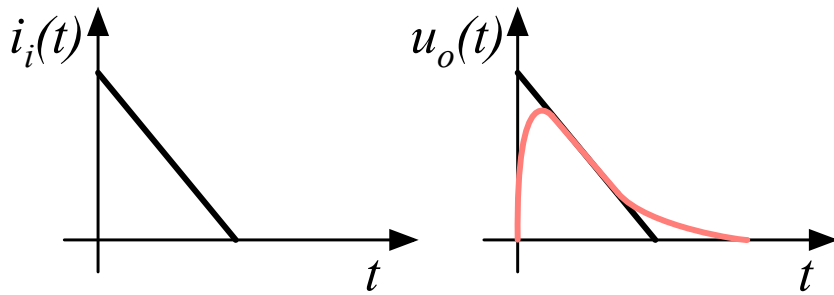


Figure 2.9: Input and output signal of the current amplifier.

866 voltage u_o is directly proportional to the input voltage u_i :

$$u_o(t) = A \cdot R_i \cdot i_s(t). \quad (2.14)$$

867 The detector capacitance C_{det} together with the input resistance of the amplifier R_i
868 defines the time constant of the signal, as shown in figure 2.9. The higher the C_{det} ,
869 the slower is the response of the amplifier. For the case of the diamond sensor, which
870 has the capacitance of the order of 2 pF and the input resistance of 50 Ω , the resulting
871 time constant is $\tau = 10^{-10}$ s. This yields the signal rise time $t_r \sim 2.2\tau = 2.2 \times 10^{-10}$ s.
872

873 2.3.1.2 Charge-sensitive amplifier

874 In order to measure integrated charge in the sensor, a feedback loop is added to the
875 amplifier, as shown in figure 2.8b. The feedback can be used to control the gain and
876 input resistance, as well as to integrate the input signal. The charge amplifier is in
877 principle an inverting voltage amplifier with a high input resistance.

878 In an ideal amplifier the output voltage u_o equals $-Au_i$. Therefore the voltage
879 difference across the capacitor C_f is $u_f = (A + 1)u_i$ and the charge deposited on the
880 capacitor is $Q_f = C_f u_f = C_f(A + 1)u_i$. Since no current can flow into the amplifier,
881 all of the signal current must charge up the feedback capacitance, so $Q_f = Q_i$.

882 In reality, however, charge-sensitive amplifiers respond much slower than is the
883 duration of the current pulse from the sensor. In addition, a resistor is added to the
884 feedback line in parallel to the capacitor. The resistor and capacitor define the decay
885 time constant of the pulse, as shown in figure 2.10. This is necessary to return the
886 signal to its initial state to be ready for a new measurement.

887 2.3.1.3 Analogue electronic noise

888 The electronic noise determines the ability of a system to distinguish different signal
889 levels. The analogue signal contains ample information about the type and energy

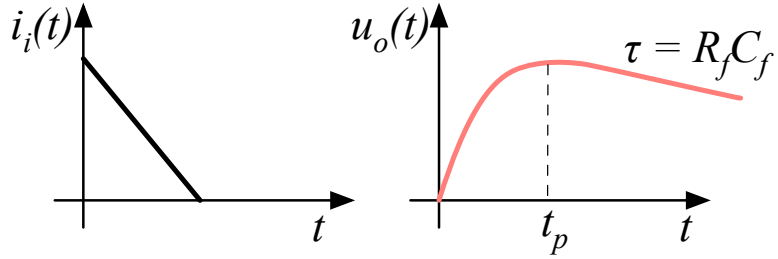


Figure 2.10: Input and output signal of the charge amplifier.

of incident radiation, which can quickly be erased or altered if the signal properties change. Therefore the noise contributions to the signal must be well understood to qualify the information the signal is carrying. The important contributions are listed below. Thermal or Johnson–Nyquist [6] noise is the dominant noise contribution in the use case for diamond detector signal amplification and therefore defines the limitations of the detector system. This noise type is generated by the random thermal motion of charge carriers. The frequency range of the thermal noise is from 0 to ∞ with a predominantly uniform distribution. Therefore this is nearly a white noise. The resulting signal amplitude has a Gaussian distribution. The RMS of the noise amplitude is defined as

$$u_{\text{RMS}} = \sqrt{4k_BRT\Delta f} \quad (2.15)$$

where k_B is the Boltzmann constant, R is the input resistance of the amplifier, T its temperature and Δf the frequency range. This equation shows that it is possible to reduce the noise RMS by either (1) reducing the frequency range, (2) reducing the resistance of the conductor or (3) cooling the conductor.

Contributions of shot noise, flicker noise and burst noise and other types are not significant relative to the thermal noise. However, the contributions of external factors can severely deteriorate the signal. This means the noise produced by capacitive or inductive coupling with an external source, which causes interference in the signal. These effects can be reduced by shielding the electronics and avoiding ground loops.

2.3.2 Analogue-to-digital converters

An analogue-to-digital converter (ADC) is a device that converts the analogue electrical signal on the input to its digital representation - a series of digital values. This involves a quantisation – *sampling* of the signal at a defined sampling period, resulting in a sequence of samples at a discrete time period and with discrete amplitude values. The resolution of the ADC is the number of output levels the ADC can quantise to and is expressed in bits. For instance, an ADC with a resolution equal to $n = 8$ bit has a dynamic range of $N = 2^n = 256$ steps. The resulting voltage resolution Q_{ADC}

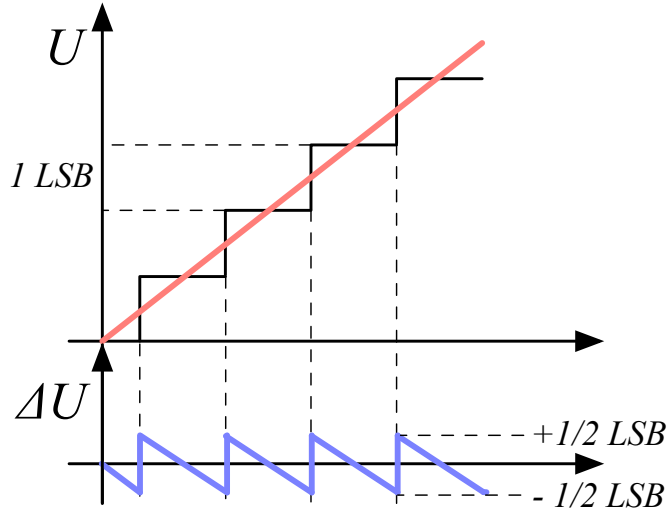


Figure 2.11: Input signal digitisation and quantisation error.

₉₁₇ at the input voltage range of $V_{\text{ADC}} = \pm 50 \text{ mV}$ is then

$$Q_{\text{ADC}} = \frac{V_{\text{ADC}}}{2^n} = \frac{100 \text{ mV}}{2^8 \text{ bit}} = 0.39 \text{ mV/bit.} \quad (2.16)$$

₉₁₈ With a sampling period of $t_s = 1 \text{ ns}$ the sampling rate is $f_s = 1 \text{ GS/s}$ (gigasample per ₉₁₉ second).

Quantisation error and quantisation noise (or a round-off error) is a contribution to the overall measurement error due to digitisation (rounding). The quantisation error is defined as a difference between the actual analog value and the closest digitised representation of this value, therefore by the least significant bit (LSB), as seen in figure 2.11. The input signal amplitude is typically much larger than the voltage resolution. In this case the quantisation error is not directly correlated with the signal and has an approximately uniform distribution \square . The probability density function $P(x)$ therefore has a rectangular shape bounded by $(-\frac{1}{2}\text{LSB}, \frac{1}{2}\text{LSB})$:

$$P(x) = \begin{cases} \frac{1}{\text{LSB}}, & -\frac{1}{2}\text{LSB} \leq x \leq \frac{1}{2}\text{LSB} \\ 0, & \text{otherwise.} \end{cases} \quad (2.17)$$

₉₂₀ The height equal to $\frac{1}{\text{LSB}}$ preserves the integrated probability of 1. The variance of ₉₂₁ the distribution is

$$\sigma^2 = \int P(x)(x - \mu)^2 dx. \quad (2.19)$$

₉₂₂ The population mean is $\mu = 0$, therefore

$$\sigma^2 = \int_{-\frac{1}{2}\text{LSB}}^{\frac{1}{2}\text{LSB}} \frac{1}{\text{LSB}} x^2 dx = \frac{x^3}{3\text{LSB}} \Big|_{-\frac{1}{2}\text{LSB}}^{\frac{1}{2}\text{LSB}} = \frac{\text{LSB}^2}{12}. \quad (2.20)$$

923 The RMS of the quantisation noise is defined as the square root of the variance:

$$\Delta Q_{\text{ADC}} = \sqrt{\sigma^2} = \frac{1}{\sqrt{12}} \text{LSB} \sim 0.289 \text{ LSB}. \quad (2.21)$$

924 For the example above the quantisation error equals $\Delta Q_{\text{ADC}} = 0.289 \cdot 0.39 \text{ mV} =$
 925 0.11 mV . The error depends strongly on the linearity of the ADC, but this is out of
 926 scope of this document as the devices used have ADCs with a very good linearity.

927 2.3.3 Digital signal processing

928 The digitised signal can be processed to extract useful information. Therefore after
 929 the signal amplification and digitisation the signal is routed in a device which handles
 930 the digital analysis. The signal can either be processed immediately (in real time) or
 931 it can be saved to a data storage for analysis at a later stage (offline). The devices
 932 carrying out the processing can be multipurpose (e.g. Field Programmable Gate
 933 Arrays) or dedicated (e.g. Application-Specific Integrated Circuits).

934 **Field Programmable Gate Array** (FPGA) is an integrated circuit designed to be
 935 reprogrammable and reconfigured after manufacturing. It consists of a set of logic
 936 gates that can be interconnected in numerous combinations to carry out a set of
 937 logic operations. Many such logic operations can take place in parallel, making the
 938 FPGA a powerful tool for signal processing. FPGAs are often used during system
 939 development or in systems in which the requirements might change with time. They
 940 can be reprogrammed in the order of seconds. In addition, the logic design only needs
 941 minor changes when migrating to a newer version of the FPGA chip of the same
 942 vendor. The FPGAs also offer faster time-to-market with comparison to application-
 943 specific solutions, which have to be developed. On the other hand, the price per
 944 part can be significantly higher than for the application-specific solutions. Also, their
 945 other major disadvantages are a high power consumption and a relatively low speed
 946 as compared to more application-specific solutions. However, today's solutions are
 947 capable of clock speeds higher than 500 MHz. Together with the integrated digital
 948 signal processing blocks, embedded processors and other modules, they are already
 949 very powerful and versatile. All in all, FPGAs are a good choice for prototyping and
 950 limited production, for projects with limited requirements for speed and complexity.

951 **Application-Specific Integrated Circuit** (ASIC) is an integrated circuit designed
 952 for a specific use. The design cannot be modified after chip production, as is the case
 953 with FPGAs. On the other hand, the ASICs can be optimised to perform a required
 954 operation at a high speed and at a low power consumption. In addition, due to the
 955 specific design the size of the chip can be much smaller. ASICs can be designed as
 956 hybrid chips, containing both a digital and an analog part. Finally, ASICs can be
 957 designed to withstand much higher irradiation doses than FPGAs and can therefore
 958 be used in harsh environments like in space or in particle colliders.

2.3. ELECTRONICS FOR SIGNAL PROCESSING

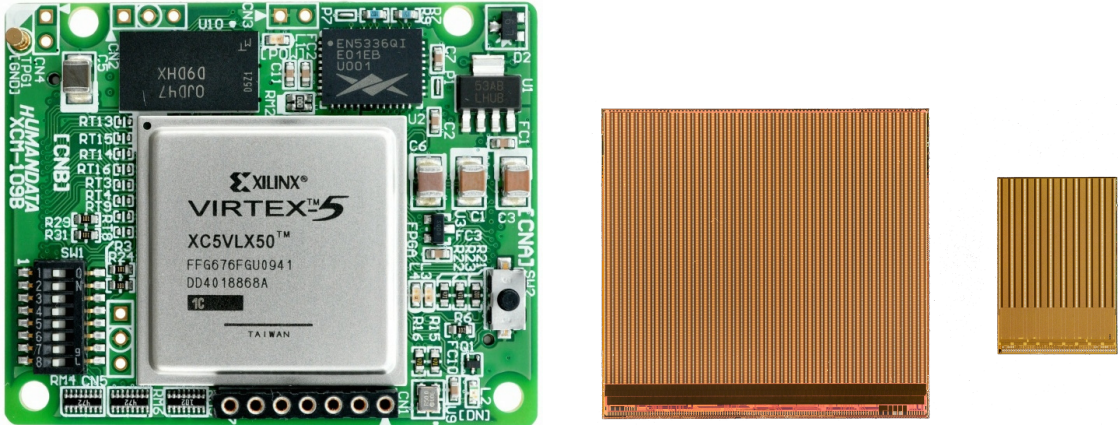


Figure 2.12: An example of a Xilinx Virtex 5 FPGA [12] and an FE-I4 and FE-I3 ASIC chip [21].

959 To update the chip, the design has to be submitted to a foundry, which produces
960 the new chips with a turnover time of 4—6 weeks. The costs of a submission start
961 at \$ 50 000, but the price per part can be reduced significantly with a high volume.
962 To sum up, ASICs are used for high volume designs with well defined requirements
963 where some stringent constraints in terms of power consumption and speed have to
964 be met.

⁹⁶⁵ Chapter 3

⁹⁶⁶ Diamond irradiation study

⁹⁶⁷ The aim of the study in this chapter is to find the operational limitations of diamond
⁹⁶⁸ detectors for spectroscopy and tracking applications. The chapter contains the mea-
⁹⁶⁹ surement results of data taken with diamond sensors. First the measurement setup
⁹⁷⁰ is described in section 3.1. Then the measured particle spectra are shown in 3.2.
⁹⁷¹ This is followed by a study of effects of the irradiation damage on the electrical signal
⁹⁷² of the diamond detector. The last section shows the results of the measurements
⁹⁷³ of irradiated diamond samples at cryogenic temperatures. The studies compare the
⁹⁷⁴ experimentally acquired data with the theory from the previous chapter and define
⁹⁷⁵ limitations of the diamond detectors in terms of noise, radiation and temperature.

⁹⁷⁶ Diamond sensors are mainly used for two types of measurements: particle counting
⁹⁷⁷ and spectroscopy. The first type of measurements depends on the sensor efficiency –
⁹⁷⁸ its ability to detect all or at least a known percentage of incident particles. The energy
⁹⁷⁹ of the particles is not so important; what bears the information is the rate and the
⁹⁸⁰ spatial distribution. Here the particles do not necessarily stop in the bulk, but rather
⁹⁸¹ continue their way. In spectroscopy, on the other hand, the particles stop within the
⁹⁸² sensor, depositing all their energy. This energy is then measured by collecting the
⁹⁸³ freed charge carriers. The goal of the experiments described in this chapter is to:

- ⁹⁸⁴ 1. Quantify the efficiency of the sCVD diamond in counting mode,
- ⁹⁸⁵ 2. Quantify the degradation of the efficiency as a function of the received radiation
dose,
- ⁹⁸⁷ 3. Quantify the macroscopic effects on charge carrier behaviour as a function of
the received radiation dose and
- ⁹⁸⁹ 4. Define limitations for use in spectroscopy.

⁹⁹⁰ The results discussed here show that there are several limitations for using diamond as
⁹⁹¹ a radiation detector. All of them need to be taken into account when designing a new
⁹⁹² measurement device. The irradiation study allows for an estimation of the lifetime of
⁹⁹³ the detector and a prediction of the longterm signal degradation as a function of the
⁹⁹⁴ received radiation dose. The result of the study is a correction factor, which can be

3.1. MEASUREMENT SETUP

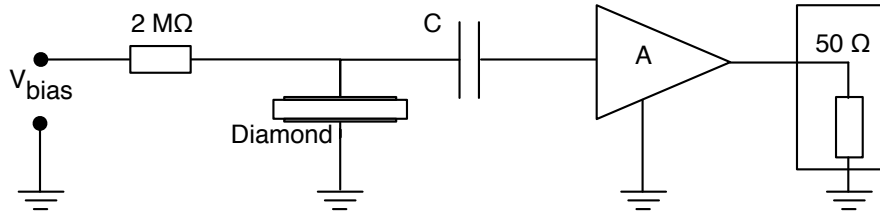


Figure 3.1: Diagram of a diamond detector readout chain.

995 applied during data analysis to ensure that the analysis results are stable despite the
996 detector degradation.

997 3.1 Measurement setup

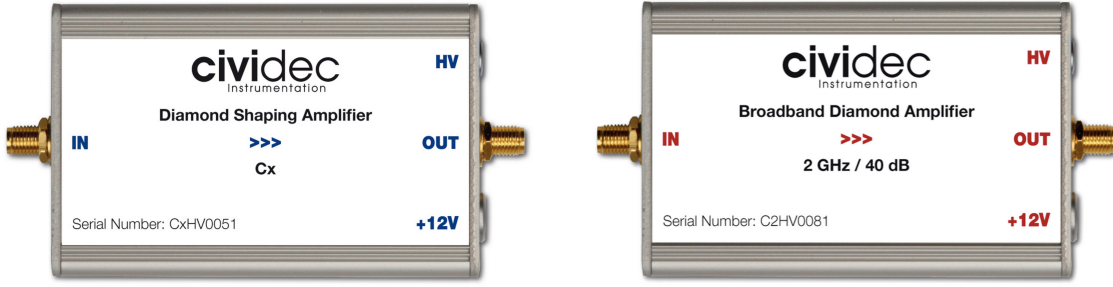
998 The first step of designing a measurement setup is to define the measurement conditions
999 such as the temperature, the type of radiation and its flux. The second step is
1000 to ensure that the setup is insensitive to external electromagnetic interferences and
1001 that it minimises electrical noise in the system. The setup needs to be calibrated
1002 before use.

1003 Shielding has to be applied wherever possible. For instance, aluminium foil can
1004 be wrapped around the exposed parts of the system to shield them from external
1005 radio-frequency (RF) interferences. In addition, the sensors have to be covered to
1006 prevent the exposure to light. The incident photons may deposit enough energy to
1007 increase the leakage current of the detector, which produces unwanted results.

1008 The measurements using diamond that are explained in these chapters have been
1009 carried out using several measurement setups, but they are all similar in terms of
1010 the electrical signal chain. The measurement chain consists of three main parts: a
1011 diamond sensor, a signal preamplifier and a readout device, as seen in figure 3.1. The
1012 signals propagating along the analogue chain are fast – in the GHz bandwidth range –
1013 and with low amplitudes – of the order of tens of μV . This gives rise to the importance
1014 of RF shielding. Also, the connection between the carrier and the preamplifier has
1015 to be as short as possible to avoid capacitive signal losses in the transmission line.
1016 Finally, the system needs to be grounded properly.

1017 3.1.1 Preamplifiers

1018 Two preamplifiers are used for the measurements, one sensitive to charge and the
1019 other to current. *CIVIDEC Cx* (figure 3.2a) is a charge sensitive amplifier. Its high
1020 SNR is achieved due to a low equivalent noise charge of 300 e^- with an additional
1021 30 e^- per each pF of the sensor capacitance. A reported gain of $\sim 12 \text{ mV/fC}$ makes
1022 it a good choice for spectroscopic measurements with diamond sensors. *CIVIDEC*
1023 *C2* (figure 3.2b) is a fast current preamplifier with a 2 GHz bandwidth limit. It is
1024 used for TCT measurements because of its fast response and a good SNR. Both are



(a) Cx charge sensitive preamplifier.

(b) C2 fast charge preamplifier.

Figure 3.2: Amplifiers used for the charge and current measurements.

1025 embedded in an RF-tight aluminium box to reduce the noise pickup. Both have an
1026 AC coupled input and an output with a 50Ω termination.

1027 3.1.1.1 Calibration

1028 The amplifiers have to be calibrated before use to determine their gain. Both are
1029 calibrated using a square signal generator with a known amplitude step of $U_{\text{in}} =$
1030 (252 ± 5) mV. A 2 GHz oscilloscope with a 10 GS/s sampling rate is used to carry
1031 out these measurements.

1032 **Cx charge sensitive amplifier** calibration necessitates an injection of a well known
1033 charge. Therefore the signal from a pulse generator is routed through a capacitor with
1034 a calibration capacitance $C_{\text{cal}} = (0.717 \pm 0.014)$ pF and then to the input of the am-
1035 plifier. The pulse area behind the capacitor is $a_{\text{cal}} = (5.0 \pm 0.5)$ pVs, with the signal
1036 amplitude on the output amounting to $U_{\text{Cx}} = (1.95 \pm 0.05)$ V. The input voltage step
1037 combined with the calibration capacitance yields a calibration charge

$$Q_{\text{cal}} = C_{\text{cal}} \cdot U_{\text{in}} = (181 \pm 5) \text{ fC}. \quad (3.1)$$

1038 The gain of the Cx amplifier when comparing the integrated input charge to the
1039 output amplitude is

$$A_{\text{Cx}}^Q = \frac{U_{\text{Cx}}}{Q_{\text{cal}}} = (9.3 \pm 0.4) \text{ mV/fC} \quad (3.2)$$

1040 whereas the factor between the area of the input current pulse and the output am-
1041 plitude is

$$A_{\text{Cx}}^a = \frac{U_{\text{Cx}}}{a_{\text{cal}}} = (390 \pm 40) \text{ mV/pVs}. \quad (3.3)$$

1042 The area-based amplification factor A_{Cx}^a can be used as an estimate for the integrated
1043 charge of a current pulse. However, it has a higher uncertainty ($\sim 10\%$) than
1044 the amplitude-based factor A_{Cx}^Q ($\sim 4\%$) due to the measurement limitations of the
1045 oscilloscope.

3.1. MEASUREMENT SETUP

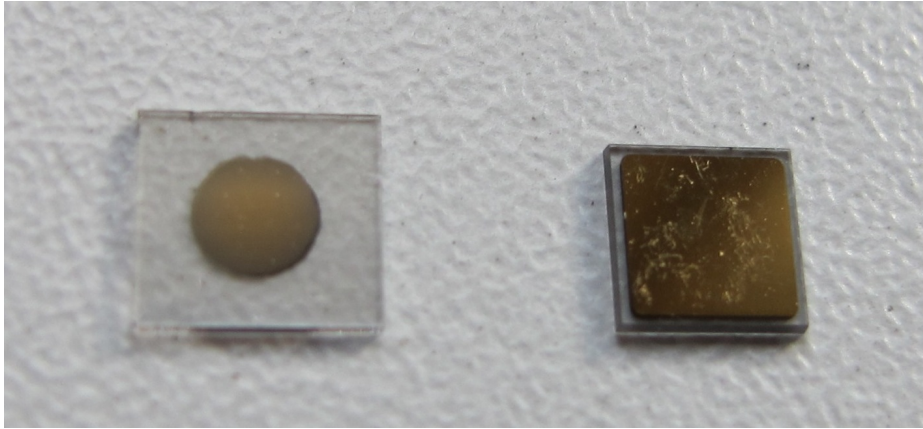


Figure 3.3: Two scCVD diamond samples: A IIa 1scdhq (left) and an E6 S37 (right).

1046 **C2 current amplifier** calibration only requires the measurement of the amplitude
1047 gain. To keep the output signal amplitude within the ± 1 V linear range of the
1048 amplifier, the input signal amplitude has to be minimised. The signal from the
1049 generator is therefore routed through a 36 dB attenuator to decrease its amplitude to
1050 $U_{\text{inAtt}} = (3.95 \pm 0.05)$ mV. Two amplifiers with different gains have been measured,
1051 because both are used for the measurements. The output of the first amplifier amounts
1052 to $U_{\text{C2-1}} = (860 \pm 5)$ mV. This yields the amplification gain

$$A_{\text{C2-1}} = \frac{U_{\text{inAtt}}}{U_{\text{C2-1}}} = (217 \pm 3). \quad (3.4)$$

1053 The second amplifier has the output equal to $U_{\text{C2-2}} = (632 \pm 5)$ mV with the resulting
1054 gain of $A_{\text{C2-2}} = (152 \pm 3)$.

1055 3.1.2 Diamond samples

1056 Detector-grade diamonds are very difficult to produce. The major challenge is to
1057 ensure a high enough purity of the lattice. The sensor samples used for these studies
1058 have been acquired from Element Six (E6) [4]. They all have the same standard
1059 dimensions. sCVD diamonds with dimensions 4.7×4.7 mm 2 are already sufficiently
1060 large for most of the beam monitoring applications and still affordable. One sample
1061 with dimensions of 5.6×5.3 mm 2 produced by IIa Singapore [6] has also been char-
1062 acterised at CERN [43]. The target thickness for all samples is 500 μm . Diamonds
1063 this thick yield a high enough signal-to-noise ratio for MIPs to be measured by the
1064 available electronics. Table 3.1 shows all the samples used for this study. Two of
1065 them are measured before and after irradiation and then compared. Irradiation doses
1066 for damaging the material need to be high – above 10^{12} particles per cm 2 to be able
1067 to observe a significant change in behaviour of a diamond sensor.

	Name	Type	Producer	Dimensions [mm ²]	Thickness [μm]	Electrode	Irradiated
S37	sCVD	E6		4.7 × 4.7	548	Cr/Au	no
S50	sCVD	E6		4.7 × 4.7	537	Cr/Au	no
S52	sCVD	E6		4.7 × 4.7	515	DLC/Pt/Au	$3.63 \times 10^{14} \pi \text{ cm}^{-2}$
S79	sCVD	E6		4.7 × 4.7	529	Cr/Au	$1 \times 10^{14} \pi \text{ cm}^{-2}$
ELSC	sCVD	E6		4.7 × 4.7	491	Cr/Au	no
1scdhq	sCVD	IIa		5.6 × 5.3	460	Cr/Au	no

Table 3.1: Diamond sensor samples used.

The diamond samples have quoted impurity densities of $\leq 2 \times 10^{14} \text{ cm}^{-3}$ and nitrogen incorporation of $\leq 10^{-9}$. The electrodes were added by various companies and institutes. For instance, S52 was metallised by a company DDL (now defunct) while the Physics Department of the University of Firenze, Italy metallised the S79. There are also several techniques for producing the electrodes. The DDL contacts consist of three layers: DLC (diamond-like carbon)/Pt/Au with 4/10/200 nm thicknesses, respectively. The metallisation for S79, on the other hand, is made up of Cr/Au with a total thickness of ~ 400 nm. The area coverage also differs from sample to sample. Diamonds must not be metallised until the very edge as the proximity of contacts with a high potential may lead to sparking. However, the areas not covered by the metallisation are less efficient because the fringe fields at the edges are not as strong as in between the electrodes. This effectively reduces the sensitive area of the sensors. In the diamonds used here the effective area is anywhere from 9 mm² to 18 mm². The leakage current through the bulk is below 1 nA, but increases for the irradiated samples. The capacitance is of the order of (2.0 ± 0.3) pF.

3.1.3 Readout devices

Electrical signals in diamond detectors are in the GHz frequency range. To preserve the information in the signals, the readout device with a high bandwidth limit must be used. For instance, a 250 MHz limit is enough for the spectroscopic measurements with the Cx charge amplifier, but might be insufficient for the current measurements with the C2 amplifier.

Two devices are used take data shown in this chapter. The first choice is a 2 GHz LeCroy WaveRunner 204MXi-A. This specific model has a sufficiently high bandwidth limit for the fast current preamplifier signals. It offers a reliable solution for analogue signal readout of limited amounts of data. However, its slow acquisition speed is a bottleneck in a test beam experiment. Its initial 100 Hz readout rate decreases to a mere 20 Hz within 20 minutes, because every single trigger is saved as a separate file and the Windows operating system is not capable of handling 10000+ files in a single directory easily. This is why it has been exchanged with a DRS4 [3], an analogue readout device developed by PSI, Switzerland. This compact device is capable of recording up to four waveforms at a time at a steady rate of up to 500 Hz. Its 700 MHz bandwidth limitation is sufficient for the signal from the charge amplifier.

3.1. MEASUREMENT SETUP

3.1.4 Setup for the efficiency study using β particles

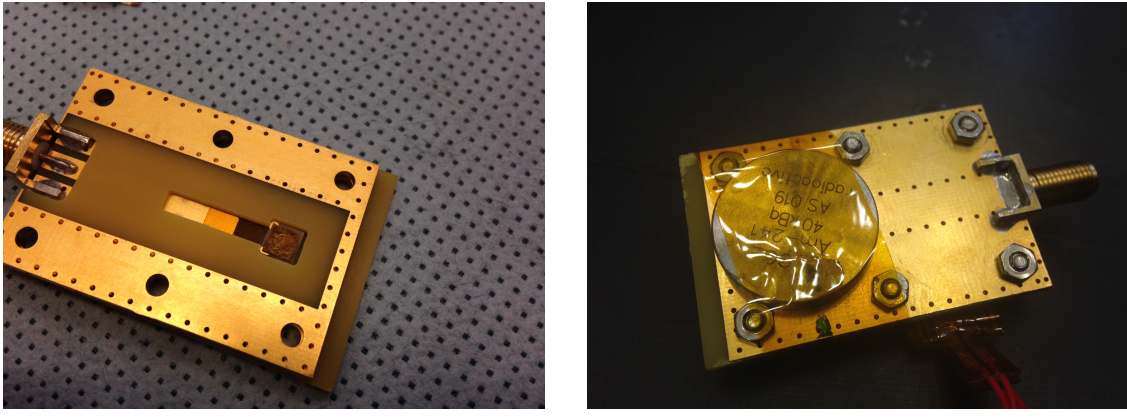
The efficiency study of the diamond sensors has been carried out at CERN in the North Hall test beam facility. There a straight high-energy particle beam of 120 GeV π is provided to the users to calibrate their detectors. The beam has a transverse spread of $\sigma = 10$ mm in both axes. The particle rate is of the order of $10^4 \pi \text{ cm}^{-2} \text{ s}^{-1}$. A diamond sensor embedded in a printed circuit board (PCB) carrier has been placed in the beam spot perpendicular to the beam and connected via an SMA connector directly to a charge amplifier. The amplified signal is read out using a LeCroy oscilloscope and a DRS4 analogue readout system. A computer is used as a controller and data storage for the readout device. A beam telescope is used as a reference detector. It is a device that helps to cross-check the measurements of the devices under test (DUTs) and to carry out spatially resolved studies on the DUTs. It consists of several pixellated sensor planes placed in series, which can track a particle's trajectory with a precision of a few μm . The sensor planes are positioned in front of the DUT and behind it. Then the beam telescope acts as a trigger system – it triggers the readout of both the telescope data and DUT data when both the planes in front and behind the DUT record a hit by an incident particle. A particle detected by all the planes within the DUT window and the DUT itself counts towards its efficiency whereas a hit missed by the DUT means that the DUT is not 100 % efficient. To discard the hits that miss the DUT completely, a region of interest (ROI) can be chosen in the beam telescope planes. The equation for calculating the sensor efficiency is therefore

$$\epsilon = \frac{N_{\text{DUT}} \wedge N_{\text{telescope}}}{N_{\text{telescope}}} \quad (3.5)$$

for an ROI smaller than the sensitive region of the diamond.

3.1.5 Room temperature α -TCT setup

This TCT study is a follow-up of an extensive diamond TCT study at cryogenic temperatures [28]. The room-temperature TCT measurements have been carried out in the laboratory. The setup consists of a diamond sensor embedded in a PCB carrier, a current amplifier and an oscilloscope. To measure α particles, their energy loss during their trajectory has to be minimised. Therefore the diamond is placed inside a vacuum chamber. The chamber is a steel tube with a diameter of 5 cm. On one side it is connected to a vacuum pump via a steel hose. A feedthrough with an SMA connector is placed on the other side. A CIVIDEC C2 current amplifier is connected directly onto the feedthrough. The amplified output is connected to the oscilloscope via an SMA cable. An ^{241}Am source with a diameter of 2 cm and a height of 0.5 cm is fixed onto the sensor carrier (figure 3.4a, figure 3.4b). Then the carrier is inserted in the chamber and fixed in place using an air-tight clamp. The pump can then be switched on. It is capable of providing the inside pressure as low as 10^{-4} mbar after approximately one hour of operation.



(a) PCB carrier with an embedded diamond sample.
 (b) Radioactive source over the carrier.

Figure 3.4: Positioning of the α -source on top of the sensor carrier.

3.1.6 Cryogenic α -TCT setup

The experiment at cryogenic temperatures has been carried out at the Central Cryogenic Laboratory at CERN. The room-temperature TCT setup has to be modified to allow for measurements at temperatures as low as 2 K. It consists of three parts:

1. a cryostat – a thermally insulated cylinder containing liquid helium,
2. an inlet – an air-tight mechanical tube with valves and feedthroughs at the top that is lowered in the liquid helium and
3. the diamond sample embedded in a PCB carrier with a fitted temperature sensor, a heater and cables leading to the feedthroughs.

The setup is described in detail in [28].

When the diamond sample is placed in the PCB carrier and the ^{241}Am source is in place, the inlet is sealed and lowered in the empty cryostat. Then the inside volume of the inlet is evacuated down to 10^{-5} mbar while the liquid helium is flowing into the cryostat. To improve the thermal contact between the diamond and the coolant, a small amount of helium gas is added inside the evacuated inlet, setting the vacuum to around 10^{-3} mbar. This value changes with time, because the gas condenses on the walls of the inlet, reducing the number of floating particles. For this reason the helium gas has to be added on an irregular basis. Every addition causes a significant undershoot of the sample temperature, which has to be corrected for using a heater placed on the back of the PCB carrier. Also, the added gas deteriorates the vacuum inside the inlet. Furthermore, at approximately 60 K the helium gas has to be evacuated from the inlet to avoid a potential explosion due to the expansion of the gas with temperature.

When the sample is cooled to the minimum temperature achievable by means of liquid helium without over-pressurising it (4.2 K), the measurements can begin. A

3.2. CHARGED PARTICLE PULSES AND SPECTRA

temperature sensor placed on the back of the PCB carrier is used to measure the temperature of the sample. After every temperature data point, the current through the heater placed in the PCB next to the diamond sample is increased, increasing the sample. The initial temperature time constant of the order of tenths of seconds at low temperatures increases with temperature. Even more so when helium is evacuated from the inlet at 60 K, removing the thermal bridge between the wall of the inlet and the diamond sample. At the room temperature (RT), the time constant is already of the order of minutes.

3.2 Charged particle pulses and spectra

In previous chapter the ionisation profiles for different types of radiation were discussed. β radiation induces a triangular electric pulse whereas α radiation induces a rectangular one. However, their amplitude, width and rise/fall time depend heavily on the type of interaction with the diamond, the purity of the diamond and the bandwidth of the amplifier and the oscilloscope. This section shows the signal pulses of α , β and γ radiation with their respective energy distributions for the case of a diamond detector. This is followed by a discussion of effects of noise on these measurements.

A CIVIDEC C2 current amplifier together with the LeCroy oscilloscope (both with a bandwidth limit of 2 GHz) is used to record the pulse shapes whereas the Cx charge amplifier is used for charge measurements. A 2 GHz bandwidth limit defines the minimum rising time equal to $t_r \simeq \frac{0.34}{BW} = \frac{0.34}{2 \times 10^9} = 170$ ps, therefore the system is capable of measuring pulses with a minimum FWHM $\simeq 170$ ps. This already makes it impossible to measure the initial peak in the α response due to the two opposite charge carriers travelling. If a charge carrier travelling through the bulk takes $t_{t1} \sim 6$ ns to reach the electrode on the opposite side ($d_1 \sim 500$ μm), the carrier with the opposite charge and a shorter path to the closer electrode – max. $d_2 \sim 10$ μm – only takes $t_{t2} \sim \frac{d_2}{d_1} t_{t1} = 120$ ps. A drift time this short induces a current pulse that is too narrow for the C2 amplifier or the oscilloscope to be able to observe.

Figure 3.5 shows a set of pulses and an averaged waveform for α , β and γ radiation using an ^{241}Am , ^{90}Sr and ^{60}Co source, respectively. The particles are measured with the non-irradiated sCVD diamond S37. α particles always produce the same signal pulse, but with a high noise RMS. The averaging suppresses the noise while retaining most the information. It does, however, smear the rising and falling edge, increasing the rising and falling time. The t_r is now of the order of 0.5 ns. Both β and γ pulses look similar - triangular and with a wide range of amplitudes. Here the pulse count is low, so the pulses with a high amplitude are not recorded. A trigger set very high would be needed to “catch” them with the oscilloscope.

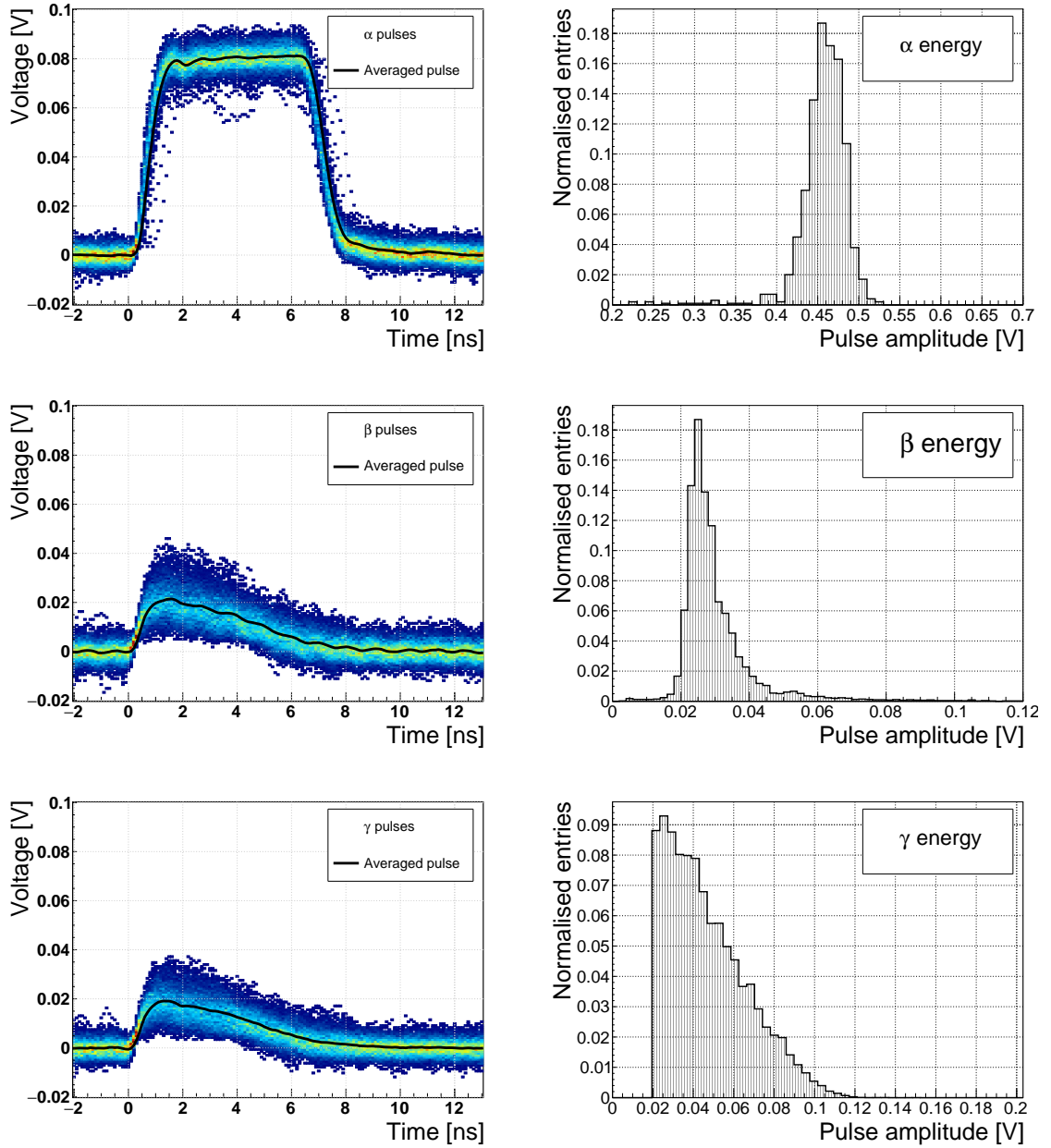


Figure 3.5: Superimposed and averaged pulses (left figures, current amplifier) and distributions of deposited energy (right figures, charge amplifier) for three types of radiation. Note the scale on the X axis of the distributions.

1201 3.3 Radiation limitations

1202 Exposure to ionising radiation degrades sensors. It deforms the lattice by displacing
1203 the atoms. Various types of lattice defects can be created in diamond, similar to those
1204 in silicon: vacancies, interstitials etc. [31] These deformations introduce new discrete
1205 energy levels between the valence and conduction band. Charge carriers drifting in
1206 their vicinity can get trapped, their energy falling to the energy level of the trap.
1207 Their emission back to the conduction band depends on how deep the trap is (how
1208 far away from the conduction band it is). The carriers caught in the shallow traps
1209 of the order of 100 meV below the conduction band are excited back up already by
1210 means of thermal excitation. This phenomenon has a short time constant, dependant
1211 on the environmental temperature. Those stopped by deep traps near the middle
1212 of the band gap need more energy and thus more time to be emitted to either the
1213 conduction or valence band. Some charge carriers remain trapped for long periods. If
1214 they build up in a certain region of the diamond and a space-charge forms, it affects
1215 the surrounding electric field. This is referred to as a space-charge formation. It can
1216 either help or counteract the field, depending on the polarity of the trapped carriers.

1217 The energy band jumping goes the other way, too. The carriers in the valence
1218 band may use the intermediate energy levels as “stepping stones” to jump to the
1219 conduction band and start drifting in the externally applied electric field. These
1220 intermediate energy levels are referred to as the generation centres of leakage current.

1221 The electrons and holes stopped in these traps cause a decrease of the induced
1222 current on the electrodes. This yields a lower integrated charge in an irradiated
1223 sensor than that in a non-irradiated one. The charge collection efficiency is therefore
1224 correlated with the level of irradiation.

1225 This section contains a study of the effects of pion ($\pi_{300 \text{ MeV}}$) irradiation on the
1226 charge collection efficiency of sCVD diamond detectors. To carry out this study, two
1227 diamond samples were irradiated to doses of $1 \times 10^{14} \pi \text{ cm}^{-2}$ (S79) and to $3.63 \times 10^{14} \pi \text{ cm}^{-2}$
1228 (S52). A test beam campaign was carried out to observe the charge collection effi-
1229 ciency at different bias voltage settings. The efficiency values acquired are used to
1230 determine the effective drop in efficiency as a function of the received radiation dose.
1231 This is to test if the collected charge Q is inversely proportional to the received dose
1232 Φ . A procedure defined by a collaboration researching diamond behaviour RD42 has
1233 been applied to the measured values to extract the damage factor. The next subsec-
1234 tion contains measurements and results of a long-term stability study using α and
1235 β particles. In particular, the charge collection efficiency with β and α radiation as
1236 a function of time is measured. To investigate this effect on the scale of charge car-
1237 riers, the change of TCT (transient current technique) pulses with time is observed.
1238 Finally, a procedure that improves the pulse shape and with it the charge collection
1239 is proposed.

3.3.1 Quantifying radiation damage in diamonds

Radiation damage varies with the type of radiation and its energy. There are several models existing [26, 25] that try to explain the impact of irradiation and to provide *hardness factors* to compare the radiation damage between different particles. The standard way is to convert the damage into *1 MeV neutron equivalent fluence* [13]. Some models have been extensively verified with simulations and with experiments. In these experiments the charge collection in sensors is measured before and after irradiation. This procedure is repeated several times, with a measurement point taken after every irradiation. Then the charge collection for this set of measurements is plotted as a function of the radiation dose received by a specific particle at a specific energy. From this a damage factor k_λ can be extracted. Damage factors have to be measured across a range of energies and types of radiation to properly quantify the damage in the sensors. Finally they are compared to the simulations to validate the theoretical models.

Diamond is an expensive material and the technology is relatively new as compared to silicon. Therefore few institutes are carrying out diamond irradiation studies. To join the efforts, the RD42 collaboration [10] has been formed. It gathers the experimental data from diamond irradiation studies. Unlike with silicon, the experimental results so far show no significant correlation with the NIEL (non-ionising energy loss) model [26], which correlates detector efficiency with the number of lattice displacements. Therefore an alternative model was proposed [25], correlating the diamond efficiency with the number of displacements per atom (DPA) in the bulk. The idea is that if the recoil energy of an incident particle is higher than the lattice binding energy (42 eV for diamond), the atom is displaced from its original position. The newly formed vacancy acts as a trap for drifting charge carriers. The more displacements that form in the bulk, the higher is the probability that a drifting carrier gets trapped. However, different types of particles interact differently with the bulk. In addition the mechanisms of interaction at low energies are different to those at high energies. To assess the damage for individual particles at a range of energies, simulations need to be run first. The simulation shown in [25] shows the DPA model for a range of energies of proton, pion and neutron irradiation in diamond. Figure 3.6 contains the simulation results as well as the superimposed empirical results of several irradiation studies. According to the figure, a 300 MeV pion beam damages the diamond bulk twice as much as a 24 GeV proton beam. The data points obtained by RD42 are also added to the figure. They have been normalised to damage by 24 GeV protons. Finally, the data point measured in the scope of this thesis has been added for comparison. The derivation is done below.

3.3.1.1 Irradiation with a $\pi_{300 \text{ MeV}}$ beam

The samples were irradiated at the Paul Scherrer Institute (PSI) [9] by means of a beam of pions with an energy of 300 MeV (kinetic energy 191.31 MeV) and with a flux of up to $1.5 \times 10^{14} \pi \text{ cm}^{-2}$ per day. The system has a 10 % uncertainty on the beam

3.3. RADIATION LIMITATIONS

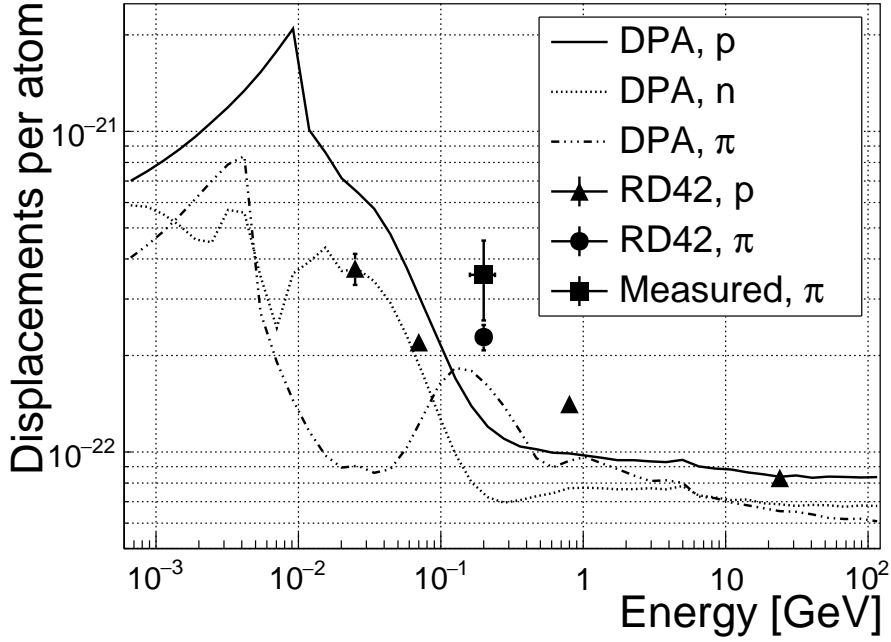


Figure 3.6: Diamond radiation damage - a model based on displacements per atom [25]. The figure shows the DPA as a function of the kinetic energy for protons, neutrons and pions. Added are data points for protons and pions by RD42 [35] and one data point for pions measured in the scope of this study.

1281 energy. Looking at the pion damage curve in figure 3.6, $\pi_{300 \text{ MeV}}$ point (191 MeV
 1282 kinetic energy) sits on a steep section of the DPA curve. This means that a deviation
 1283 in beam energy can have a significant effect on the damage in the sensor. In addition,
 1284 their quoted uncertainty on the measurement of the delivered dose is $\pm 20\%$.

1285 Two diamond samples, S52 and S79, were put in the $\pi_{300 \text{ MeV}}$ beam in the 2014
 1286 PSI irradiation campaign; S52 to $(1 \pm 0.21) \times 10^{14} \pi \text{ cm}^{-2}$ and S79 to $(3.63 \pm 0.77) \times$
 1287 $10^{14} \pi \text{ cm}^{-2}$. During the process, the gold electrodes got slightly activated, but the
 1288 activation decayed in two weeks.

1289 3.3.1.2 Charge collection efficiency and charge collection distance

1290 Three diamonds – non-irradiated S37 and irradiated S52 and S79 – were tested in a
 1291 $\pi_{120 \text{ GeV}}$ test beam in the SPS North Experimental Area at CERN [17] before and
 1292 after irradiation. The goal was to estimate the charge collection efficiency (CCE) and
 1293 charge collection distance (CCD) as a function of irradiation dose. The samples were
 1294 primed (pumped) prior to data taking using a ${}^{90}\text{Sr}$ radioactive source. The data were
 1295 then taken at a range of bias voltages ranging from 30 V to 900 V, yielding between
 1296 0.06 V/ μm and 1.8 V/ μm electrical field in the bulk. Every data point contained
 1297 approximately 5×10^4 measured particles. The charge deposited by the particles was
 1298 measured using a CIVIDEC Cx charge preamplifier.

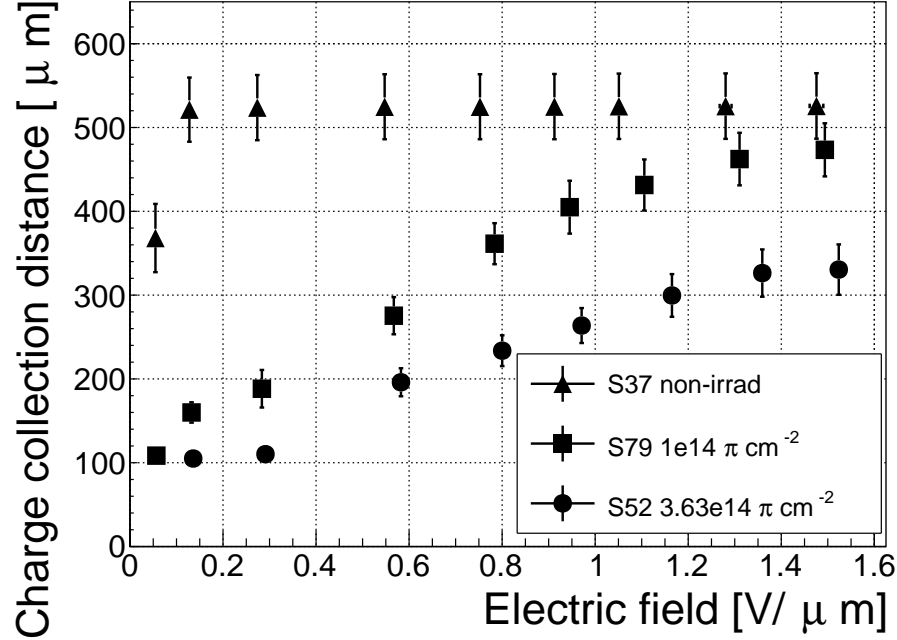


Figure 3.7: The figure shows the CCD for S37, S79 and S52 at a range of bias voltage settings.

As expected, the integrated amplitude spectrum is a Landau distribution. Its most probable value (MPV) is used to calculate the most probable collected charge Q_i :

$$Q_i [e^-] = \frac{1}{1.6 \times 10^{-19}} Q_i [C] = 6241 \cdot Q_i [fC] = 6241 \cdot \frac{MPV [mV]}{A [\frac{mV}{fC}]}, \quad (3.6)$$

where $A = 9.3 \text{ mV/fC}$ is the preamplifier gain factor and $1 e^- = 1.6 \times 10^{-19} \text{ C}$. The CCD can then be calculated using the average number of electron-hole pairs produced per micrometer in diamond $\delta_d = 36 \text{ e-h } \mu\text{m}^{-1}$ (from table 5.2):

$$CCD = \frac{Q_i}{\delta_d}. \quad (3.7)$$

The resulting CCD for the three measured samples at bias voltages ranging from $0.2\text{--}1.6 \text{ V } \mu\text{m}^{-1}$ is shown in figure 3.7. S37 exhibits a full collection distance already at $0.4 \text{ V } \mu\text{m}^{-1}$ whereas the irradiated samples have a more gentle increase of CCD with increasing bias voltage. It is evident that at $1 \text{ V } \mu\text{m}^{-1}$ the maximum CCD has not been reached in the case of S79 and S52. Nevertheless, to compare the measured data point with those provided by RD42, the CCD at $1 \mu\text{m}$ has to be taken.

3.3.1.3 Irradiation damage factor

The irradiation damage factor k_λ is a way to quantify irradiation damage of a specific particle at a specific energy. Via this factor different types of irradiation can be

3.3. RADIATION LIMITATIONS

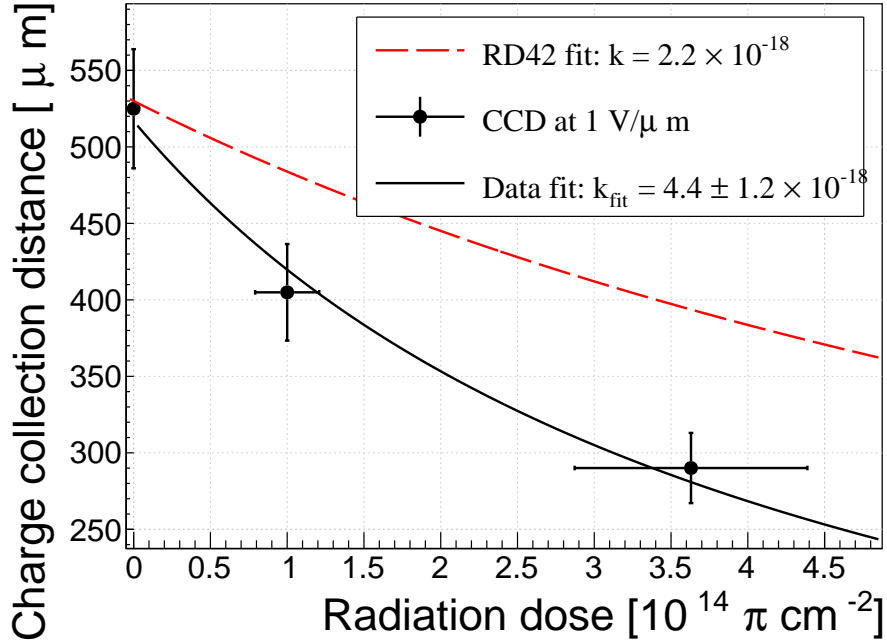


Figure 3.8: The charge collection distance at 1 V/ μm bias voltage for the three diamond samples is plotted as a function of the received radiation dose. It is compared to the RD42 data for pion irradiation. The data points are about 15–25 % lower than expected from the RD42 data [35].

¹³¹⁴ compared. It is obtained experimentally by measuring the CCD of a number of
¹³¹⁵ samples at various irradiation steps and fitting the equation 3.9 to the data. λ is the
¹³¹⁶ measured CCD, λ_0 is the CCD of a non-irradiated sample and Φ the radiation dose.
¹³¹⁷ As a reference, the damage factor for 24 GeV protons is set to $1 \times 10^{-18} \mu\text{m}^{-1} \text{ cm}^{-2}$.

$$\frac{1}{\lambda} = \frac{1}{\lambda_0} + k_\lambda \cdot \Phi \quad (3.8)$$

$$\lambda = \frac{\lambda_0}{k_\lambda \lambda_0 \Phi + 1} \quad (3.9)$$

¹³¹⁸ The data points with the maximum CCD obtained in the test beam measurements
¹³¹⁹ are plotted against radiation dose received in figure 3.8. Equation 3.9 is fitted to
¹³²⁰ the data points and a damage factor $k_\lambda = (4.4 \pm 1.2) \times 10^{-18} \mu\text{m}^{-1} \text{ cm}^{-2}$ can be
¹³²¹ obtained. The value is for a factor of two higher than the damage factor obtained by
¹³²² RD42. This could be due to an insufficient priming time ahead of the measurement.
¹³²³ In addition, the diamond samples have not been polished and re-metallised after
¹³²⁴ irradiation, as is the case for the RD42. Also, with only two samples measured, the
¹³²⁵ statistical uncertainty is high. Nevertheless, it can be concluded that the 300 MeV
¹³²⁶ pions damage the diamond bulk significantly more than the 24 GeV protons.

3.3.2 Long-term measurement stability

An important requirement for particle detectors is a stable performance over long periods of time. For instance, the charge collection for a defined radiation type and quantity must not change over time or has to change in a predicted way. The stability of diamond detectors depends on many factors: material purity, polishing process, electrode material, irradiation damage etc. The aim is to study the behaviour of diamond under controlled conditions, with the goal to understand its limitations. One of these limitations is the received radiation dose as it can affect the long-term stability of the sensor during operation.

The three diamond samples (S37, S79 and S52) have been exposed to two different types of ionising radiation for a longer period to see if their behaviour changes over time. Two parameters have been observed in particular:

1. Charge collection of β particles and
2. Charge collection and ionisation profile of α particles.

3.3.2.1 β long-term stability

The diamond samples have undergone a long-term stability test at room temperature using β radiation. This has been done using a ^{90}Sr source emitting ~ 2 MeV electrons at a rate of approximately $10^4 \text{ e}^- \text{ cm}^{-2}$. To simulate the initial conditions in HEP experiments, the sensors must not be primed before starting the measurements. The measurement setup consists of a diamond sample (S37, S52 or S79) with the CIVIDEC Cx spectroscopic amplifier, a silicon diode with a CIVIDEC C6 amplifier for triggering and a ^{90}Sr source on top. A particle emitted by the source traverses the sensor bulk and hits the silicon diode, triggering the analogue signal readout. The source is left on the top for the course of the experiment. The measurements, however, are taken at discrete times. For every data point, approximately 10^4 triggers have to be recorded. The offline analysis of the recorded signal pulse amplitudes yields a Landau distribution for every data point. The current charge collection relative to the initial charge collection for every sample is plotted as a function of the received β dose in figure 3.9. It shows that, for the irradiated samples, the charge collection efficiency improves when the diamond sensor is primed with a β source. The effect is negligible for the non-irradiated high-quality S37. Both relative increases are significant – 22 % for S79 and 55 % for S52. At a received dose of approximately 4×10^6 particles the charge collection is stabilised. At that point S79 achieves close to a full efficiency (in absolute values – not shown) whereas S52 reaches approximately 50 %.

The ~ 2.28 MeV electrons emitted by this source are not MIPs; their charge deposition is higher than that of an electron MIP, according to the Bethe-Bloch distribution [15]. Nevertheless, for the purpose of these measurements this energy is adequate since only the relative change in charge collection is of interest.

To sum up, diamond provides a stable measurement of the β radiation detection after reaching a stable state. Even if damaged by radiation, it reaches a stable charge

3.3. RADIATION LIMITATIONS

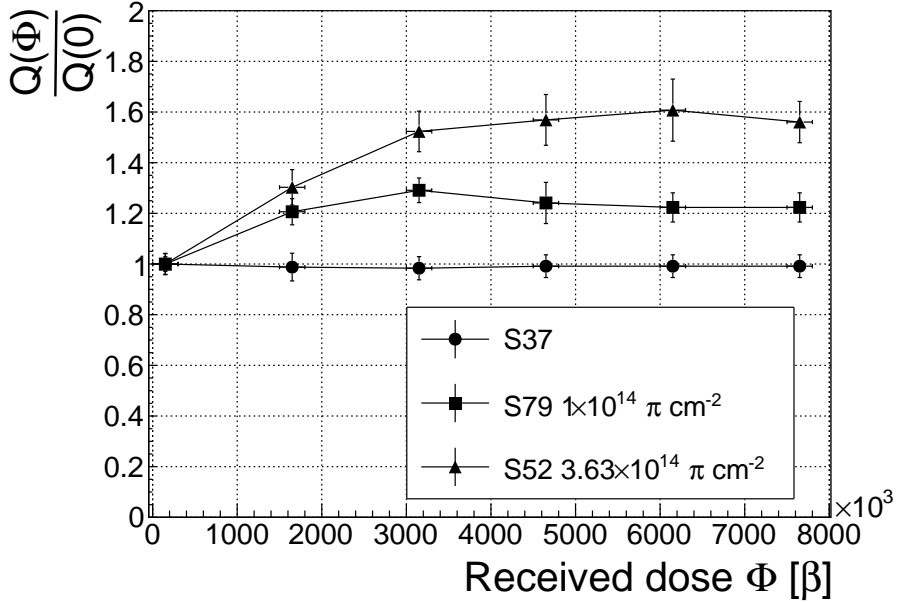


Figure 3.9: Relative increase of charge collection over time due to priming with the ^{90}Sr radioactive source. The charge collection for the non-irradiated S37 stays constant. The bias voltage for this measurement is 1 V/ μm .

1368 collection at a received dose of $\sim 4 \times 10^6$ MIPs. Its efficiency decreases with a high
 1369 irradiation dose. However, the decrease can be accounted for if the damage factor
 1370 and the rate and energy of the particles are known. γ radiation has a similar impact
 1371 on the diamond as the β . The incident photons, if they interact with the diamond,
 1372 prime the bulk, increasing the charge collection efficiency. The difference, however,
 1373 is that the interaction probability (cross-section) is lower for gammas [41, 24].

1374 3.3.2.2 α long-term stability

1375 This part discusses the stability of irradiated diamond sensors during α measurements.
 1376 An ^{241}Am source is used, emitting α particles with a mean energy of 5.5 MeV. They
 1377 affect the diamond differently than when subjected to β radiation. This is due to the
 1378 point-like charge carrier creation; an α particle penetrates the bulk and stops at a
 1379 depth of $\sim 14 \mu\text{m}$ (for a 5.5 MeV particle). The deposited energy on its path produces
 1380 4×10^5 e-h pairs according to equation 3.10:

$$n_{\text{e-h}} = \frac{E}{E_{\text{e-h}}} \quad (3.10)$$

1381 where E is the deposited energy of the particle and $E_{\text{e-h}}$ is the energy required to
 1382 create an electron-hole pair. The deposited energy and as a consequence the collected
 1383 charge for a MIP is significantly lower in comparison. According to equation 3.11 a
 1384 MIP produces 18×10^3 e-h pairs in a 500 μm thick diamond:

$$n_{\text{e-h}} = d \cdot E_{\text{avg}}, \quad (3.11)$$

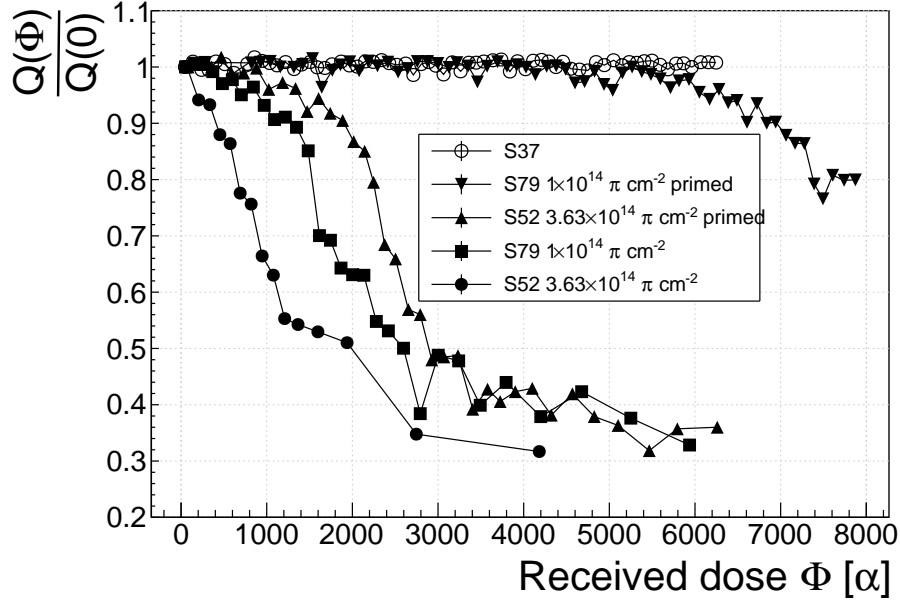


Figure 3.10: Relative decrease of the collected charge as a function of the received α dose for non-irradiated and irradiated diamond samples.

where d is the thickness of the sensor and E_{avg} is the average number of e-h pairs created per micrometer. Thus the collected charge of a 5.5 MeV α is for a factor of 22 higher. In addition, the energy is deposited in a small volume – 14 μm in depth and ~ 20 nm radially [28]. This dense distribution of charge carriers affects their behaviour at the start of the drift. Furthermore, carriers of only one polarity drift through the sensor while those of the opposite polarity almost instantly reach the adjacent electrode. Taking into consideration that the diamond bulk has been damaged by irradiation, these phenomena combined might have an effect on the operation of the detector.

The first test has been carried out using the CIVIDEC Cx spectroscopic amplifier, with the bias voltage of the samples set to +500 V. Figure 3.10 shows the results of 6500 recorded hits at a rate of ~ 7 particles per second. The collected charge $Q(\Phi)$ for the non-irradiated sample is stable as compared to the initial collected charge $Q(0)$ (plotted as a relative value $\frac{Q(\Phi)}{Q(0)}$). It is expected that the irradiated samples have a lower charge collection efficiency than the non-irradiated sample. However, their initial efficiency suddenly drops after a certain period of time. The initial efficiency after priming with β particles is higher than that without priming, but eventually it also deteriorates. In addition, the spread of measured energies increases significantly. This can not be seen in the figure as only the mean value of the data points is shown. Finally, the particle counting rate decreases with a decreased efficiency, which can be seen in the figure as the measurement points being further apart with the increasing dose (most pronounced for the un-primed S52).

To investigate this sudden drop in efficiency, the current pulse shapes using a C2

3.3. RADIATION LIMITATIONS

1408 current amplifier have to be observed, as shown in figure 3.11. The shape of the
1409 pulse holds more information about the charge carrier properties in the sensor than
1410 solely the value of the integrated charge. This time only the primed S79 sample
1411 has been tested. Both the hole and the electron collection are observed to determine
1412 whether they behave differently or not. The data in figures 3.11 show that the initially
1413 stable pulses start deteriorating – suddenly several different shapes start appearing,
1414 some still very similar to those from the beginning while the others with almost zero
1415 amplitude.

1416 Some charges get stopped in the charge traps in the bulk for a long time, building
1417 up regions of space-charge. The built up space-charge affects the electric field, making
1418 it non-uniform. The non-uniform field in turn affects the drifting carriers, slowing
1419 them down or speeding them up, depending on the field gradient. Since the movement
1420 of the carriers is inducing the electric current, the field gradient can be observed in
1421 the current signal.

1422 The second test with the C2 current amplifier has been carried out as follows: at
1423 the beginning of the test when the diamond is still operating stably, 60 pulses are
1424 recorded. An average pulse is calculated. This is a reference pulse for the subsequent
1425 measurement points. Then an RMS of the single pulses with respect to the reference
1426 pulse is calculated and the resulting RMS values are summed together (σ_{ref}).

1427 All the subsequent data points also consist of a set of 60 pulses. At every data point
1428 the summation of the RMS values of the individual pulses with respect to the initial
1429 averaged pulse is calculated (σ). The ratio between the initial σ_{ref} and discrete values
1430 σ gives a measure of change of the pulse shape with respect to the reference pulse at
1431 the start of the measurement. Figure 3.12 shows the ratio $\frac{\sigma_{\text{ref}}}{\sigma(\alpha \text{ dose})}$. From the data
1432 obtained it can be concluded that the initial pulse shape quickly starts deteriorating.
1433 In fact, the deterioration of the shape follows an approximate exponential decay
1434 function, which can be fitted to the data. The resulting decay constants for electrons
1435 and holes are $\tau_e = (4400 \pm 150) \alpha^{-1}$ and $\tau_h = (3300 \pm 140) \alpha^{-1}$. The electrons retain
1436 the initial shape for longer. The deteriorated shapes also seem to be for a factor of 2
1437 better than those of the holes.

1438 **Restoring the pulse shapes** Finally, an effort has been made to find a way for the
1439 pulse shapes to return to their initial state. Five methods are listed:

- 1440 1. Removing the source and leaving the bias voltage switched on,
- 1441 2. Removing the source and switching the bias voltage off,
- 1442 3. Priming with γ at a rate of $400 \text{ s}^{-1}\text{cm}^{-1}$ without applied bias voltage,
- 1443 4. Priming with β at a rate of $1000 \text{ s}^{-1}\text{cm}^{-1}$ with applied bias voltage and
- 1444 5. Priming with β at a rate of $1000 \text{ s}^{-1}\text{cm}^{-1}$ without applied bias voltage.

1445 The diamond sample S79 is first primed using a ^{90}Sr source for approximately one
1446 hour. Then the bias voltage is switched on and an ^{241}Am source is put on top. The
1447 pulses produced by the incident α particles have a proper rectangular pulse at the

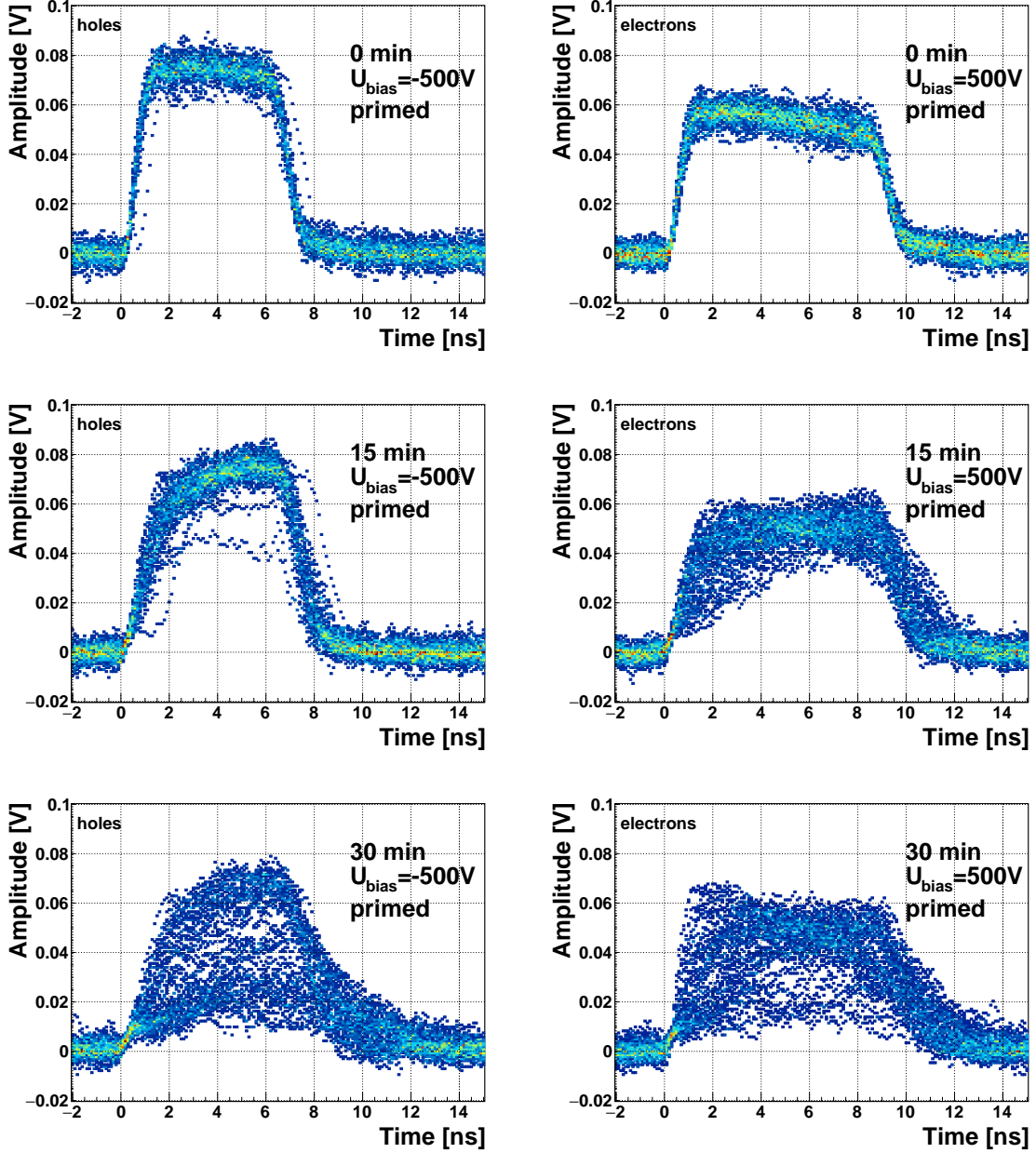


Figure 3.11: The signal of the irradiated and primed S79 deteriorates with time for both polarities. Every plot contains 60 superimposed pulses.

beginning, but then start changing – first gradually and later increasingly more in an erratic way, as described in the text above. After approximately 30 minutes, one of the methods is tested. When a “healing” procedure is started, a set of 60 pulses is taken at irregular points of time to observe the change in the pulse shape and to assess the quality of the “healing” procedure. Then the bias voltage is switched off and the sample is primed again to reset its state before starting with the next run.

The results depicted in figure 3.13 show that the methods (3) and (5) improve the

3.3. RADIATION LIMITATIONS

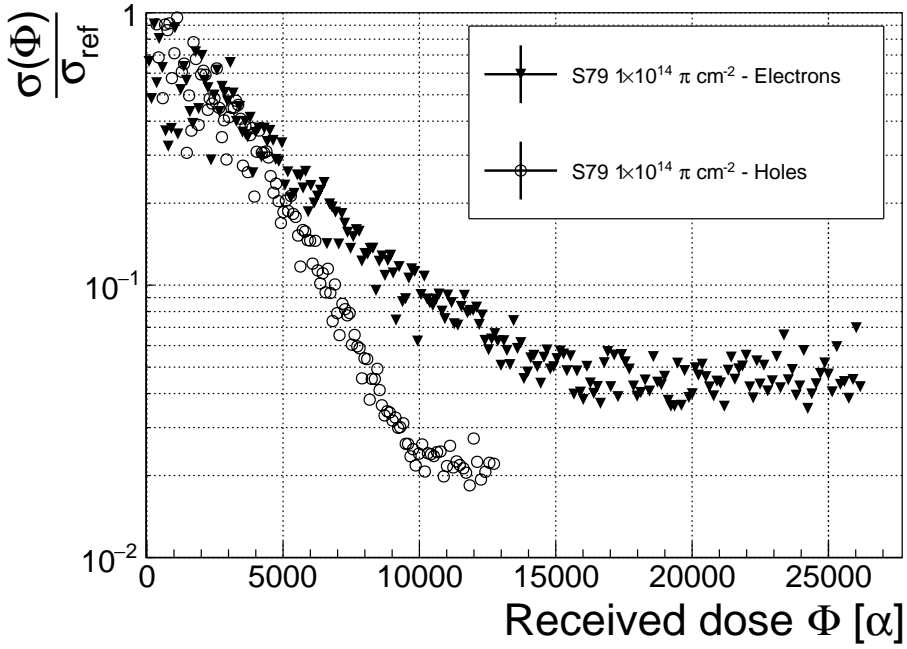


Figure 3.12: Deterioration of the pulse shapes with time.

shape, method (2) helps slowly, (1) does not show any change with time and (4) at first improves, but then significantly degrades the shape. The effect observed in method (4) has already been described in [32]. The “healing” process therefore depends on the rate of radiation, the bias voltage and the time of exposure. The ionising radiation creates free charges, which quickly recombine close to the place of generation. It is likely that they also release the charges trapped during the measurement, reducing the overall effect of the space-charge. The traps get filled with both flavours of carriers, thus they are neutralised. The pulse shape gradually returns to its initial state.

Procedure	Source	Bias voltage	Effectiveness
1	/	ON	no
2	/	/	slow
3	^{60}Co	/	YES
4	^{90}Sr	ON	no
5	^{90}Sr	/	YES

Table 3.2: Effectiveness of healing procedures.

In summary, the shape of the pulses caused by α radiation changes with time for irradiated samples. The shape of the pulses gets distorted and becomes erratic. Charge collection decreases and its spread increases. This happens even faster for non-primed diamonds. To “heal” the diamond – to bring the pulse shapes back to their initial shape – the sample must be primed using a β or a γ source for several minutes at a bias voltage of 0 V. Switching to the inverse polarity for a few seconds

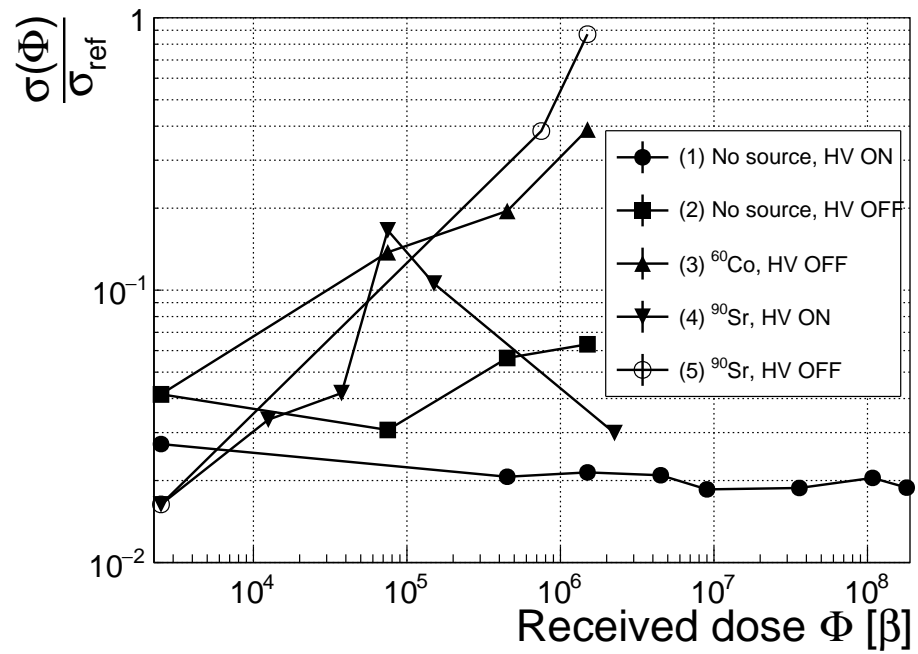


Figure 3.13: Comparison of the five procedures for the “healing” process for an irradiated diamond that had been exposed to α radiation with a rate of 10^1 s^{-1} , with the bias voltage switched on, for at least 30 minutes.

¹⁴⁷¹ helps a bit, but in a long run distorts the signal, which cannot return to its initial
¹⁴⁷² shape.

3.4. TEMPERATURE LIMITATIONS

1473 3.4 Temperature limitations

1474 A test has been carried out to evaluate the effect of temperature changes on the
1475 output signal of the diamond sensors. A cryostat filled with liquid helium is used to
1476 cool down the sensor during the measurement process. The current signal response
1477 to α -particles is measured at 18 temperature points between 4 K and 295 K. At every
1478 temperature point a set of 300 pulses is read out at various bias voltages. Resulting
1479 data show that the charge collection is stable from RT down to 150 K where it starts
1480 decreasing. It stabilises again at about one third of the initial value at 75 K. This
1481 behaviour was first measured and discussed by H. Jansen [28].

1482 The band gap energy in diamond is equal to $E_g = 5.5$ eV while the average energy
1483 to produce an electron-hole pair is $E_{e-h} = 13.25$ eV. This means there is excessive
1484 energy deposited in the diamond bulk. The incident α -particle stops within $\sim 10\text{--}15$ μm of the bulk,
1485 transferring all its energy to the lattice during deceleration. A part of this energy directly ionises the carbon atoms, creating free electron-hole pairs.
1486 The positively charged hole and the negatively charged electron in the hole attract
1487 each other via the Coulomb force and may undergo a bonding process during which
1488 an exciton is emitted.

1490 The remaining energy, however, is converted into lattice vibrations (phonons [46,
1491 28]). This means that the lattice within the ionisation volume (approximately $\sim 15 \mu\text{m} \times \sim 2 \text{ nm}$
1492 in size) is briefly heated up. The hot plasma then cools down to the temperature of
1493 the surrounding material by heat dissipation, (i.e. phonon transport).

1494 The free electron binds with the free hole into a bound state (not recombination)
1495 – the exciton [33]. The exciton binding energy is 80 meV. At higher temperatures the
1496 lattice provides enough energy to thermally excite the electron from the exciton state
1497 back to the conduction band. At lower temperatures, however, the exciton lifetime
1498 increases, which means that it takes a longer time for the electrons to get re-excited
1499 to the conduction band. The re-excitation lifetime at room temperature is ~ 30 ps,
1500 increasing to $\sim 150 \mu\text{s}$ at 50 K [28]. This means that some of the bound electrons do
1501 not even start drifting within the period of ~ 10 ns, which is the expected carrier drift
1502 time. When they are finally freed, the current they induce is already hidden in the
1503 electronics noise. The effective area of the observed current pulse is therefore smaller
1504 than that of a pulse induced by all the carriers drifting at the same time. This in
1505 effect reduces the measured collected charge. The longer the time constant, the lower
1506 the measured collected charge, as shown in figures 3.18 and 3.19.

1507 3.4.1 Temperature-variant α -TCT before irradiation

1508 Three sCVD diamond samples have been tested at a range of temperatures using
1509 the α -TCT technique. At each temperature point, the bias voltage is set to several
1510 positive and negative values. A set of 300 pulses is recorded at every data point
1511 and averaged offline. The resulting averaged pulses of sample S37 at the 260 K
1512 temperature point and a bias voltage of ± 400 V, ± 500 V and ± 700 V are shown in
1513 figure 3.14. The pulses induced by holes as charge carriers are shorter than those

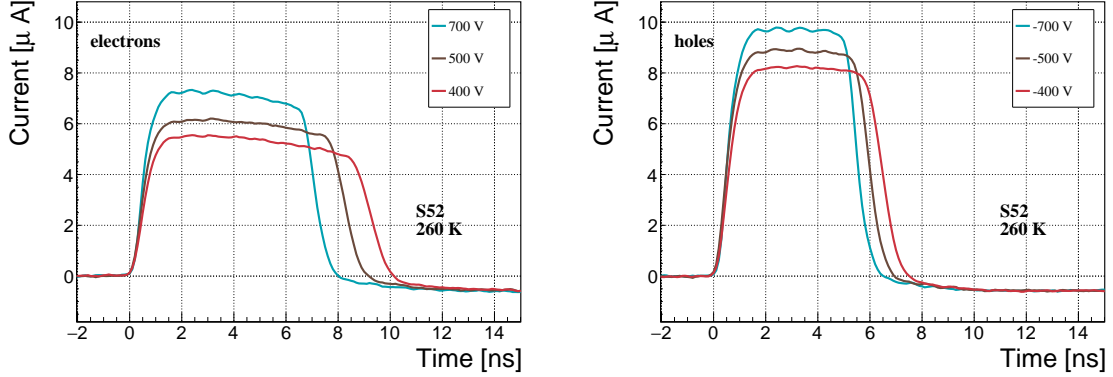


Figure 3.14: Varied bias voltage at a fixed temperature.

induced by electrons, which means that holes travel faster in diamond. The area of the pulse, however, is the same for both polarities, which corresponds to the fact that the same amount of charges is drifting in both cases.

Figure 3.15 shows pulses at a bias voltage set to ± 500 V across the range of temperatures between 4 K and 295 K. Several conclusions can be drawn by observing their shape. First, the pulse shapes change with decreasing temperature. The pulse time gets shorter, hinting at the faster carrier drift velocity v_{drift} . Second, between 150 K and 75 K there is a significant change in shape - the time constant of the rising edge increases significantly and the pulse area decreases. From 75 K down to 4 K there is no significant change. Last, the top of the pulse at the S52 is not flat, which means that a portion of the drifting charge is lost along the way. This is due to charge trapping, likely by means of crystal defects or impurities.

3.4.2 Temperature-variant α -TCT after irradiation

The irradiated S79 and S52 have been re-tested in the cryostat after irradiation. The aim is to observe how their pulse shapes change with decreasing temperature, in particular the decaying top of the pulses, as shown in figure 3.16. The decay time gives information on trapping of charge carriers while travelling through the diamond bulk. A variation of the decay time constant as a function of temperature might help to reveal the type and depth of the charge traps. To observe these effects or lack thereof, a number of requirements have to be met. First, the diamond samples are intentionally not primed prior to the experiment because priming would improve the pulse shapes and possibly change the decay time constant of the signal. Second, keeping in mind that the pulse shape of irradiated diamonds changes with time, the duration of the measurement of an individual data point has to be short – of the order of 30 seconds. Last, the sequence of the bias voltage settings is important, the reason for which is explained below.

Unfortunately it is not possible to avoid temporal pulse changes. For instance, one measurement point takes approximately one minute. After the measurement, the

3.4. TEMPERATURE LIMITATIONS

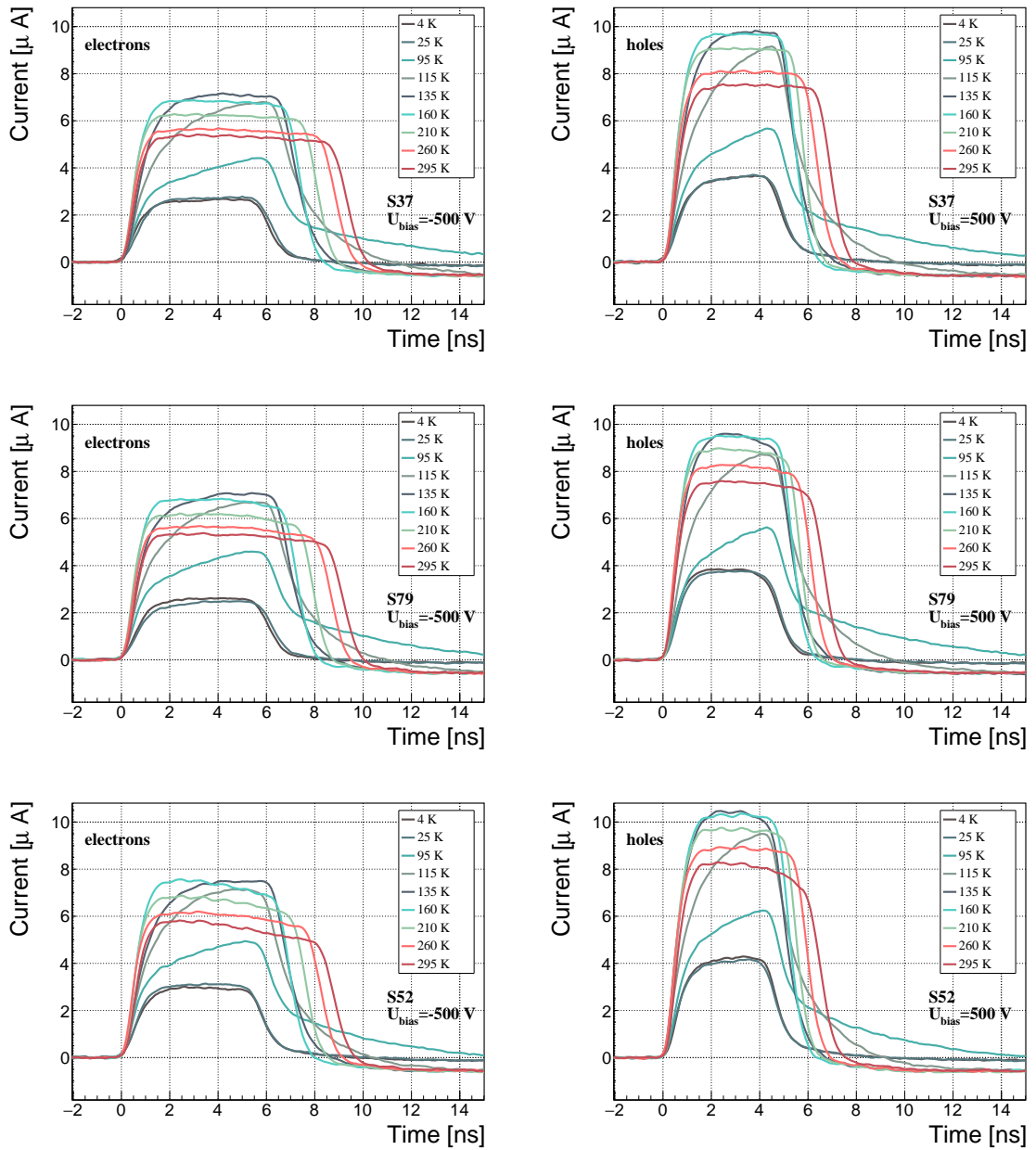


Figure 3.15: Several data points between 4 K and 295 K at a bias voltage of ± 500 V.

bias voltage polarity is swapped for a few seconds to bring the diamond back into its initial state. But a few seconds with respect to a minute are not enough. Therefore when the bias voltage is set to the next value, there is still some residual effect of the previous measurement. Similar to the effects of polarisation, this effect is also decreasing the pulse height. This can be observed in figure 3.16, which shows the resulting pulses of S52 for bias voltages of ± 200 V, ± 300 V, ± 400 V and ± 500 V at 230 K and 260 K. In this case the measurement sequence is: 230K (200 V, 300 V, 400 V, 500 V, -500 V, -400 V, -300 V), 260 K (-200 V, -300 V, -400 V, -500 V, 500 V, 400 V, 300 V). The changes in pulse shapes for holes at 230 K and 260 K cannot be attributed to the temperature change. Instead, the explanation could lie in diamond “polarisation”. This means that, when exposed to an electric field with α measurements ongoing, an internal electric field of inverse polarity builds up in the diamond, which effectively reduces the overall electric field. This internal field does not dissipate when the external bias voltage is switched off. The diamond becomes “polarised”. When switching the polarity of the external bias voltage, the internal and external electric field point in the same direction at the beginning, increasing the overall electric field and with it the pulse height. In figure 3.16 this happens when switching from 500 V (figure 3.16a) to -500 V (figure ??) at 230 K. The built up polarisation contributes to the pulse having a sharp rising edge and a high amplitude. This effect decays during the next two voltage points. There would be a handful of ways to avoid this polarisation effect in the data:

1. After every data point invert the bias voltage and leave it to return to a neutral state for the same amount of time,
2. Make a hysteresis of data points, going from minimum negative to maximum positive bias several times,
3. Reduce the measurement time at every bias voltage setting.

Unfortunately, options (1) and (2) are very time consuming and would increase the overall experiment time to over one day. The third option would worsen the resulting averaged pulses. In the end an alternative option has been chosen: alternating the starting bias voltage and the sequence at every temperature point. With this option, a meaningful systematic error in analysing the pulse shapes can be attained.

Figure 3.17 shows the irradiated S52 and S79 as well as the non-irradiated S37 for comparison, all at a bias voltage of ± 500 V and at several temperature points between 4 K and RT. It is evident that the radiation damage affects the shape of the pulses across all temperatures.

3.4.2.1 Collected charge as a function of temperature

The area below the current pulse is proportional to the charge collected by the diamond detector. The collected charge is observed as a function of temperature. First, the amplitude values of the averaged pulses at a bias voltage of ± 500 V and across the

3.4. TEMPERATURE LIMITATIONS

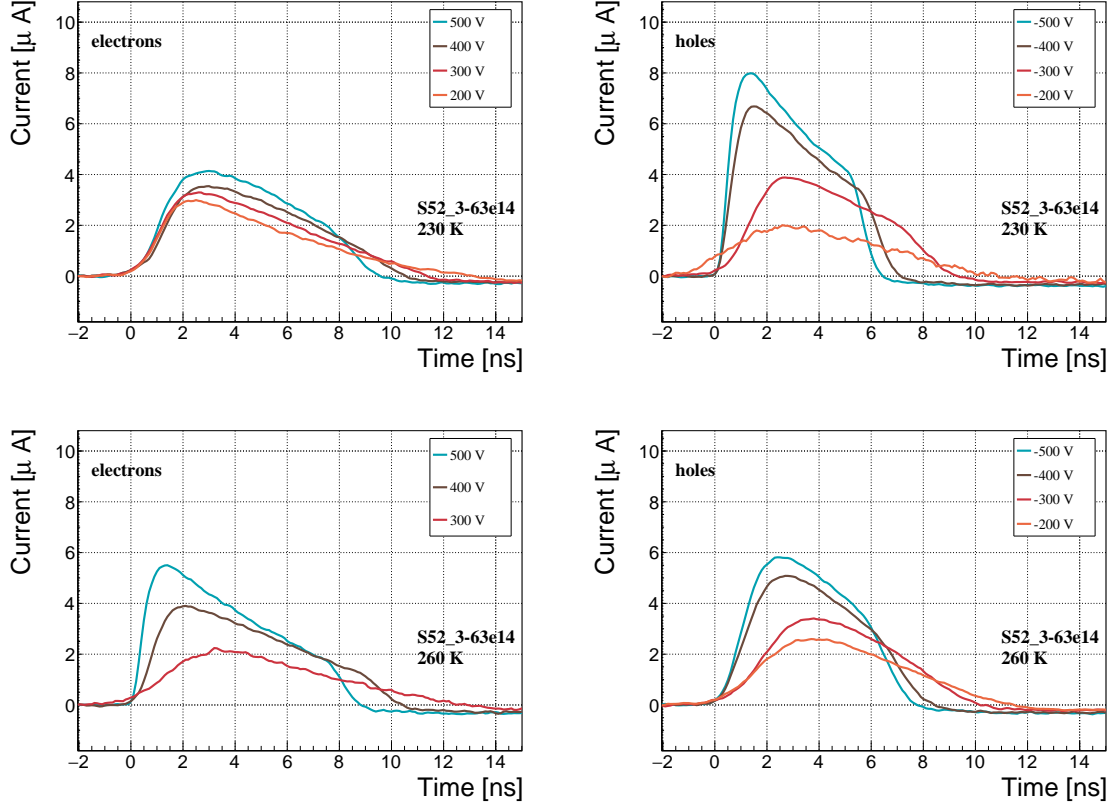


Figure 3.16: Varied bias voltage at a fixed temperature for an irradiated sample.

temperature range between 4 K and 295 K have to be integrated. Then a calibration factor is used to derive the charge for all data points. This factor is obtained using a Cx charge-sensitive amplifier. The resulting values for electrons and holes are plotted in figures 3.18 and 3.19, respectively. Thesis [28] proposes a model that explains the drop in charge below 150 K. The new contribution are the data points for the irradiated samples. The values for them are lower than those of non-irradiated samples, which is expected. The values for all samples are fairly stable in the range between 4 K and 75 K and between 150 K and 295 K. However, in the values for the irradiated S52 some excursions can be observed. This is due to the sequence of the measurement steps, which introduces a hysteresis effect and is explained in the preceding text.

The collected charge drops significantly from 150 K down to 75 K. In the non-irradiated samples the values in the lower temperature range are approximately 30 % of the values at the high range. For the irradiated ones this difference is lower – 35 % for S79 and 50 % for S52. An interesting detail is that the ratio between the values for non-irradiated samples and their irradiated counterparts at the lower range is different than at the higher range. Looking at the values for the electron collection in figure 3.18: for S52 the lower ratio is equal to 128 % and the higher equal to 170 %. For S79 these ratios are 100 % and 109 %, which means that the difference in charge

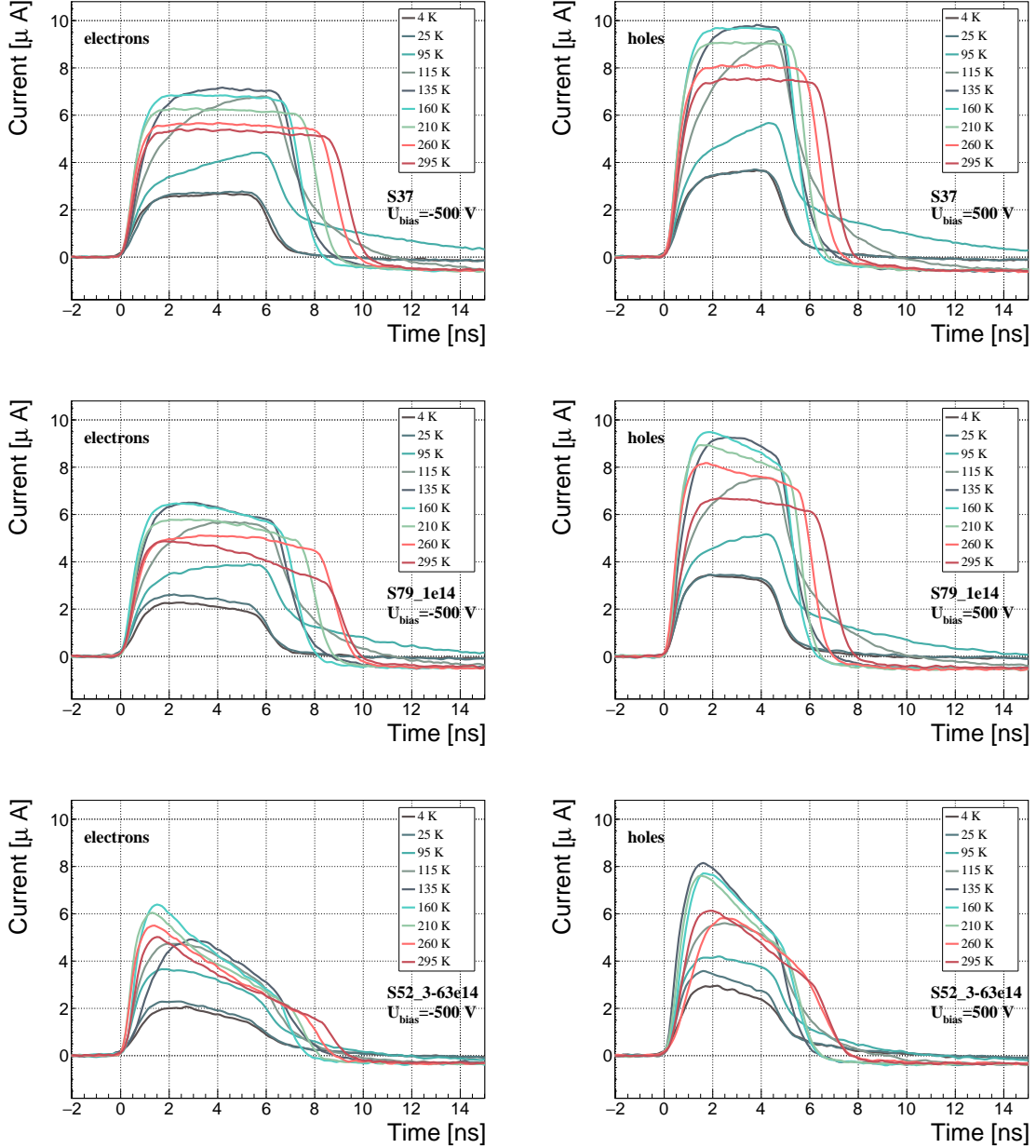


Figure 3.17: After irradiation: several data points between 4 K and 295 K at a bias voltage of ± 500 V.

1600 collection between 4 K and 75 K before and after irradiation is negligible.

1601 3.4.2.2 Charge trapping

1602 The carriers drifting through the bulk get stopped by the charge traps with a certain
 1603 probability. This trapping happens uniformly throughout the diamond, decreasing
 1604 the number of carriers in the charge cloud. Therefore the absolute number of trapped

3.4. TEMPERATURE LIMITATIONS

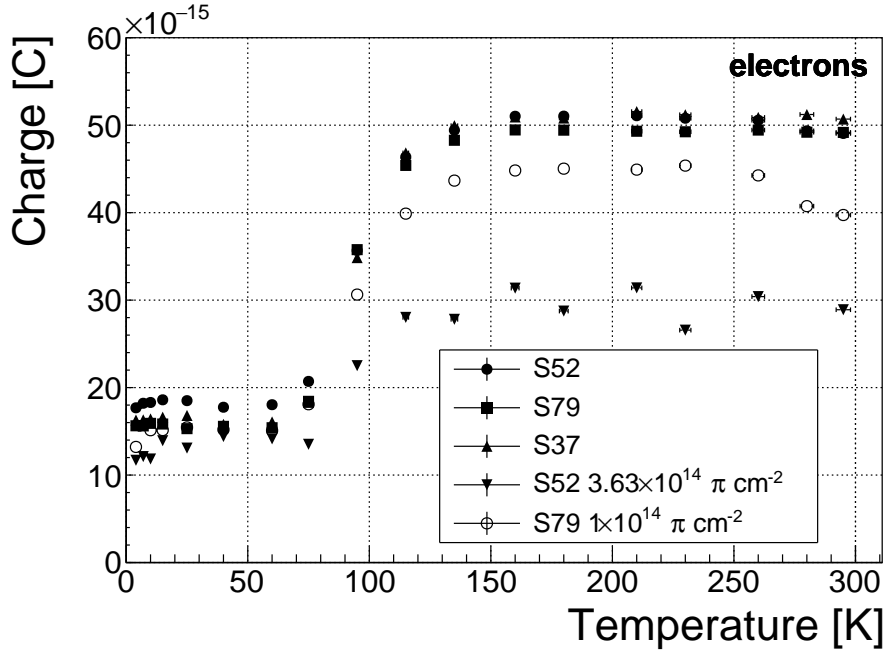


Figure 3.18: Collected charge for electrons as a function of temperature.

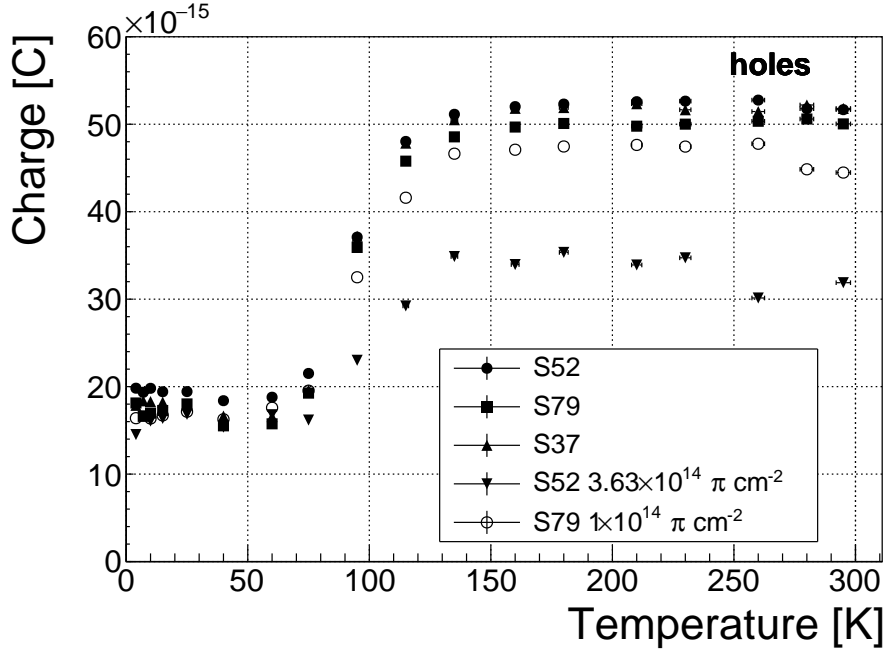


Figure 3.19: Collected charge for holes as a function of temperature.

carriers decreases. At the same time the absolute number of trapped carriers per unit of length decreases. The resulting function for the number of drifting carriers per unit of length is a decaying exponential function:

$$I(t) = I(0) \cdot e^{-\frac{t-t_0}{\tau}} + I_0, \quad (3.12)$$

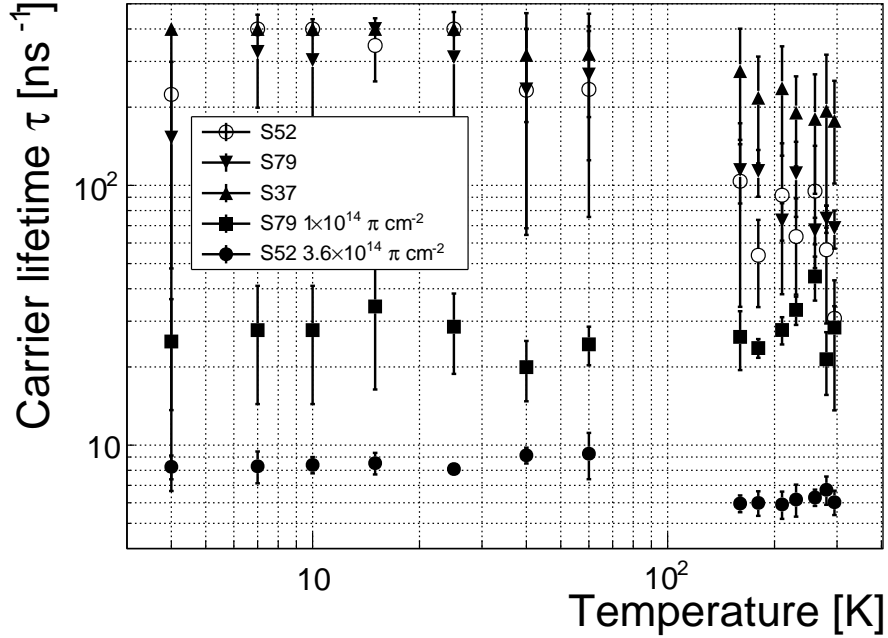


Figure 3.20: This figure shows the charge carrier lifetime as a function of temperature. The data points between 75 K and 150 K are omitted. The fit function only works well on signals with a well pronounced decaying top.

where $I(0)$ is the initial induced current, I_0 is the end current, t is time, t_0 is temporal displacement of the pulse and τ is the decay time constant. This value tells how long it takes before the amplitude of the pulse decreases to 63 % of its initial height.

The decaying exponential function is fitted to the decaying top of the averaged pulses at bias voltages of ± 400 V and ± 500 V across all temperatures excluding the transitional range between 75 K and 150 K. The resulting decay time constants τ for an individual temperature point are not equal, which stems from the fact that the pulses change with time due to “polarisation”. This counts as a systematic error. Therefore the fitted τ for ± 400 V and ± 500 V are averaged into one value representing the measurement at that temperature point. Figure 3.20 shows the fitted τ for the five samples between 4 K and 295 K. In principle the time constants should be infinite for a perfect and non-irradiated sample. Here a slightly tilted top of the pulse due to space-charge is already successfully fitted with an exponential function (a pitfall in an automatic analysis), resulting in a τ of the order of $(200 \pm 20) \times 10^{-9}$ s. Consequently the fitting method is not adequate for non-irradiated samples. For the irradiated samples the fit becomes increasingly more meaningful. As seen in figure 3.20, the fitted values of the irradiated samples are fairly stable across all temperatures. There is a slight increase in the decay time constant of the S52 from $(6.0 \pm 0.5) \times 10^{-9}$ s above 150 K to $(8.5 \pm 0.9) \times 10^{-9}$ s below 75 K. On the other hand, this step is not observable in the S79 data. With only one sample exhibiting this behaviour, the effect is not significant enough. Judging by the data acquired, the samples would need to

3.4. TEMPERATURE LIMITATIONS

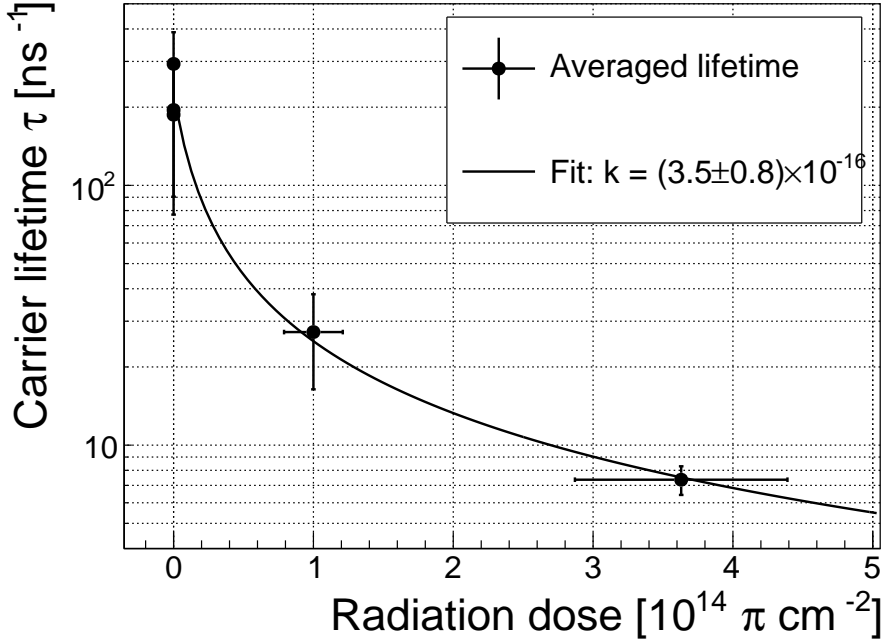


Figure 3.21: This figure shows the carrier lifetime averaged over all temperatures and plotted as a function of the π irradiation dose.

be irradiated to doses above $1 \times 10^{14} \pi \text{ cm}^{-2}$ to quantify this effect in detail. So far this effect is not regarded as significant for the scope of this thesis. Building on this assumption, the conclusion is that the signal decay time constant for irradiated sCVD diamond is constant across the temperature range between 4 K and 295 K, excluding the transitional range between 75 K and 150 K.

Taking into account the discussion above, all the values can be averaged into one decay constant. Figure 3.21 shows these values for all samples as a function of the received $\pi_{300 \text{ MeV}}$ radiation dose. To estimate the charge carrier lifetime with respect to the radiation dose received, a similar model is used than that in section 3.5. This model states that the charge carrier lifetime is linearly decreasing with increasing radiation dose:

$$\frac{1}{\tau} = \frac{1}{\tau_0} + \kappa_\tau \cdot \Phi \quad (3.13)$$

$$\tau = \frac{\tau_0}{\kappa_\tau \tau_0 \Phi + 1} \quad (3.14)$$

where τ_0 is the lifetime for a non-irradiated sample (real lifetime, therefore of the order of 400 ns), τ is the lifetime of an irradiated sample, Φ is the received radiation dose and κ_τ the lifetime degradation factor. For these data the fitted factor is equal to $\kappa_\tau = (3.5 \pm 0.8) \times 10^{-16} \text{ s cm}^2 \pi_{300 \text{ MeV}}^{-1}$. Using this factor, the steepness of the decay in the pulse shape as a function radiation dose can be estimated. This is highly useful information when designing a system where the current pulse shape is an important factor.

1648 3.5 Conclusion

1649 This chapter gives an overview of the capabilities and limitations of diamond as a
1650 particle detector. Two effects on diamond are studied – radiation and temperature.

1651 Two sCVD diamond detectors were irradiated with 300 MeV pions. They were
1652 tested alongside a non-irradiated sample to observe the changes in the ability to detect
1653 α , β and γ radiation. Their charge collection efficiency was measured in a test beam
1654 facility. The results were compared to the results from the RD42 collaboration and
1655 a DPA model. A radiation damage factor $k_\lambda = (4.4 \pm 1.2) \times 10^{-18} \mu\text{m}^{-1} \text{cm}^{-2}$ was
1656 obtained for $\pi_{300 \text{ MeV}}$ particles. The data point was not in agreement with the data
1657 provided by RD42 nor with the model. However, the irradiation process and the low
1658 number of tested samples hold a relatively high statistical uncertainty. In addition,
1659 there was no diamond surface treatment done in between the measurements, as is
1660 the case in the study conducted by RD42. The results obtained in the course of
1661 these measurements are going to be fed into the existing pool of data in the RD42
1662 collaboration.

1663 The next step was to test the long-term capabilities for α detection. The shape
1664 of the ionisation profile was investigated to determine the behaviour of the charge
1665 carriers in the irradiated diamond. An exponential decay was observed in the pulses
1666 of irradiated samples, proving that there are charge traps in the bulk that were created
1667 during irradiation. Then a long-term stability test was carried out. The results show
1668 that the irradiated diamond detectors do not provide a stable and reliable long-term
1669 measurement of α particles. This might be due to a space-charge build-up in the
1670 bulk, which changes the electric field, affecting the charge carriers. A procedure to
1671 improve the pulse shape using β and γ radiation was proposed.

1672 Finally, the diamond sensors were cooled down to temperatures between 4 K and
1673 295 K. Their response to α particles was observed. The results of the non-irradiated
1674 and irradiated samples were compared. The effect of reduction for the number of
1675 drifting charges due to exciton recombination was observed in both sets of data.
1676 The second set had a superimposed effect of charge trapping during the drift, which
1677 was represented by an exponential decay in the signal. The decay time constant
1678 did not change with temperature. Therefore all temperature points for individual
1679 samples were averaged and the decay time constants were plotted against the received
1680 radiation dose. A lifetime degradation factor $\kappa_\tau = (3.5 \pm 0.8) \times 10^{-16} \text{ s cm}^2 \pi_{300 \text{ MeV}}^{-1}$
1681 for non-primed diamonds was defined.

₁₆₈₂ **Chapter 4**

₁₆₈₃ **Charge monitoring**

₁₆₈₄ *The ATLAS Diamond Beam Monitor*

₁₆₈₅ Particle detectors in high energy physics experiments need to meet very stringent
₁₆₈₆ specifications, depending on the functionality and their position in the experiment.
₁₆₈₇ In particular, the detectors close to the collision point are subject to high levels of
₁₆₈₈ radiation. Then, they need to operate with a high spatial and temporal segmentation
₁₆₈₉ to be able to precisely measure trajectories of hundreds of particles in very short
₁₆₉₀ time. In addition, they need to be highly efficient. In terms of the structure, their
₁₆₉₁ active sensing material has to be thin so as not to cause the particles to scatter
₁₆₉₂ or get stopped, which would worsen the measurements. This also means that they
₁₆₉₃ have to have a low heat dissipation so that the cooling system dimensions can be
₁₆₉₄ minimised. Finally, they need to be able to operate stably for several years without
₁₆₉₅ an intervention, because they are buried deep under tonnes of material and electronics.

₁₆₉₆ The material of choice for the inner detector layers in the HEP experiments is
₁₆₉₇ silicon. It can withstand relatively high doses of radiation, it is highly efficient (of the
₁₆₉₈ order of $\sim 99.9\%$) and relatively low cost due to using existing industrial processes
₁₆₉₉ for its production. Its downside is that, with increasing irradiation levels, it needs to
₁₇₀₀ be cooled to increasingly low temperatures to ensure a stable operation. This is not
₁₇₀₁ the case with diamond. In addition, diamond has a lower radiation damage factor,
₁₇₀₂ which means it can operate in a radiation-heavy environment for a longer period.

₁₇₀₃ The ATLAS Diamond Beam Monitor (DBM) [] is a novel high energy charged
₁₇₀₄ particle detector. Its function is to measure luminosity and beam background in the
₁₇₀₅ ATLAS experiment. Given its position in a region with a high radiation dose, di-
₁₇₀₆ amond was chosen as the sensing material. The monitor's pCVD diamond sensors
₁₇₀₇ are instrumented with pixellated FE-I4 front-end chips. The pCVD diamond sensor
₁₇₀₈ material was chosen to ensure the durability of the sensors in a radiation-hard envi-
₁₇₀₉ ronment and the size of its active area. The DBM is not the first diamond detector
₁₇₁₀ used in HEP, but it is the largest pixellated detector installed thus far, as shown in
₁₇₁₁ figure 4.1. It was designed as an upgrade to the existing luminosity monitor called the
₁₇₁₂ Beam Conditions Monitor (BCM) [] consisting of eight diamond pad detectors, which

4.1. LUMINOSITY MEASUREMENTS

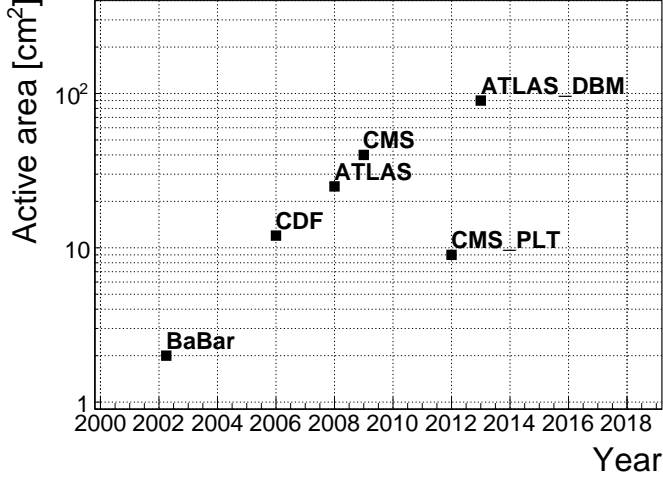


Figure 4.1: Diamond detectors installed in high-energy physics experiments in the last decade, sorted by the active sensor area. The first four detectors from the left are radiation monitors whereas the right two are pixel trackers.

is able to perform precise time-of-flight (ToF) measurements. The DBM complements the BCM's features by implementing tracking capability. Its pixelated front-end electronics significantly increase the spatial resolution of the system. Furthermore, the DBM is able to distinguish particle tracks originating in the collision region from the background hits. This capability is a result of its projective geometry pointing towards the interaction region. This chapter first describes the principles of luminosity measurements. It then explains how the DBM carries out this task. Finally, some results from tests and from the real collisions are presented.

When a particle traverses a sensor plane, a hit is recorded in the corresponding pixel. Thus, a precise spatial and timing information of the hit is extracted. With three or more sensors stacked one behind the other, it is also possible to define the particle's trajectory. This is the case with the DBM. Its projective geometry allows the particles to be tracked if they traverse the sensor planes. The DBM relates the luminosity to the number of particle tracks that originate from the collision region of the ATLAS experiment. Particles that hit the DBM from other directions are rejected as background radiation.

4.1 Luminosity measurements

Luminosity is one of the most important parameters of a particle collider. It is a measurement of the rate of particle collisions that are produced by two particle beams. It can be described as a function of beam parameters, such as: the number of colliding bunch pairs, the revolution frequency, the number of particles in each bunch and the transverse bunch dimensions. The first four parameters are well defined. However, the transverse bunch dimensions have to be determined experimentally

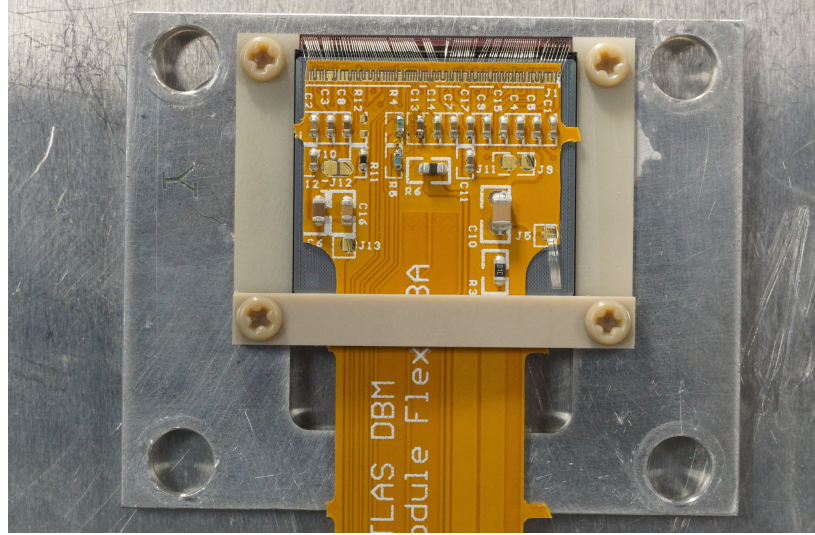


Figure 4.2: DBM module, top-down view. Visible is the flexible PCB with signal and power connections, the silicon sensor and a part of the FE-I4. Wire bonds from the PCB to the FE-I4 and to the sensor are also visible.

1736 during calibration. The ATLAS experiment uses the *van der Meer scan* [1] during
1737 low-luminosity runs to calibrate the luminosity detectors. This scan is performed
1738 by displacing one beam in a given direction and measuring the rate of interactions
1739 as a function of the displacement. Transverse charge density of the bunches can be
1740 estimated on the basis of the interaction rate. The calibrated luminosity detectors
1741 can then operate during high-luminosity runs.

1742 One approach to luminosity monitoring is to count the number of particles pro-
1743 duced by the collisions. The luminosity is then proportional to the number of detected
1744 particles. A detector has to be capable of distinguishing individual particles that fly
1745 from the interaction point through the active sensor area. If the detector has at least
1746 three layers, it can reconstruct the particles' tracks, which in turn yields more infor-
1747 mation on their trajectory. This is one reason why detectors with a high timing-
1748 and spatial segmentation are more suitable for these applications. The second reason
1749 is that, with a high spatial segmentation, the detector does not saturate even at high
1750 particle fluencies.

1751 4.2 Diamond pixel module

1752 The two most important parts of the diamond pixel module, which is shown in fig-
1753 ure 4.2, are the sensor, which detects ionising radiation, and the pixellated front-end
1754 chip, which collects the ionised charge with a high spatial segmentation, processes the
1755 recorded data and sends them to the readout system. This section describes these
1756 two main parts of the module and their interconnection.

4.2. DIAMOND PIXEL MODULE



Figure 4.3: A pCVD wafer. The golden dots on the surface are the electrodes that are applied during the qualification test. The wafer is measured across the surface to find the regions with the highest efficiency.

1757 4.2.1 Sensors

1758 The DBM modules are instrumented with two types of sensors – pCVD diamond and
1759 silicon. The silicon sensors are used as a fallback solution because there were simply
1760 not enough high-quality diamond sensors available. In addition, a comparative study
1761 of irradiation damage between silicon and diamond can be made with such a hybrid
1762 system.

1763 **Diamond sensors** The target material for this application is pVCD diamond. The
1764 reason for this is that the active area of an individual sensor must be approximately
1765 4 cm^2 , which is too large for the sCVD diamond. pCVD material is also a bit
1766 cheaper, which makes a detector with a large active area more feasible to build. The
1767 material is provided by three companies: DDL, E6 and II-IV and it is grown in
1768 15 cm wafers, as seen in figure 4.3. The target thickness of the wafers is 500 μm and
1769 the minimum required charge collection efficiency is 40 % ($\text{CCD} \geq 200 \mu\text{m}$). They
1770 need to be operated at bias voltages between 600–1000 V. On one side there is a
1771 single gold electrode applied across the entire surface. On the other side a pixellated
1772 metallisation is added.

1773 **Silicon sensors** are standard $n^+ - in - n$ planar sensors with a 200 μm thickness
1774 and were mostly fabricated at CiS [], a company from Ertfurt, Germany. They are
1775 designed to have nearly a 100 % efficiency when non-irradiated. Their bulk resistivity
1776 is between 2–5 $\text{k}\Omega\text{cm}$ and they were diffusion oxygenated at 1150 °C for 24 hours to

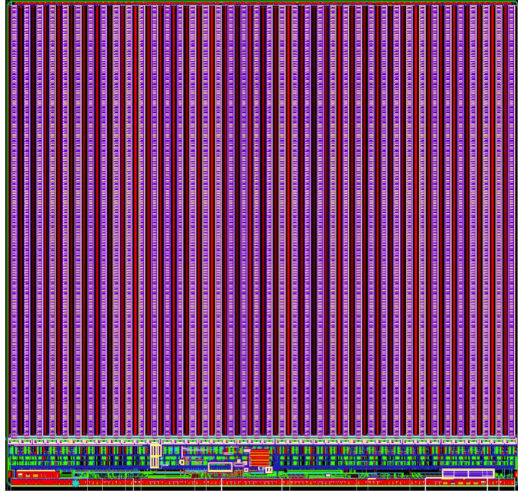


Figure 4.4: FE-I4 layout, top-down view. The pink area are pixels grouped into columns, the green area below is the common logic and the red strip at the bottom are the wire bond pads.

increase their radiation hardness. One side is segmented into pixels. Guard rings at the edges of the sensor provide a controlled drop in potential, reducing the possibility of shorts at maximum design bias voltages of the order of 1000 V.

4.2.2 Front-end electronics

The FE-I4 (front-end version four) [1] is an ASIC pixel chip designed specifically for the ATLAS pixel detector upgrade. It is built as a successor to the current pixel chip FE-I3, surpassing it in size of the active area ($4\times$ larger) as well as the number of channels/pixels ($10\times$ more). 336 such FE-I4 modules are used in the newly installed pixel layer called the Insertable B-Layer (IBL) [2]. The DBM is also instrumented with these chips. The FE-I4's integrated circuit contains readout circuitry for 26880 pixels arranged in 80 columns on a $250\text{ }\mu\text{m}$ pitch and 336 rows on a $50\text{ }\mu\text{m}$ pitch. The size of the active area is therefore $20.0\times16.8\text{ mm}^2$. This fine granularity allows for a high-precision particle tracking. The chip operates at 40 MHz with a 25 ns acquisition window, which corresponds to the spacing of the particle bunches in the LHC. It is hence able to correlate hits/tracks to their corresponding bunch. Furthermore, each pixel is capable of measuring the deposited charge of a detected particle by using the Time-over-Threshold (ToT) method. Finally, the FEI4 has been designed to withstand a radiation dose up to 300 MGy. This ensures a longterm stability in the radiation hard forward region of the ATLAS experiment.

Each pixel is designed as a separate entity. Its electrical chain is shown in figure 4.5. The bump-bond pad – the connection to the outside of the chip – is the input of the electrical chain, connected to a free-running amplification stage with adjustable shaping using a 4-bit register at the feedback branch. The analog amplifier is designed to collect negative charge, therefore electrons. The output is routed through

4.2. DIAMOND PIXEL MODULE

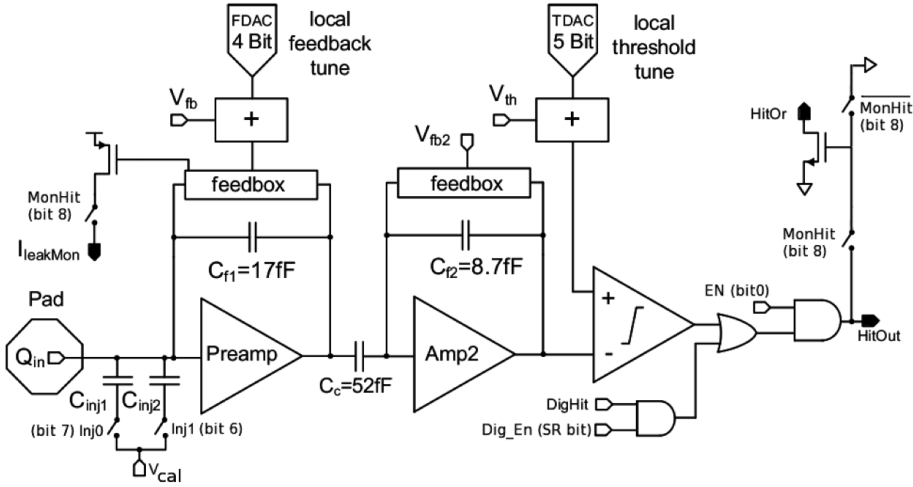


Figure 4.5: Schematic of an analog pixel. Courtesy of the FE-I4 collaboration.

a discriminator with an adjustable threshold. This value in effect defines the level at which the circuit detects a hit. In addition, there is a counter of the clock cycles (25 ns sampling) during which the signal is above the discriminator threshold. The value of the counter is proportional to the collected charge. The logic gates at the end of the chain are used to enable/disable the pixel and to issue a so-called HitOr flag – this signal is set whenever at least one of the pixels was hit and is used as a trigger for the readout. The output of the chain – HitOut – is routed into the logic of the chip where it is buffered and eventually sent out to the readout system. The module receives all its commands from the system via a 40 MHz LVDS line. The commands are either settings for the pixel registers or triggers that start the data readout. The data are sent via an LVDS line at up to 320 Mbit/s, but by default at 160 Mbit/s, four times faster than the clock of the device. This allows the chip to clear out its buffers before new data are recorded, thus avoiding dead time and data pile-up. The FE-I4 has been successfully tested for trigger rates of up to 300 kHz.

The DBM uses pCVD diamond with $d_C = 500 \mu\text{m}$ thickness and silicon with $d_{Si} = 200 \mu\text{m}$ thickness as a sensor material. The resulting most probable value (MPV) of the deposited charge for a minimum ionising particle (MIP) is calculated with the formula $Q_s = d \cdot E_{e-h}$ and equals 18000 electrons and 17800 electrons, respectively, at a full charge collection efficiency. Unfortunately this is not the case with the pCVD material, whereby the expected charge collection efficiency is of the order of 50 % – around 9000 e. This value further decreases with received irradiation dose. Therefore in order to detect the particles depositing energy on the far left side of the landau spectrum, the threshold has to be set to a significantly lower value. On the other hand, if the threshold set too low, it also detects the electronic noise and stores a false noisy hit. With the typical noise amplitudes being in the range of 120–200 e, a safe threshold range would be between $Th = 1000\text{--}3000$ e. The target for the DBM is to lower the threshold down to 800 e.

The analog amplifier is implemented in two stages to get a fast rise time at a low noise and a low power consumption. The output signal of the analog amplifier has a triangular shape with a fast rise time and a long decay. The shape can be adjusted by tuning the amplifier feedback loop. Its length is proportional to the collected charge, but it needs to be calibrated first. This is done by means of two injection capacitors, $C_{\text{inj}1}$ and $C_{\text{inj}2}$, seen in figure 4.5 with well defined capacitances. First, the charge $Q_{\text{cal}} = V_{\text{cal}} \cdot (C_{\text{inj}1} + C_{\text{inj}2})$ is injected into the analog chain. Then the length of the output pulse is measured and finally the feedback value is changed to either lengthen or shorten the pulse in order to get to the required duration t_{cal} . The typical values are $Q_{\text{cal}} = 5000 - 16000$ e at the time $t_{\text{cal}} = 5 - 10$ ToT. The target values depend on the sensor, the type of a radioactive source and the application. Therefore the initial threshold Th at 1 ToT and the calibrated value Q_{cal} at t_{cal} ToT give us a linear scale of collected charge with respect to time over threshold. However, in practice this relation is nonlinear for lower thresholds, but since the goal of the measurements is to track the particles rather than to measure their deposited energy precisely, this is sufficient.

4.3 Module assembly and quality control

Parts for the detector arrived separately and were assembled into modules at CERN’s DSF lab after being checked for production faults. The assembled modules underwent a series of quality control (QC) and burn-in tests to determine their quality, efficiency and long-term stability.

4.3.1 Assembly

A single-chip module consists of a pixel module, a flexible PCB and the supporting mechanics (a ceramic plate and an aluminium plate). The chip arrives already bump-bonded to the sensor, be it diamond or silicon. First it is glued to the ceramic plate on one side and to the PCB on the other using either Araldite 2011 or Staystik 672/472. The choice of glue was a topic of a lengthy discussion. Staystik is re-workable and has a very high thermal conductivity. The latter is important because the FE-I4 chips tend to heat up significantly and need a good heat sink. The problem is that it has a curing temperature of 160/170 °C. This temperature may cause some unwanted stress build-up between the FE-I4 and the diamond sensor due to different coefficients of thermal expansion, pulling them apart. This would disconnect the pixels, yielding large regions of the module insensitive to radiation. To avoid this, an alternative glue was tried. Araldite 2011 can be cured at lower temperatures – down to RT – but it has a lower heat conductivity. In the end Araldite is used as the safer option. However, due to the longer curing, the entire assembly process using Araldite is extended to two working days. After curing, the module is wire-bonded and attached to the aluminium plate using screws made up of a radiation-resistant PEEK plastic. They have to be tightened with a great care, because their screw head is only 0.2–0.6 mm

4.3. MODULE ASSEMBLY AND QUALITY CONTROL

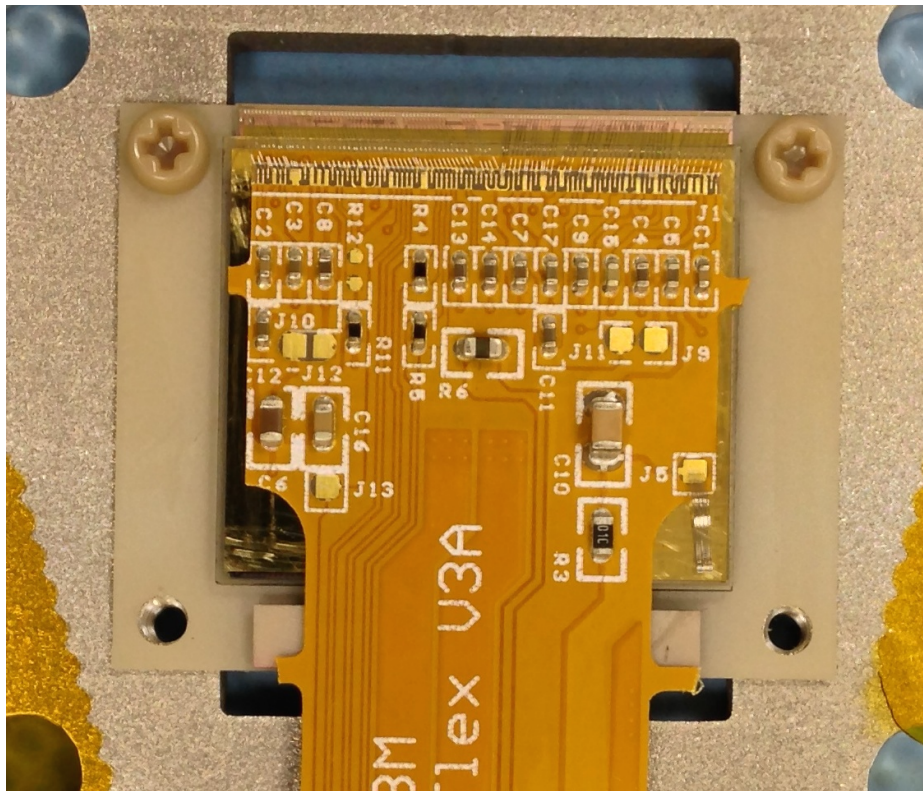


Figure 4.6: An assembled DBM module.

away from the sensor edge – the sensor displacement tolerance during gluing is of the order of 0.5 mm. Finally, the module is put in an aluminium carrier which protects it from mechanical damage or electrostatic discharges. Figure ?? shows an assembled module.

4.3.2 Testing

The modules are tested in the lab using an RCE readout system and a moving stage with two degrees of freedom. They are placed onto the stage and connected to the readout system and the power supplies. After ensuring the low- and high voltage connectivity they are checked for the signal connectivity. If everything is operational, a series of automated tests is run. Each of these tests calibrates a certain value within a pixel, whether it is the signal threshold or the value for integrated charge. These are tuned in a way that the response to a predefined calibration signal is uniform for all pixels across the sensor. This procedure is referred to as *tuning*.

When the modules are tuned, they are tested using a ^{90}Sr radioactive source. Two things are checked: 1) operation of all pixels and 2) sensor efficiency. The first test is carried out by moving the module slowly under the source while taking data so that the entire surface is scanned uniformly. The resulting occupancy map reveals any pixels that are not electrically coupled to the sensor via bump bonds. This is an important step in the DBM QC procedure, because it turned out that a significant

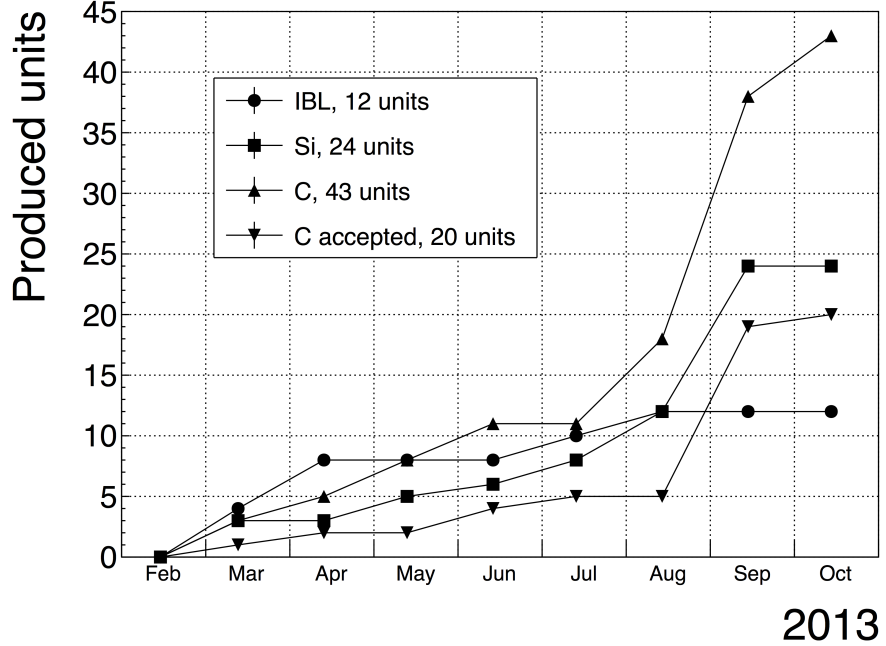


Figure 4.7: Module production with time.

portion of the flip-chipped diamond sensors exhibited very poor connectivity. The disconnected regions on the faulty modules ranged anywhere from 0.5–80 % of the overall active surface. In two cases the sensor was even completely detached from the chip. Therefore the pixel connectivity turns out to be the most important qualification factor in the QC procedure. Unfortunately the only way to check it at the moment is to fully assemble a module and test it using a radioactive source. If the module turns out to be of poor quality, it is disassembled and sent for rework. The turnover time of this operation is of the order of one month, which affected the DBM installation schedule significantly.

Only the modules that passed the pixel connectivity test undergo the second test stage in which the sensor’s efficiency was estimated. A scintillator is placed underneath the module and is used as a trigger. A particle that crosses the DBM module and hits the scintillator, triggers the module readout. In the end, the number of triggers is compared to the number of hits/clusters recorded by the module. The resulting ratio is an estimate of the sensor’s detection efficiency. The real sensor efficiency can only be measured in a particle beam and using a beam telescope as a reference detector. Nonetheless, the *pseudo-efficiency* is a rough estimate of the sensor’s quality.

The results for the DBM QC are shown in section 4.4. All in all, 79 modules went through the QC procedure – 43 diamond modules and 36 silicon modules, 12 of the latter only for testing purposes. Figure 4.7 shows their production with time. 18 diamond modules and 6 silicon modules were in the end chosen to be made up into DBM telescopes and installed into ATLAS.

4.3. MODULE ASSEMBLY AND QUALITY CONTROL

1909 A very important issue is the so called erratic current. This term describes the
1910 leakage current in a pCVD diamond that becomes unstable. It can develop gradually
1911 or can be triggered with a β source. Spikes appear in the otherwise stable leakage
1912 current. They can be up to three orders of magnitude higher than the base current.
1913 Sometimes the current also suddenly increases for a few orders of magnitude and stays
1914 at that level (e.g. from the initial 1 nA to 3 μ A). The amplitude differs in magnitude
1915 from sensor to sensor. This effect is still not fully explained, but the hypothesis
1916 is that the charges find a conductive channel along the grain boundaries, causing
1917 discharges. These discharges are picked up by the pixel amplifiers in the FE-I4. A
1918 single discharge can trigger a group of up to \sim 500 pixels, resulting in a *blob* on the
1919 detector occupancy map. Sometimes the conductive channel stays in a conductive
1920 state, making one or more pixels always to fire. These pixels only use the bandwidth
1921 of the readout channel, so they have to be masked out during measurements.

1922 4.3.3 Installation and commissioning

1923 The DBM modules that passed the QC tests were assembled into telescopes – sets of
1924 three modules one behind the other with a spacing of 50 mm. Of the 18 diamond and
1925 6 silicon modules, 6 diamond and 2 silicon modules were built. A special care was
1926 taken when choosing the sets of three diamonds. The modules with a similar pseudo-
1927 efficiency, leakage current, maximum stable high voltage and shape of disconnected
1928 regions were grouped together. After assembly into telescopes, the modules were
1929 tested for their connectivity. Then the high voltage was applied and the leakage
1930 current was observed. This was an important point to check because all three modules
1931 shared the same high voltage channel. Any instabilities on one of the modules would
1932 cause problems on the other two. This would for instance happen if one of the modules
1933 had a much lower breakdown voltage.

1934 Due to time constraints, the telescopes were not built at the same time but in-
1935 stead the production was pipelined. As soon as two telescopes were ready, they were
1936 transported to Point 1 – the site where parts of the ATLAS detector were being put
1937 together. There they were prepared for installation onto the pixel detector struc-
1938 ture that had been extracted from ATLAS due to pixel detector commissioning. The
1939 commissioning was nearing completion, so the technicians were preparing the detec-
1940 tor for re-insertion. The cylindrical structure was being closed off by four new service
1941 quarter-panels (nSQPs). This meant that with every day the access to the place
1942 of installation of the DBM was more difficult. The first two telescopes were still put
1943 into place when only one nSQP was in place. This allowed the installation process
1944 to be carried out from both sides. This proved to be helpful, because the process
1945 was lengthy and had to be done with great precision. It involved tightening several
1946 screws on both sides of the telescopes, adding thermal paste on the aluminium joints
1947 and removing the protective covers, revealing the fragile wire bonds. At the same
1948 time the surrounding electronics and cables had to be left untouched. The lessons
1949 learnt with the first part of the installation were helpful when installing the other tele-

scopes. The last two were fitted onto the structure when three nSQPs were already in place, leaving only a narrow opening for access. The entire procedure was carried out blind. After every installation, the telescopes were tested again. First, the low voltage connectivity was checked and a set of tests was run on the FE-I4 front-end chips. An eye diagram was made to estimate the quality of the signal transmission. Then a ^{90}Sr source was used to perform a source test on three modules at the same time. Leakage current was observed during the source test. The final test included running four telescopes (all on one side) at a time. All the tests were successful and the DBM was signed off.

4.4 Performance results

This section gives an overview of the performance results of the DBM modules achieved during the QC and the test beam campaign. The source tests were performed to check for disconnected regions in the sensors and to measure the diamond's pseudo-efficiency. Only the modules with minimal disconnected regions and maximum pseudo-efficiency were chosen for installation.

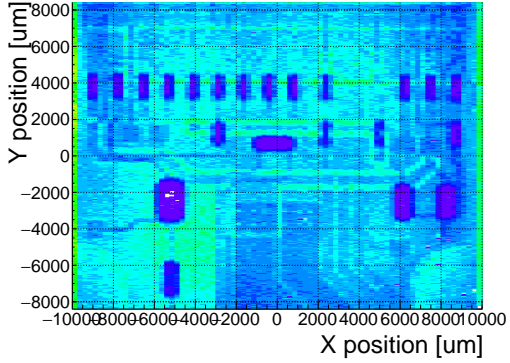
4.4.1 Source tests

All modules went through the same procedure when tested using a ^{90}Sr source – to check for disconnected regions and to measure the pseudo-efficiency.

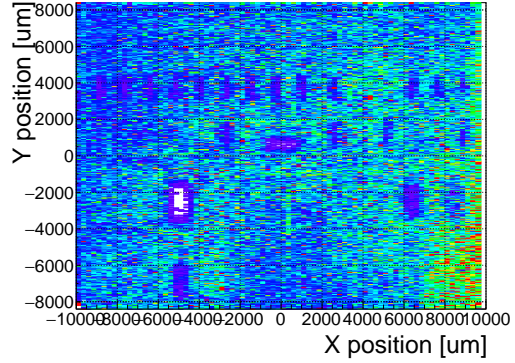
The setup consisted of a placeholder for the ^{90}Sr source, an X-Y moving stage with a holder for the module and a scintillator with a photomultiplier placed below the source and the module. The scintillator was used as a trigger – when it detected a particle, it triggered the readout of the module. If the module was placed in between the source and the scintillator, the particle had to traverse the module to hit the scintillator. Therefore, in the case of a module with a 100 % efficiency the triggered data read out by the module would need to contain at least one hit in the module. In reality the β particles scatter around the setup and sometimes hit the scintillator from other directions, without incident the module. This produces empty triggers. The phenomenon sets the limitation of measuring with a radioactive source as compared to the measurements in a test beam, in which the particles in principle always travel in one direction and their scattering is minimal.

The test for disconnected regions was carried out by moving the module under the source in X and Y direction so that the exposure over the entire plane was uniform. This resulted in an occupancy scan seen in figures 4.8a and 4.8b. The silicon module had a very uniform occupancy plot. So much so that the features of the overlaying flexible PCB can be observed. The rectangular shadows are the passive components whereas the lines are the traces in the PCB. Furthermore, a circular-shaped edge of the PCB can be seen on the bottom right side of the plot. These darker areas are such because fewer electrons can penetrate the material with a high density. In the case of the diamond, the features of the PCB can be observed as well, but are much

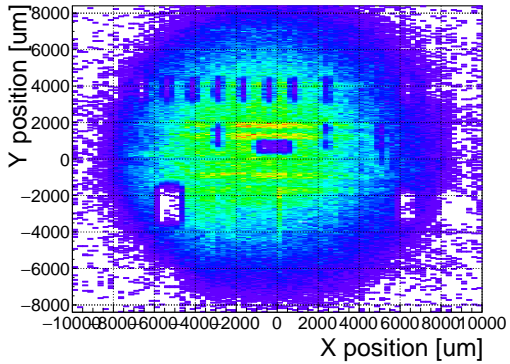
4.4. PERFORMANCE RESULTS



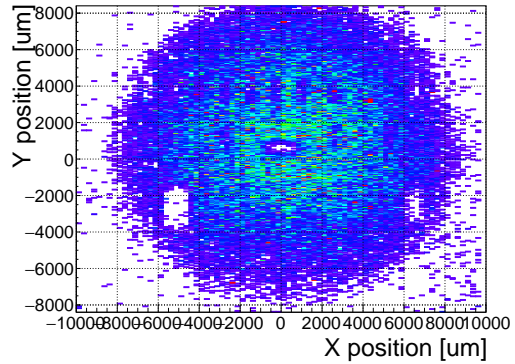
(a) Occupancy scan for MSBM-34.



(b) Occupancy scan for MDBM-23.



(c) Pseudo-efficiency scan for MSBM-34.



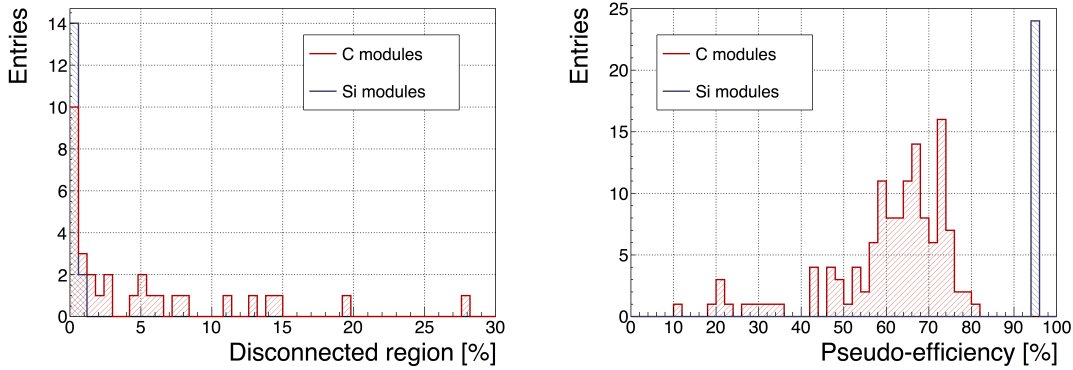
(d) Pseudo-efficiency scan for MDBM-23.

Figure 4.8: Occupancy and pseudo-efficiency scans for the silicon (left) and diamond sensor (right) to check for disconnected regions and estimate the sensor's efficiency. Shadows of the electronic components are clearly visible because fewer electrons were able to traverse through such a higher amount of material.

1989 less distinguishable. In principle, the plot is much more granulated – less uniform.
 1990 This high variance in the diamond's detection ability is due to the grain boundaries
 1991 in the pCVD material which trap the drifting charges, rendering some regions much
 1992 less efficient.

1993 The pseudo-efficiency test was carried out by placing the module directly below the
 1994 source and collimating the particles so that their trajectory was incident the module
 1995 in the middle. For every trigger by the scintillator, a script checked whether there
 1996 was a hit recorded in the module or not. The resulting ratio between the number
 1997 of triggers and number of hits recorded in the module is a pseudo-efficiency – an
 1998 estimation of the sensor's efficiency. It cannot give a precise value due to the triggers
 1999 produced by scattered particles, but at least gives a rough estimate.

2000 Figure 4.9a shows the distribution of disconnected regions across all tested mod-
 2001 ules. Silicon modules were performing as expected, with a minimum number of dis-
 2002 connected pixels. The majority of the silicon modules yielded the pseudo-efficiency
 2003 of $(94.3 \pm 0.2)\%$. Silicon sensors being 99.99 % efficient, this value was underesti-



(a) Disconnected regions for all modules derived from the occupancy scans. (b) Pseudo-efficiencies for all modules at various threshold and voltage settings.

Figure 4.9: Measurements of pseudo-efficiency and disconnected regions for all modules that went through the QC procedure.

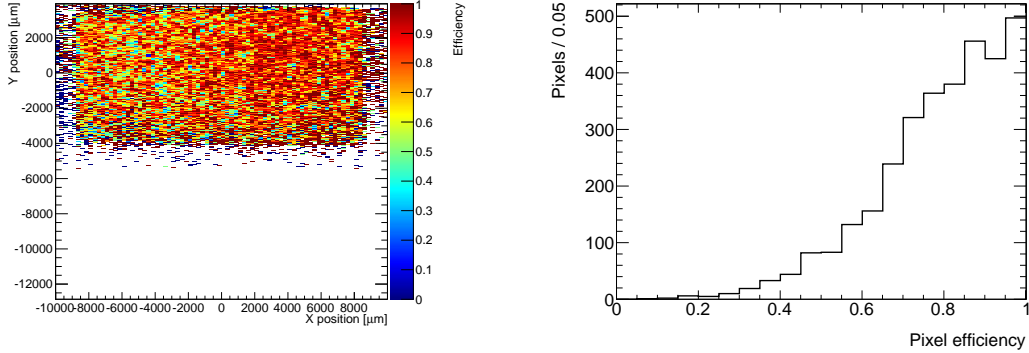
mated by about 5 %. The measured pseudo-efficiency of the diamond modules was (65 \pm 7) %, with outliers down to 10 %. The value depended on the diamond quality, the set threshold and the applied bias voltage. The latter two settings were varied to check the behaviour of the modules under various conditions.

4.4.2 Test beam results

The first two assembled prototype DBM modules, MDBM-01 and MDBM-03, were tested at DESY, Hamburg, in a test beam facility. The aim of the measurements was to measure their efficiency, the spatial distribution of the efficiency and the effect of the beam on the disconnected regions. A silicon module MSBM-02 was measured to crosscheck the measurements. Since the silicon module is almost 100 % efficient, it was used as an “anchor” – the efficiency of the diamond module was measured relative to that of the silicon module. Two beam telescopes were used as reference systems: Kartel [], built by JSI institute from Ljubljana, and EUDET Aconite []. Both are instrumented with six Mimosa26 pixel planes and capable of tracking particles with a 2 μm pointing resolution.

The test beam prototypes did not meet the acceptance criteria for production DBM modules in the following areas: first, the stated CCDs were slightly below 200 μm , which would be the DBM minimum. Secondly, the applied bias voltages ranged from 1–2 V/ μm . In addition, the threshold cut could only be set to 1500 electrons, which is higher than the DBM minimum (1000 e). Nonetheless, the resulting module efficiencies were still in the range between 70–85 %.

To analyse the test beam data, Judith [] software framework was used. Judith is capable of synchronising data streams from several detector systems only connected via a trigger system, reconstructing tracks and calculating efficiency for the DUTs. It was also used to reconstruct and analyse the acquired Kartel test beam data together



(a) This is an efficiency distribution. Each bin corresponds to a single pixel. The triggering scintillator of the Kartel telescope was smaller than the DUT. Hence, the recorded hits can only be seen in the top half of the sensor.

(b) Pseudo-efficiencies for all modules at various threshold and voltage settings.

Figure 4.10: An efficiency study of a prototype DBM diamond module in a test beam. The statistics are low (~ 10 hits/pixel) as the data was collected during a short run.

2029 with the silicon and diamond module as DUTs. A sample of the analysed data is
2030 shown in figures 4.10a and 4.10b.

2031 4.5 Operation

2032 4.5.1 Positioning

2033 The DBM is placed in the forward region of the ATLAS detector very close to the
2034 beam pipe, as shown in figure 4.12. The mechanical structure that holds the sensor
2035 planes is, due to its shape, referred to as a DBM telescope. A telescope is a system
2036 that consists of several pixel sensors placed in series one behind the other. Each
2037 DBM telescope houses three diamond pixel modules. Eight DBM telescopes reside
2038 approximately 1 m away from the collision region, four on each side. They are tilted
2039 with respect to the beam pipe for 10°. This is due to a specific phenomenon con-
2040 nected to erratic (dark) currents in diamond. Studies have shown [] that the erratic
2041 leakage currents that gradually develop in diamond can be suppressed under certain
2042 conditions. For instance, if a strong magnetic field is applied perpendicular to the
2043 electric field lines in the diamond bulk, the leakage current stabilises []. The DBM
2044 was designed to exploit this phenomenon. The magnetic field lines in the ATLAS
2045 experiment are parallel to the beam. Hence, an angular displacement of the sensor
2046 with respect to the beam allows for the leakage current suppression. However, the
2047 DBM telescopes still need to be directed towards the interaction region. Taking these
2048 considerations into account, a 10° angle with respect to the beam pipe was chosen.
2049 The influence of the magnetic field on the particle tracks at this angle is very low
2050 as the field lines are almost parallel to the tracks. The tracks are therefore straight,



Figure 4.11: This photo highlights four telescopes installed onto the nSQPs and around the pipe.

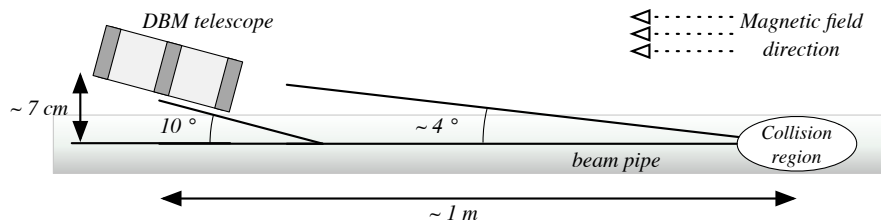


Figure 4.12: Position of the DBM in the ATLAS experiment.

2051 which reduces the track reconstruction complexity.

2052 4.5.2 Data taking during collisions

2053 The DBM has been commissioned in ATLAS and is now taking data. Several issues
 2054 still need to be resolved regarding the readout systems. Unfortunately, due to issues
 2055 with the low voltage power supply regulators, six out of 24 modules were damaged
 2056 during operation: four silicon and two diamond modules. The system configured
 2057 the modules into an unsteady state whereby they drew twice as much current as the
 2058 allowed maximum. This current most probably fused the wire bonds within minutes.

4.5. OPERATION

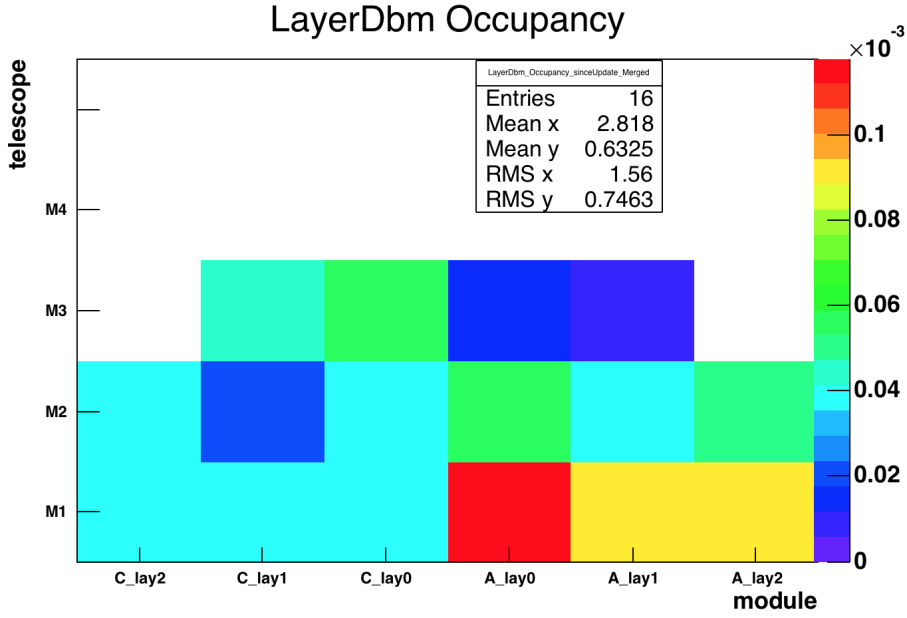


Figure 4.13: Occupancy of individual modules during collisions. Only 16 modules were taking data.

2059 This has left only five diamond telescopes fully operational. The preliminary data
 2060 obtained using the remaining telescopes show that the background rejection could
 2061 indeed work.

2062 The first step of the system test was to take data during collisions and check
 2063 the occupancy in the individual modules. The occupancies were plotted side by side
 2064 for comparison. Figure 4.13 shows some of the occupancy values. At the time, the
 2065 readout system was not yet configured to read out all telescopes in parallel.

2066 The second step was to test the detector's capability of particle tracking. Only one
 2067 telescope was used to take data with the beam. If all three planes of the telescope
 2068 were hit during a bunch crossing, a linear line was fitted to the hits. This line
 2069 represented the particle's trajectory. It was projected towards the interaction point.
 2070 Two parameters were calculated where the line is the closest to the interaction point:
 2071 the radial distance and the longitudinal distance between the line and the interaction
 2072 point, as shown in figure 4.14. This was done for the events with two colliding bunches
 2073 as well as for events with only one, non-colliding bunch. The tracks recorded during
 2074 the events with two colliding bunches could either come from the collisions or could
 2075 be background scattering. Tracks recorded during a non-colliding bunch, on the
 2076 other hand, are definitely background particles since, in principle, there should be no
 2077 collisions taking place.

2078 A comparison of the data acquired and depicted in figures 4.15a and 4.15b showed
 2079 that, for the colliding bunches, the majority of the reconstructed tracks had the origin
 2080 in the interaction point, with an expected spread in Z and R . For non-colliding
 2081 bunches, the distribution is more spread out. In the Z_0 plot the distribution has one

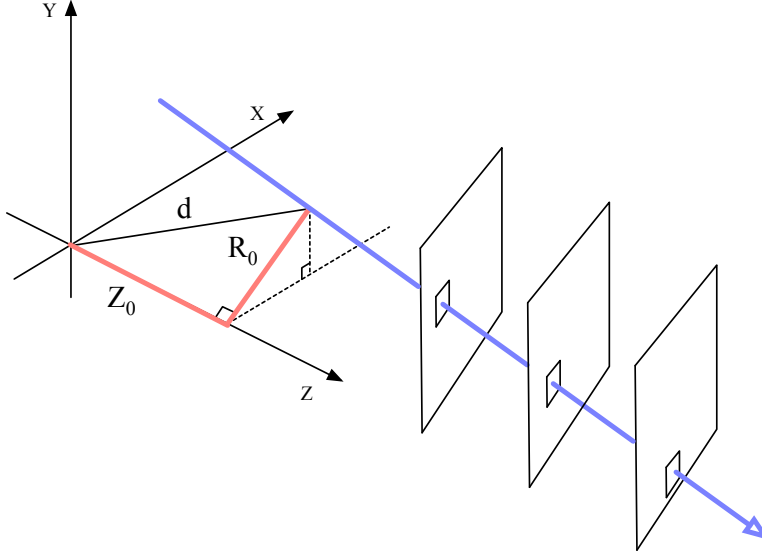


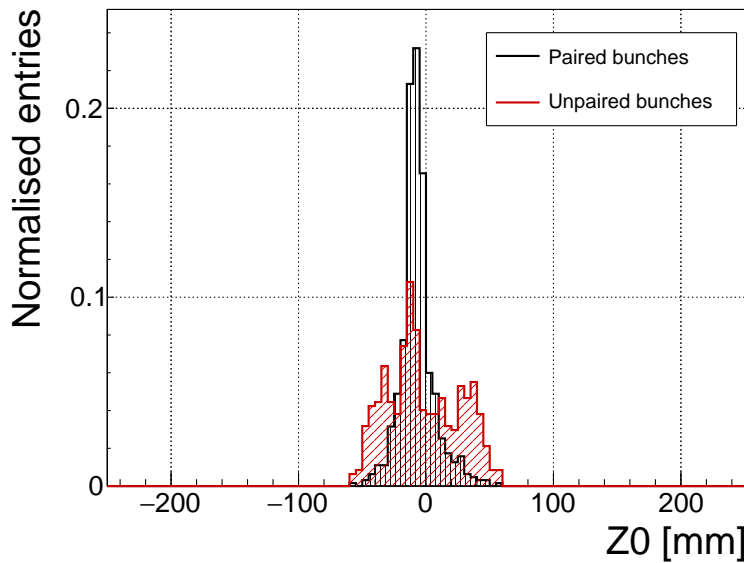
Figure 4.14: A diagram showing the radial distance R_0 and longitudinal distance Z_0 of the trajectory from the interaction point at the minimal distance d . Z is the axis along the beam line. Three module planes intercept a particle and reconstruct its trajectory.

peak in the middle, which means that the empty RF buckets still held some particles. The two peaks on the sides, however, show that a significant number of tracks had their origin at the radius of the beam pipe. Therefore these tracks were made by stray protons colliding with the beam pipe. These collisions are unwanted as they do not produce any meaningful physics while still damaging the ATLAS detector by means of the scattered radiation.

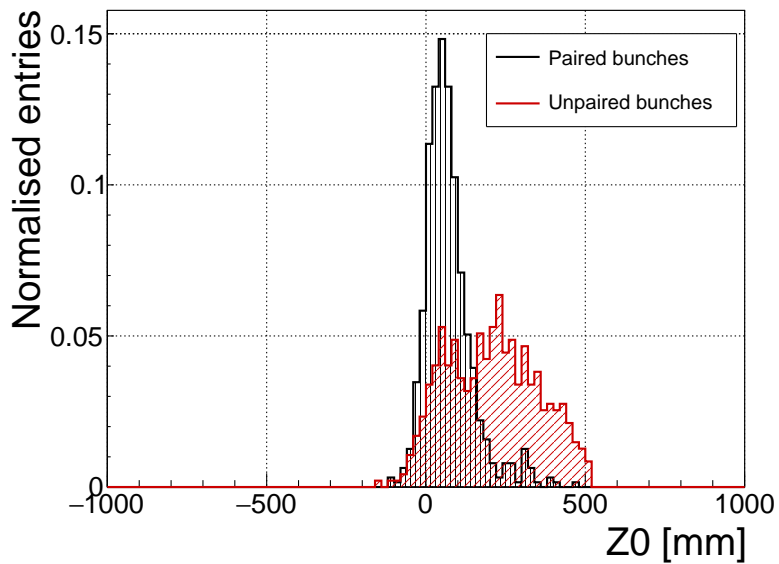
4.6 Conclusion

The Diamond Beam Monitor has been designed as an upgrade to the existing luminosity detectors in the ATLAS experiment. It is the first diamond pixel tracking detector installed in a high-energy physics experiment. The pixelated front-end electronic chips ensure precise spatial detection of the charged high-energy particles. The projective geometry allows for particle tracking and background rejection. The detector is placed in a high-radiation forward region of the experiment. Therefore, radiation hardness of the chosen pCVD diamond sensors is an important requirement. The tests carried out in the test beam and in the laboratory confirmed that enough detector-grade DBM modules have been built to be installed in the experiment. The DBM is now running in ATLAS during collisions. Further improvements have to be made on the readout firmware before it is included in the main readout stream.

4.6. CONCLUSION



(a) Radial distance of the particle trajectories from the interaction point.



(b) Longitudinal distance of the particle trajectories (along the beam path) from the interaction point.

Figure 4.15: These two plots show two parameters of particle tracks recorded by one of the DBM telescopes: radial and longitudinal distance of the projected tracks from the interaction point.

2100 **Chapter 5**

2101 **Current monitoring**

2102 ***Real-time particle identification***

2103 Diamond sensors have a very fast signal response due to their low capacitance. The
2104 electrical signal created by drifting charge carriers retains its shape without significant
2105 distortion. When the sensor is used together with a fast current amplifier with a high
2106 broadband limit (~ 2 GHz) and a readout device with a similar limit, the information
2107 about the drifting charges is retained. For instance, a proton creates the free e-h pairs
2108 along its trajectory. The electrons and holes start drifting immediately. Those closest
2109 to the electrodes recombine quickly whereas those at the opposite side contribute to
2110 the induced signal for longer. The resulting signal is therefore a triangular pulse
2111 with a steep rising edge and a gentle falling edge. It is possible to determine the
2112 drift velocity of the charge carriers by measuring the width of the pulse, as was done
2113 in chapter 3. Furthermore, it is possible to determine with a certain probability
2114 what is the type of incident radiation, judging by the shape of the induced pulse.
2115 This, however, only applies to sCVD diamond material. Its uniform carbon lattice
2116 allows the ionisation profiles to retain their shape, unlike in pCVD material, laden
2117 with grain boundaries, or in even in silicon where the shape is deformed due to p-n
2118 junction non-uniformities.

2119 This chapter describes an application that carries out particle identification by
2120 means of the pulse shape analysis. It was developed for measuring activity of a
2121 neutron reactor. In this case the device has to be able to filter out the photon
2122 background with a rate several orders of magnitude higher than the neutron rate.
2123 Overall detected rate in a neutron reactor can easily exceed 10^8 particles $\text{cm}^{-2}\text{s}^{-1}$,
2124 depending on the distance of the detector from the reactor core. The device has to
2125 be able to cope with such high rates. It also needs to be dead time free or at least
2126 close to that, to minimise the counting error. At these rates, it still has to be able to
2127 identify the types of pulse. This type of online analysis cannot be done in software.
2128 It has to be implemented in an FPGA.

5.1 Motivation

Pulse shape analysis (PSA) is a common software tool for analysing sensor response to incident particles. It is usually done by means of software that runs over big amounts of data that have been acquired and saved to storage. This offline analysis can be repeated and improved. However, the saved data take up a lot of storage space. In addition, saving raw waveform data requires a system capable of a high data throughput and fast data storing. For instance, an oscilloscope can save up to 100 signal waveforms per second. This means that there is a high measurement dead time. To avoid the high dead times, the software algorithms can be ported to the FPGA where they analyse the incoming signal in real time. The signal is then discarded and only the analysis results are saved, decreasing the storage space significantly.

The offline pulse shape analysis has already been used for particle identification with a diamond sensor [29, 23]. An effort has been made to implement an online and real time application for this analysis by porting the algorithms into an FPGA. This section first describes the device specifications Then it describes in detail the PSA algorithms and the structure of the code. Afterwards it discusses the performance results, which showcase the limitations of the device. Finally it describes the data acquired with radioactive sources and in neutron reactors.

5.2 Requirements

Chapter 3 shows that the shape is heavily dependent on several factors, such as environmental temperature and received irradiation dose. At temperatures lower than 150 K the signal from an α starts deteriorating due to recombination of charges in the charge cloud. Sensor irradiation, on the other hand, introduces charge traps, which cause the signal to decay exponentially. These two factors are a significant limitation for particle identification. Priming can improve the charge collection and longterm stability of the pulse shapes. To improve the measurement further, a high bias voltage has to be applied, increasing the measurement SNR.

Factor	Operating range
Sensor material	sCVD diamond
Sensor thickness	500 μm
Temperature	150 K – 400 K
Radiation dose	1×10^{13} neq $\text{cm}^{-2}\text{s}^{-1}$
Charge carriers	holes
Bias voltage	$\sim 1 \text{ V } \mu\text{m}^{-1}$
Signal-to-noise	5

Table 5.1: Limitations to particle identification.

2159 5.3 Device specifications

2160 The ROSY box has a single BNC input with the termination $50\ \Omega$ or $1\ M\Omega$ with a
2161 DC or AC coupling. The analog chain has a 250 MHz bandwidth limit. The input
2162 range can be set from $\pm 50\text{ mV}$ up to $\pm 5\text{ V}$. The signal offset can be set to any value
2163 within this range. The ADC samples this signal with an 8-bit precision at a rate of
2164 up to 5 GSPS. The PSA uses the highest sampling to achieve width measurement
2165 resolution of 0.2 ns. The spectroscopic application does not need such a fine timing
2166 resolution and therefore operates at a reduced sampling rate of 0.8 ns. The amplitude
2167 resolution depends on the chosen input range, but at 256 ADC counts per sample, it
2168 can be as low as 0.39 mV s^{-1} at the range of $\pm 50\text{ mV}$ and as high as 39 mV s^{-1} at
2169 the range of $\pm 5\text{ V}$.

2170 The logic structure of the PSA is designed using VHDL and runs on Xilinx Virtex 5. The PSA is capable of a maximum counting rate of 1.56×10^8 pulses per second,
2171 yielding a 6.4 ns double pulse resolution. The analysis is more time consuming; the
2172 maximum throughput rate of the pulse shape analysis is $\sim 5 \times 10^6$ pulses per sec-
2173 ond. This means that after every pulse, the device has a dead time of approximately
2174 (200 ± 15) ns, depending on the width of the pulse being analysed. Any pulse arriving
2175 during the analysis of the previous one is counted, but not analysed. Any two pulses
2176 with the distance between the rising edges lower than 6.4 ns are counted as a single
2177 pulse.

2178 The device is very sensitive to noise pick-up. Therefore the setup must be designed
2179 to minimise the pick-up by means of proper shielding, use of high-quality cables etc.
2180 The relatively low bandwidth limit filters out some high-frequency noise, but not the
2181 ringing or higher noise spikes. That is the task for the PSA.

2183 5.4 Pulse parameters

2184 A signal pulse on the input is parametrised during the analysis process. The PSA
2185 measures its amplitude, area, width and the slope of its falling edge, as shown in
2186 figure 5.1. The amplitude is the difference between the baseline and the highest
2187 sample in the pulse and is given in ADC counts as an 8-bit value. The area is defined
2188 as the sum of amplitudes of all samples between two defined boundaries within the
2189 pulse. The width is defined as the number of samples with a value higher than a set
2190 amplitude threshold. If the threshold is at half the maximum amplitude, the resulting
2191 width is *full width at half maximum* (FWHM). The falling slope is the maximum
2192 negative difference between values of two samples and is given in ADC counts per
2193 sample. These parameters can also be used as *qualifiers* for accepting or discarding
2194 a pulse. All four parameters limited by the low and high limit are called a *qualifier*
2195 *set*. For instance, a rectangular pulse by an α particle always has the same FWHM
2196 and a very steep slope. In comparison, a photon has a lower falling slope value and
2197 a narrower FWHM. Therefore the low and high cut on these two qualifiers allow for
2198 a discrimination between the two pulses. Another qualifier is a *form factor* and is

5.5. APPLICATIONS

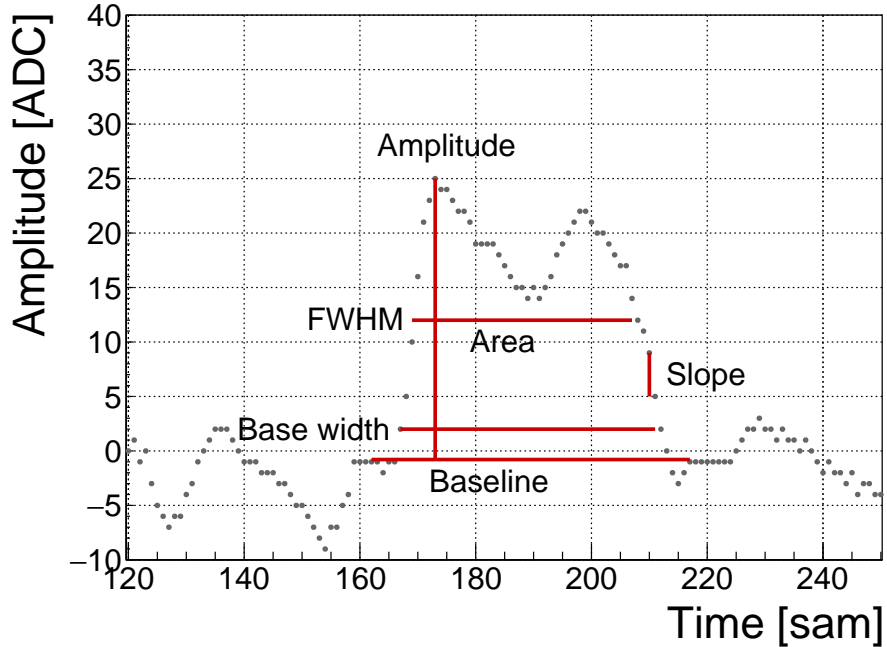


Figure 5.1: A pulse and its parameters.

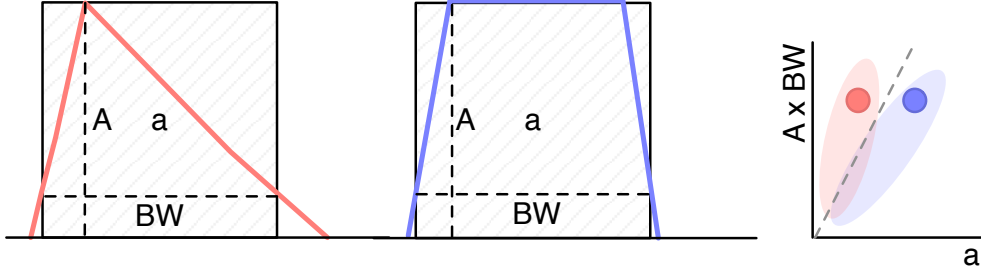


Figure 5.2: Form Factor is the ratio between the measured area (a) and the calculated area ($A \times BW$) of the pulse. The calculated area is significantly larger than the measured area for a triangular triangular pulse, but less so for the rectangular one. The red and blue dot in the right plot are the value entries of the two pulses shown. The red and blue oval shapes depict the regions for the values expected from triangular and rectangular pulses. By carefully choosing the linear qualifier (dashed line) and taking only the entries below the cut rectangular pulses can be identified.

2199 defined as the ratio between the measured area and the amplitude multiplied by the
2200 width. By comparing the measured and the calculated area the difference between a
2201 triangular and a rectangular pulse can be inferred, as shown in figure 5.2.

2202 **5.5 Applications**

2203 The FPGA firmware is designed for systems instrumented with CIVIDEC amplifiers
2204 and CIVIDEC sVCD diamond detectors. Three applications are available: *Spectroscopy*,
2205 *Pulse Shape Analysis* and *Counter*, each optimised for a specific task. Their
2206 capabilities are described below. The firmware runs in ROSY, a readout system
2207 produced by CIVIDEC.

2208 **Spectroscopy** is a tool for measuring energy spectra of radioactive sources. It is
2209 used in combination with the CIVIDEC Cx spectroscopic charge amplifier. The
2210 signal from the charge amplifier is analysed in real time. The FPGA measures the
2211 maximum amplitude of the signal. The amplitude value is ready at the end of the
2212 pulse and is stored in the amplitude histogram. Immediately after, the analysis is
2213 reset and the system is ready for a new acquisition. Upon request from the software,
2214 the histogram is read out, during which the analysis is paused. In addition to the
2215 histogram building, the firmware can also store raw pulse waveforms, which can be
2216 then read out by the software. The maximum allowed throughput is 1 million counts
2217 per second.

2218 **Pulse Shape Analysis** is a tool for measuring energy spectra of radioactive sources,
2219 with an additional feature. It can identify the type of radiation detected by the
2220 diamond detector. By means of the pulse analysis it can subtract the background
2221 radiation and only measure the signals from the defined radiation source. It is used
2222 in combination with the CIVIDEC C2 fast current amplifier. The firmware receives
2223 a current pulse from the detector and digitises it. The pulse is then analysed and
2224 parametrised. The analysis module measures its maximum amplitude, full width
2225 at half maximum (FWHM), baseline amplitude, falling slope and its area. Then
2226 it compares the obtained pulse parameters with the qualifiers set by the software
2227 and determines what type of radiation hit the diamond detector. Depending on the
2228 qualifiers, the pulse can either be *accepted* or *rejected*. The firmware then stores the
2229 parameters of the analysed pulse into histograms. Two histograms exist for each
2230 parameter: one for all pulses and one for accepted pulses. In addition, there is one
2231 2D histogram (a scatter plot), which can plot two parameters one with respect to the
2232 other. Upon request from the software, all histograms are read out, during which the
2233 analysis is paused. The maximum allowed throughput is 1 million counts per second.

2234 **Counter** is a tool that measures the count rate and the mean time during counts.
2235 It is used in combination with the CIVIDEC Cx, C6 or C2 amplifier. It contains
2236 one histogram which holds the information about the mean time during counts. The
2237 counter is operational also during the readout of the histogram. The highest counting
2238 rate with enabled histogram writing is $3 \times 10^7 \text{ s}^{-1}$.

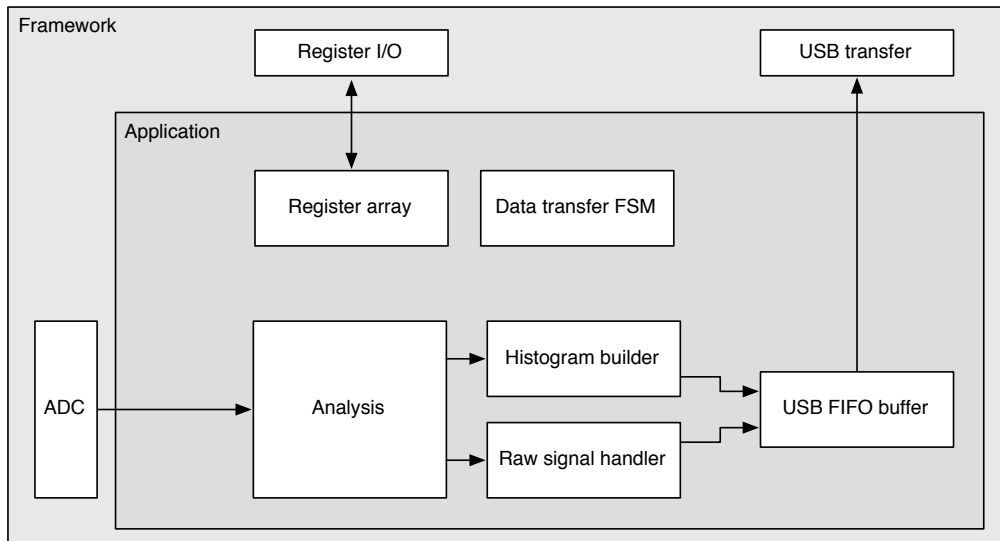


Figure 5.3: Firmware design structure.

5.6 Description of the firmware

The applications are built on top of the Picotech platform. The base code handles the communication between the software and the hardware. Furthermore, it provides the interface to the ADC data, the input/output registers and the USB data transfer. The applications have a set of modules that handle the data input and output and a module for signal analysis, as shown in figure 5.3. The data handling modules are very similar in all the applications to ensure compatibility of the communication between software and firmware and the readout data format. The analysis module, however, is different from one application to the other. The data handling layer is the same for all applications and consists of the final state machine (FSM), the histogram builder, the raw signal handler, the USB FIFO buffer and the register array.

The firmware is written entirely in VHDL. The diagram in figure 5.3 shows the module architecture. The ADC provides the module with 32 digitised signal samples every clock cycle (6.4 ns). The signal is routed directly to the pulse analyser and into the raw signal handler. The analyser outputs are connected to the I/O registers and to histogram buffers. Both the histogram buffers and raw signal buffers are connected to the USB FIFO through a multiplexor. The firmware communication to the controller is done via input/output (I/O) registers (control and status registers, counters) and serially via USB (histogram data, waveforms).

5.6.1 Design constraints

Speed The ADC provides 32 8-bit samples on every 6.4 ns clock cycle. It is not possible to e.g. sum all 32 values in a single cycle, because the summation takes too long to complete. This is why the summation has to be pipelined and carried out

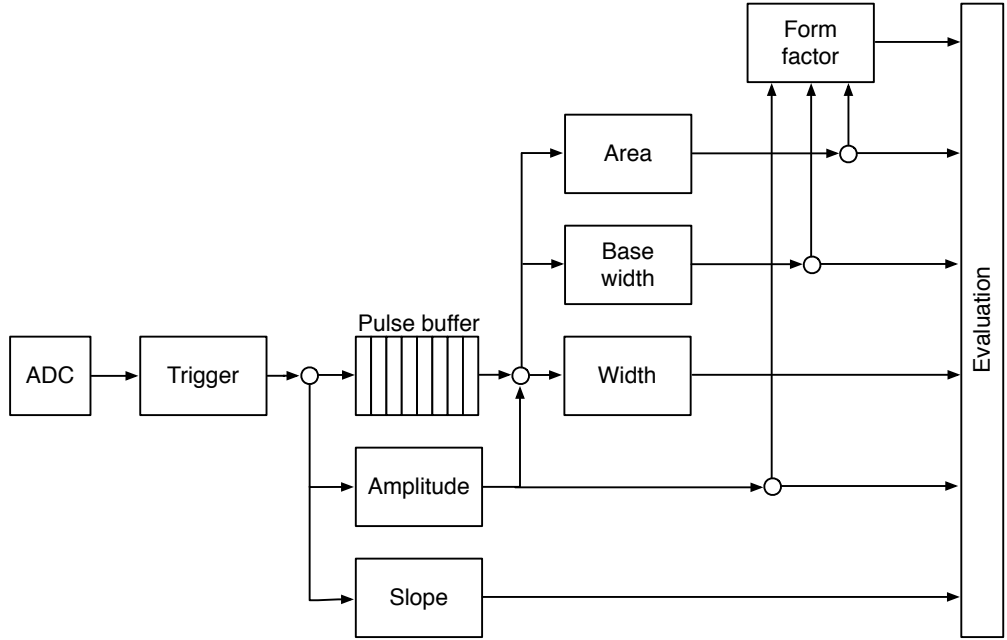


Figure 5.4: Code design plan.

in three cycles. This adds up to the analysis duration, which in turn decreases the maximum pulse rate.

Firmware size The PSA application makes use of a number of FIFO and RAM buffers to store the pulse waveforms and histograms. 48 32k block RAM modules have been used for the implementation, maxing out the available block RAM memory space on this FPGA. The analysis algorithm also takes up a significant portion of the FPGA. Many of the operations are carried out on 256-bit long numbers received from the ADC, which quickly fills up the available logic. This is also why the place and route procedure takes a long time.

Power consumption The reduction of the power consumption is not crucial for the intended applications.

5.6.2 Analysis module

This module is different for different applications. The Pulse Shape Analysis (PSA) application has the most complex module design. The spectroscopy application only uses a small part of that design and the Counter application an even smaller one.

The analysis (or parametrisation) is carried out in several steps, as shown in figure 5.4. The triggering block starts the readout upon signal threshold crossing. The maximum slope of the falling edge is observed. The Amplitude block calculates the pulse height and retains the maximum amplitude while pushing the signal into the pulse buffer. Then the entire pulse is clocked out of the buffer while its FWHM,

5.6. DESCRIPTION OF THE FIRMWARE

2282 baseline width and area are measured. Finally, the Form factor is calculated. At the
2283 end the Evaluation block takes in all the parametrised information and classifies the
2284 pulse according to user-defined cuts.

2285 **Triggering** module handles signal polarity swapping, triggering on threshold and
2286 defining the trigger window. The real-time processing algorithm allows for a positive
2287 or an inverted input signal. However, the PSA only handles positive-polarity pulses.
2288 Therefore a negative signal is swapped in the *triggering* block. Signal analysis and
2289 readout are then triggered when the signal crosses a user-defined threshold. In addition,
2290 the signal has to be over the threshold for a defined number of samples. This is
2291 to avoid triggering on noise spikes. A double clock cycle delay is used on the signal
2292 to make sure that the recorded signal window includes the rising edge of the pulse as
2293 well as some baseline before it. A *trigger active* signal marks a window that contains
2294 the entire pulse including some baseline signal before and after it. The trigger can
2295 be vetoed by three signals: if the pulse analysis is still taking place, if the input
2296 signal exceeds the maximum voltage range or if the data transfer FSM is pausing the
2297 analysis due to data transfer to the controller.

2298 **Amplitude** block calculates the pulse height from the difference between the pulse
2299 and the baseline. It also finds the position of the maximum amplitude within the
2300 clock cycle. It receives 32 8-bit samples from the triggering block every clock cycle.
2301 Time delays in the logic prevent it to find the maximum value of the 32 samples
2302 within one clock cycle (6.4 ns). Therefore the decision logic has been pipelined in
2303 three stages, which means that the final maximum value is ready three clock cycles
2304 after the end of the pulse.

2305 **Pulse buffer** is a FIFO that stores the signal while its amplitude is being measured.
2306 At the end of the pulse the FIFO is read out so that the remaining measurements
2307 can take place.

2308 **Width** block uses the maximum amplitude to determine the *half-maximum* and to
2309 measure the FWHM. To do so, it counts the samples that are above the half-maximum
2310 amplitude. However, this method might also count high enough noise spikes before
2311 or after the pulse. Hence an improved method, which “cleans” the measurement of
2312 unintentional additional noise, has been implemented. It is described in section 5.6.3.

2313 **Baseline width** block is the same as the Width block, but it measures the width
2314 either at 50 %, 25 %, 12.5 % or 6.25 %, depending on the setting in the register. It
2315 also makes use of the special method described in 5.6.3 to avoid overestimations due
2316 to including noise in the measurement.

2317 **Area** block measures the pulse area by summing up the amplitude values of the sam-
2318 ples in the pulse. The boundaries of the summation are defined with the crossing of
2319 the amplitude above a certain threshold. Only the samples between those boundaries
2320 are summed up. The boundaries can be set at 50 %, 25 %, 12.5 % or 6.25 % of

2321 the maximum amplitude of the pulse. The area measurement makes use of the same
2322 routine as the FWHM and Baseline width block to remove the potential outlying
2323 samples.

2324 **Falling slope** block measures the highest negative difference between amplitudes of
2325 two adjacent samples, thus getting the maximum negative slope of the pulse. It is an
2326 experimental routine, only used for academic purposes.

2327 **Form factor** block is used as a special qualifier for particle identification. It com-
2328 pares the weighted measured area of the pulse with its weighted calculated “form”,
2329 which is defined as the multiplication of the measured amplitude and baseline width.
2330 The equation is as follows:

$$x \cdot a - y \cdot A \cdot BW \geq 0, \quad (5.1)$$

2331 where a is the measured area, A is the amplitude, BW is the baseline width and x
2332 and y the weighting factors for the measured and calculated area, respectively. The
2333 output of the block is the boolean result of this equation.

2334 **Evaluation** block takes in all the parameters from the analysis blocks and compares
2335 them against the user-defined qualifiers. If the parameters are within the bounds,
2336 the pulse is accepted, otherwise it is rejected. The corresponding counters within the
2337 block are incremented.

2338 5.6.3 Area and width measurement

2339 The routine for measuring pulse area and width must have a specific algorithm imple-
2340 mented to carry out the measurements correctly. The core point is that the routine
2341 precisely defines the edges of a pulse. It does so by means of *vector cleaning*, pre-
2342 sented in figure 5.5. An important input, beside the ADC data and the measurement
2343 threshold, is the position of the sample with the highest amplitude.

2344 The signal arrives from the ADC as a set of 32 8-bit samples every every clock cycle
2345 with a period of 6.4 ns. All 32 samples are compared against the width measurement
2346 threshold. If a sample value is equal or higher than this threshold, a binary 1 is set
2347 in a 32-bit *vector* on the position corresponding to the position of the sample in the
2348 incoming ADC data set. The resulting vector might also include some noise at the
2349 edges of the pulse, depending on the height of the width measurement threshold. The
2350 old routine simply counts the binary ones in this vector to get the pulse width. This
2351 works well for measuring the FWHM because the threshold was high. However, for
2352 width measurements at 25 %, 12.5 % or 6.25 % of the pulse height this might already
2353 become a problem, because the noise might be counted in as well. This is why the
2354 new routine cleans the outliers in this vector before counting the remaining ones in
2355 the clean vector.

2356 The routine starts from the position of the maximum height. It follows the vector
2357 in both ways and finds the first falling edge (0 at this position and 1 at the previous

5.6. DESCRIPTION OF THE FIRMWARE

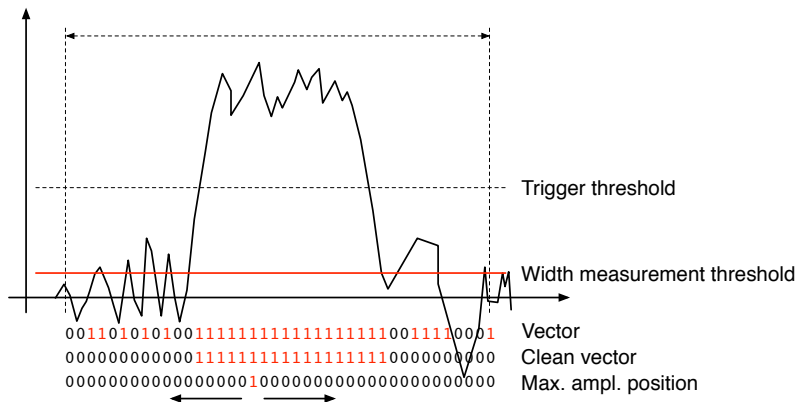


Figure 5.5: A sample pulse. The first vector shows which samples are above the width measurement height. The second vector is a clean vector. The third line shows the position of the maximum amplitude. The vector cleaning algorithm starts from the maximum amplitude and continues in both ways along the vector.

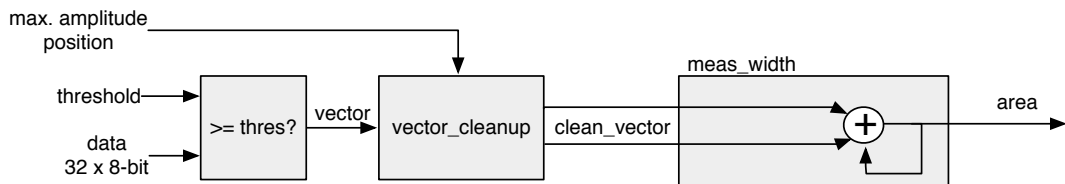


Figure 5.6: This block counts the remaining binary ones in the clean vectors and outputs this value as the pulse width.

2358 one). From there on it rewrites any binary 1 with a binary 0. The resulting clean
 2359 vector only has one bunched set of binary ones which are summed, yielding a precise
 2360 pulse width. The area measurement is similar - it only integrates over the samples
 2361 marked in the clean vector. Both measurement routines, for area and for width, are
 2362 implemented separately so that the area routine can have a different threshold set.

2363 This section explains how the algorithm is designed. First, the idea for it was
 2364 tested using Excel and was only afterwards ported to the VHDL. The underlying
 2365 algorithm first cleans the vector. Then it passes the cleaned vector either to the
 2366 width or area measurement, as shown in figures ?? and ???. The width measurement
 2367 module only sums the ones in the vector whereas the area measurement module sums
 2368 the data samples marked by the cleaned vector. Both modules issue a *valid* signal
 2369 when they finish the measurement.

2370 5.6.3.1 Vector cleaning

2371 This is the most important block. Its inputs are: *vector*, *parsing active*, *position of the*
 2372 *max. amplitude (PA)* and its delay (*DA*). *PA* is a 32-bit binary number that shows the
 2373 position of the sample with the maximum amplitude within the data block whereas

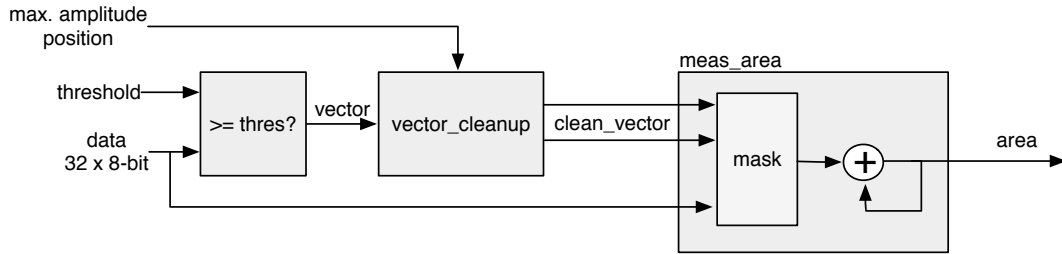


Figure 5.7: This block masks the input data with the clean vector and sums the remaining samples.

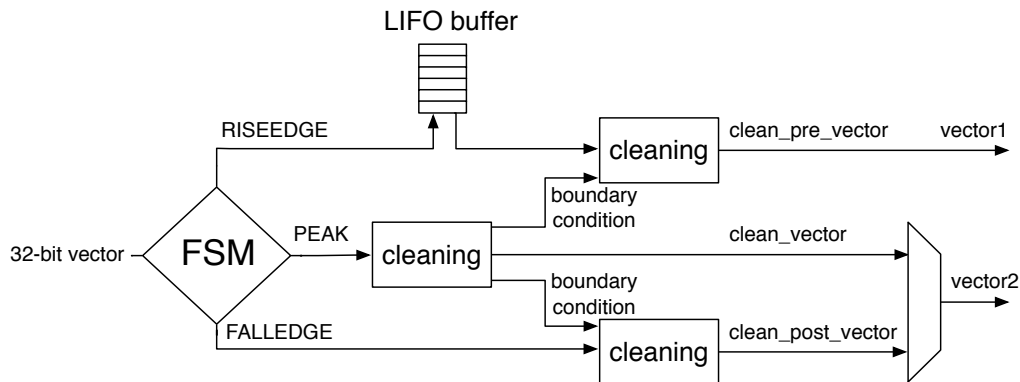


Figure 5.8: Vector cleaning routine outputs two vectors - one forward in time and one back in time from the peak of the pulse.

2374 the DA tells us how many clock cycles after the start of the parsing this PA block
 2375 is. The vector cleaning module is designed as a final state machine (FSM) with the
 2376 states IDLE, RISEEDGE, PEAK, FALLEDGE and READY. The FSM is idle until it
 2377 receives the *active* signal from the external module, marking that the vector parsing
 2378 has commenced. It switches to RISEEDGE, which starts two procedures: 1) it fills
 2379 the vector of the pulse's rising edge into a last-in-first-out (LIFO) buffer and 2) counts
 2380 down from the DA value. When this counter reaches 0, the FSM changes its state to
 2381 PEAK because the current vector on the input is the one containing the maximum
 2382 amplitude. This data block is sent through the *peak algorithm*, which cleans the
 2383 vector. The FSM switches to FALLEDGE state. Now both the previously buffered
 2384 vector of the rising edge and current vector of the falling edge go through the *pre-*
 2385 *and post- algorithm* where they are cleaned, but they get their boundary conditions
 2386 from the *peak algorithm*. The output of this module is therefore two cleaned vectors
 2387 in parallel – one forward in time and the other backwards.

2388 5.6.3.2 Algorithm

2389 The underlying algorithm is sequential - it carries out a logic operation on vector bit
 2390 on position 0, uses the output of this operation for the operation on bit on position

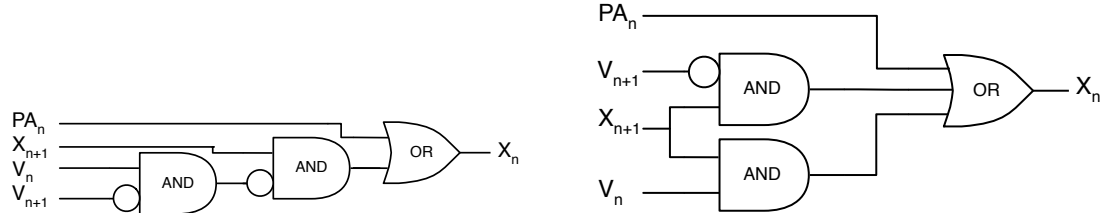


Figure 5.9: One logic step in the algorithm chain before and after Karnaugh minimisation.

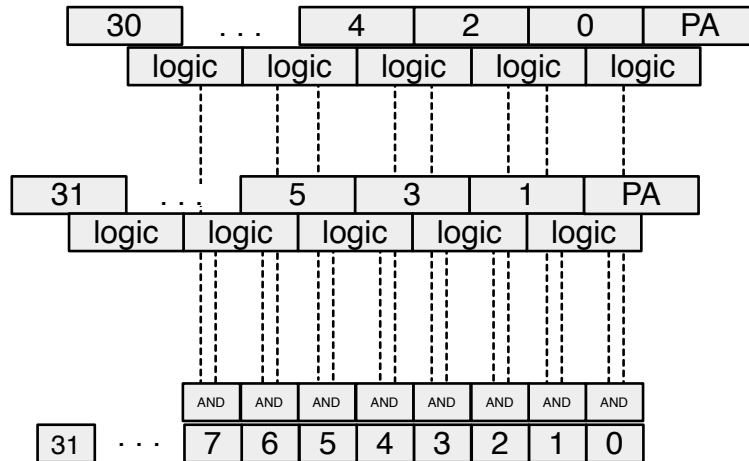


Figure 5.10: Vector is divided into two 16-bit logic chains. The algorithm logic is then run on the two chains separately. The results are then merged into one 32-bit clean vector by using a set of AND gates.

2391 1 and so on. This means that it has to carry out 32 logic operations per clock
 2392 cycle. With each operation taking approximately 0.3 ns, the entire logic chain takes
 2393 approximately 10 ns to complete. With only 6.4 ns per clock cycle, this means timing
 2394 errors would occur. To fix the problem, a more complicated *decimated algorithm* has
 2395 been designed. It consists of two parallel logic chains. Each of the two only takes
 2396 every second bit into account (chain one: 0, 2, 4 ..., 30. Chain two: 1, 3, 5 ..., 31).
 2397 This makes the chains effectively 16 bits long. The algorithm is run on the two chains
 2398 and the results are merged together at the end as shown in figure 5.10. This effectively
 2399 reduces the number of sequential logic operations to around 18, which is within the
 2400 timing constraints.

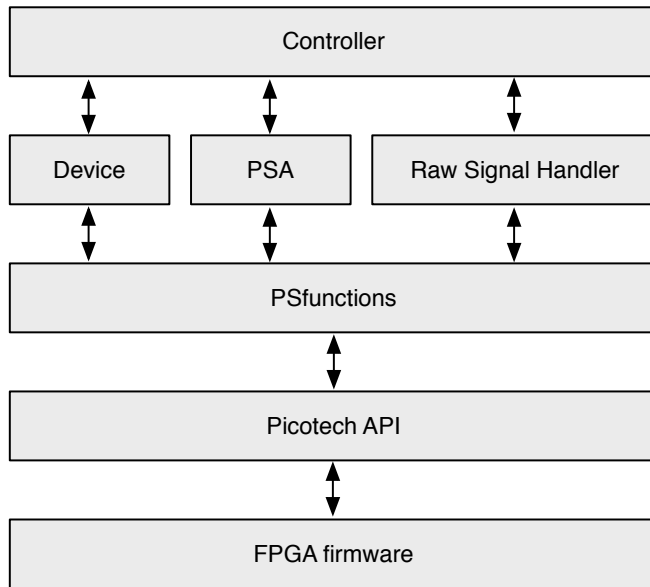


Figure 5.11: Abstraction levels of the controller software.

²⁴⁰¹ 5.7 Control and data interface

²⁴⁰² Communication between the device and the controller PC is done via the API func-
²⁴⁰³ tions provided by the producer. In addition, the API used by CIVIDEC has access
²⁴⁰⁴ to several extra functions. These allow the user to download a customised bitfile to
²⁴⁰⁵ the FPGA, access the I/O registers and use the USB data transfer.

²⁴⁰⁶ 5.7.1 Software

²⁴⁰⁷ The software has been designed in C++ in several levels of abstraction. Figure 5.11
²⁴⁰⁸ shows the structure of the classes. The classes Device, PSA and RawSignalHandler
²⁴⁰⁹ are there to make it easier to read and understand the controller code. In principle the
²⁴¹⁰ PSfunctions can also be accessed directly by the controller, but for this the instruction
²⁴¹¹ sequences must be well known and understood.

²⁴¹² 5.7.2 Data readout

²⁴¹³ The device records the data in two forms - as signal waveforms and as histograms
²⁴¹⁴ of analysed pulse parameters. Both are available upon request from the controller.
²⁴¹⁵ Only one of the two can be transferred via the USB line at a time.

²⁴¹⁶ The waveforms are saved into a FIFO buffer, which can hold up to 64 pulses of the
²⁴¹⁷ length of \sim 500 samples. The data format for each pulse is such that it starts with a
²⁴¹⁸ header containing the pulse timestamp and the sequential number, continues with the
²⁴¹⁹ data samples and ends with a header containing all the measured parameters (width,

5.8. PERFORMANCE RESULTS

2420 amplitude, area, falling slope and form factor). When the FIFO is full, it issues a
2421 flag, which tells the controller that the data buffer is ready for readout.

2422 The histograms are implemented into the FPGA's Block RAM. Their size ranges
2423 from 256 to 4096 bins (an 8-bit or a 12-bit histogram, respectively), depending on the
2424 required histogram resolution. For instance, the width parameter is measured with a
2425 0.2 ns resolution; the expected maximum pulse width is less than 20 ns. This yields
2426 the maximum range of 100 bins, making an 8-bit histogram sufficiently large. The
2427 same reasoning is applied to the amplitude measurement. In this case the maximum
2428 range is defined by the 8-bit resolution of the ADC. The area measurement, however,
2429 yields higher values and can therefore have a more refined binning (12-bit). Finally,
2430 a single 12-bit 2D histogram is included, with 6 bits for every axis. It is used as an
2431 online scatter plot for comparing one measured parameter to another. An example
2432 for it is a comparison of the width against the area, which can help the user determine
2433 the cuts that need to be applied to the measurement.

2434 5.8 Performance results

2435 The device has been tested in the lab using a pulse generator as well as several radioactive
2436 sources. The results show that: 1) the amplitude, area and width measurement
2437 are linear across all input ranges, 2) the highest rate of the PSA algorithm is $\sim 5 \times 10^6$
2438 pulses per second and 3) the lowest SNR where the algorithm still functions is ~ 5 .

2439 **Trigger rate** A pulse generator was used to verify the highest achievable rate at
2440 which the PSA still analyses every incoming pulse. The final state machine imple-
2441 mented in the pulse analysis module prevents the triggering block from issuing a
2442 trigger due to an incoming pulse if the previous analysis is still in ongoing. Given
2443 that all the pulses were of the same length, the analysis duration was always the
2444 same. When the time between the incoming pulses was shorter than the time of the
2445 analysis, the pulses were not analysed. Figure 5.12 shows the sharp decline in the
2446 percentage of the analysed pulses when reaching the rate of 5 MHz. Therefore the
2447 overall analysis duration for a 10 ns pulse is approximately 200 ns.

2448 **Linearity** A pulse generator was used to verify the linearity of the measurements
2449 across all input ranges. Pulse width and amplitude were varied and measured both
2450 with the oscilloscope and the PSA to check for non-linearities or inconsistencies in the
2451 PSA measurements. The resulting plots in figures ?? and 5.13c show that the PSA
2452 measurements agree well with those from the oscilloscope. The major inconsistency
2453 is observed in the lower range of the plots. It stems from the fact that the bandwidth
2454 limit of the PSA is lower than that of the oscilloscope, which affects the pulse shape.
2455 Effectively, the PSA cannot measure the rectangular pulses of the width smaller than
2456 2 ns.

2457 **Stability** The input pulse signal was superimposed with white noise generated by
2458 a noise generator with a variable gain. The mixed signal yielded pulses with an

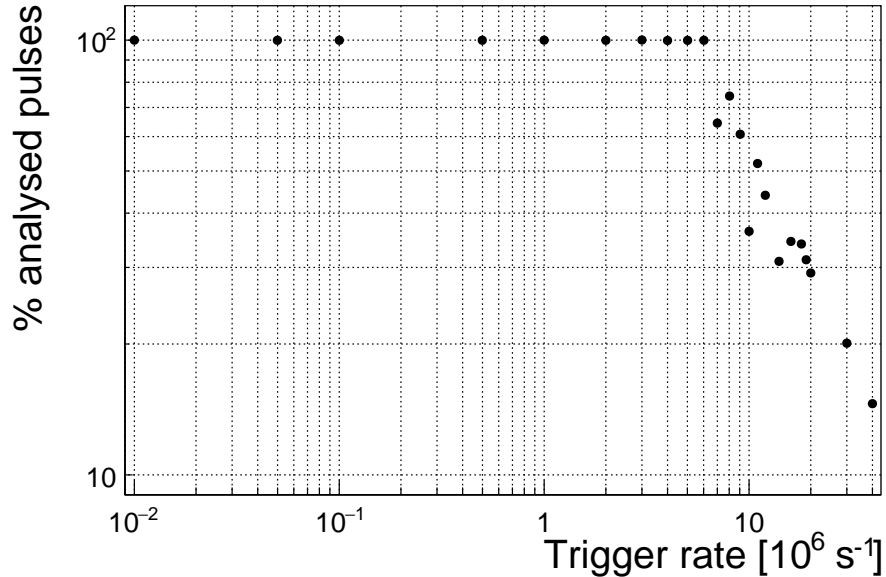


Figure 5.12: This figure shows the capability of the device to analyse all arriving pulses for a range of input frequencies. The highest achievable rate with zero lost pulses is $5 \times 10^6 \text{ s}^{-1}$.

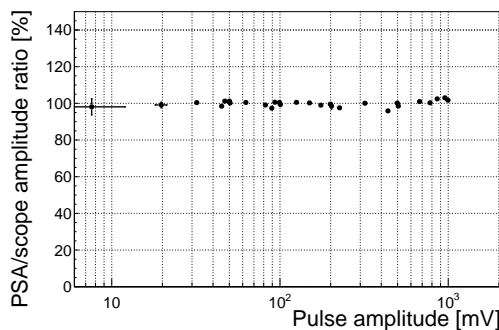
SNR ranging from 5 (very noisy) to 100 (noise negligible). The PSA then performed the pulse parametrisation at different SNRs. The resulting plots in figures 5.13b, 5.13d and 5.13e show that the pulse width measurement is stable even for low SNR whereas the amplitude measurement is affected significantly. This stems from the analysis taking the highest sample as the pulse's amplitude. The area measurement, being effectively the integrated amplitude across the pulse, is also affected by the faulty amplitude measurement. Nevertheless, the mean area remained the same. This means that the added noise only affects the resolution of the spectrum, not its position.

5.8.1 Comparison between the charge- and current-sensitive spectroscopy

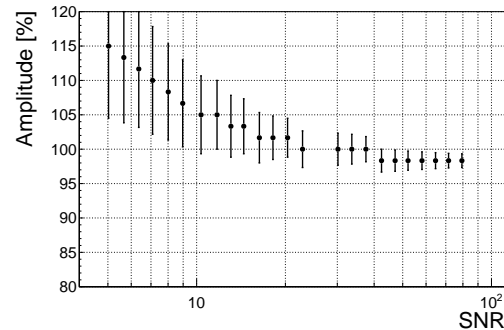
The calibration was done using a $^{148}\text{Gd}^{239}\text{Pu}^{241}\text{Am}^{244}\text{Cm}$ source which emits α particles with four different energies. The PSA in combination with the current amplifier was compared against the 8-bit spectroscopic application in combination with the charge amplifier and a commercial 14-bit spectroscopic readout.

The ^{241}Am peak measured by the Cx amplifier has an RMS of 0.8 ADC, which corresponds to a 32 keV energy resolution. For comparison, the C2 amplifier measures this peak with an RMS of 1.9 ADC, which corresponds to a 75 keV energy resolution. Therefore the energy spectrum measured by the current amplifier has a lower energy resolution.

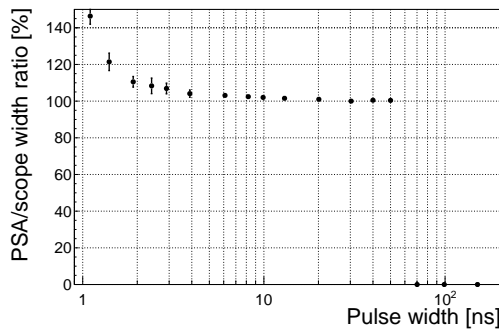
5.8. PERFORMANCE RESULTS



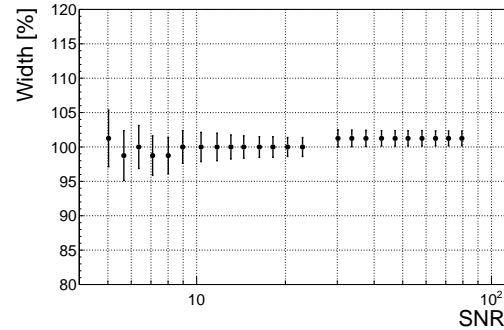
(a) Linearity across the amplitude range.



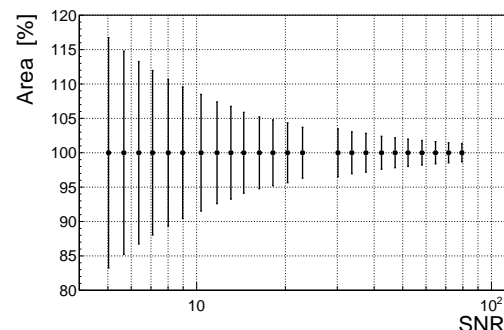
(b) Amplitude stability.



(c) Linearity across the width range.



(d) Width stability.



(e) Area stability.

Figure 5.13: These diagrams show the linearity of the measurements and their stability with respect to analog noise.

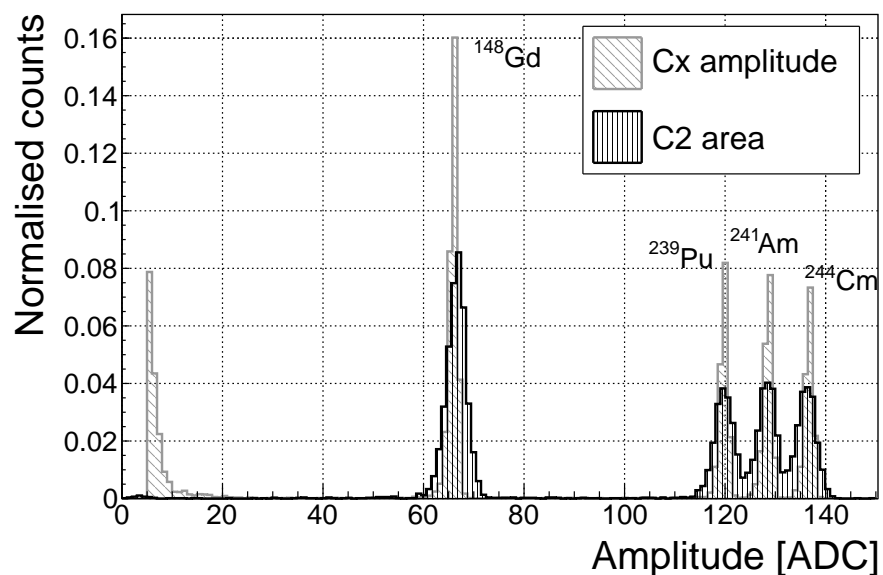


Figure 5.14: Spectrum of a $^{148}\text{Gd}^{239}\text{Pu}^{241}\text{Am}^{244}\text{Cm}$ source using a Cx and a C2 amplifier.

5.9. SOURCE CALIBRATION

2479 5.9 Source calibration

2480 The operation of the pulse shape analysis has been tested using several radioactive
 2481 sources. In particular, an α , a β and a γ source have been used. Each source has
 2482 been placed on top of the diamond detector and left for a predefined time depending
 2483 on its activity. Table 5.2 shows the sources used, the time of exposure and their rate
 2484 during this time. The data for the α source have been taken for both polarities. In
 2485 addition, a long run with an α source with a sheet of paper in between the source
 2486 and the diamond has been taken. The paper stops the α particles but lets through
 2487 the photons, which helps to estimate the background photon radiation of the source.

Run	Source	Radiation	Energy [MeV]	Time [h]	Triggers	Rate [s^{-1}]	Bias [V]
2488	1 $^{241}\text{Am}^*$	α	5.5	60	958	4.4e-3	500
	2 ^{241}Am	α	5.5	17	10558	0.17	500
	3 ^{241}Am	α	5.5	18	11454	0.18	-500
	4 ^{90}Sr	β	2.3	0.42	1.07e6	1000	500
	5 ^{60}Co	γ	1.3	0.28	1.34e6	3300	500
	6 $^{239}\text{Pu Be}$	n	1-10	2.5	1.5e6	230	500

2489 Table 5.2: Measurements carried out at Atominsttitut.

2490 The pulses acquired during the data taking are shown in persistence plots in
 2491 figures 5.15. Figure 5.15a showing the ^{241}Am source background reveals that the
 2492 diamond detector had been contaminated, probably with chipped-off grains of the
 2493 unsealed source. This stems from the fact that α pulses are recorded despite having
 2494 a sheet of paper, which stops all the particles emitted by the source. However, the
 2495 number of α hits due to contamination is negligible - an estimated 1 h^{-1} . Another
 2496 point worth noting is the falling slope of the rectangular pulse in figure 5.15c. This
 2497 stems from the space charge that had built up during the neutron irradiation and is
 2498 discussed in section ???. Finally, figure 5.15f shows that the neutron source causes
 2499 the widest variety of pulse shapes - triangular and rectangular as well as those in
 2500 between. Pulse shapes caused by neutrons are described in detail in [45, 44].

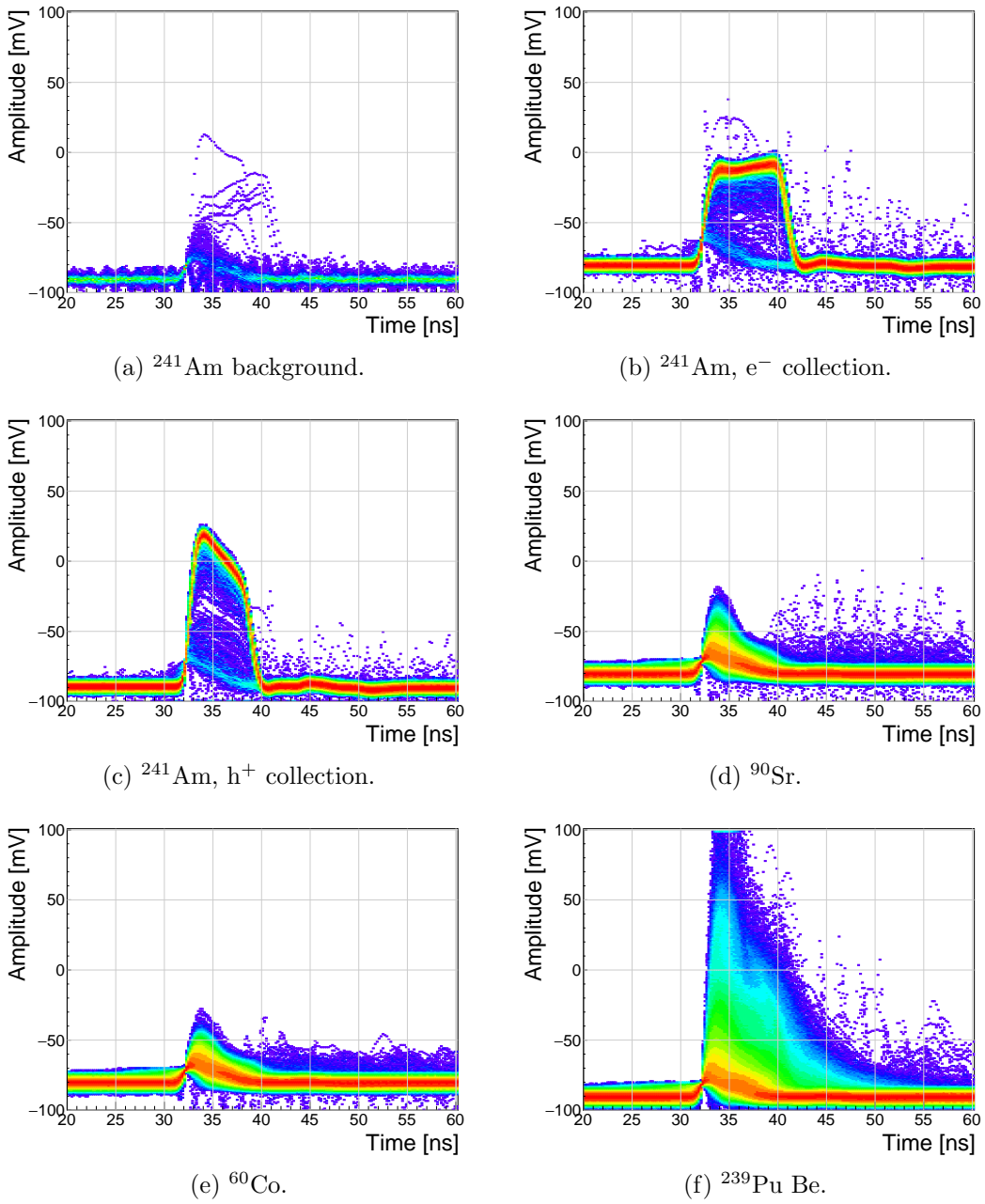


Figure 5.15: Accumulated pulses for all runs.

5.9. SOURCE CALIBRATION

5.9.1 Source measurements – scatter plots

An online pulse shape analysis has been run on all the above mentioned data sets. The parameters of the pulses are plotted in 2D histograms - in form of scatter plots. The aim is to find a way to distinguish between the various types of radiation in order to only select the spectrum of a single type of particles from a spectrum of a mixed source. The energy spectrum is directly proportional to the measured area of the current pulses, therefore all the parameters are plotted against the pulse area. The parameters used are:

- FWHM
- Base width
- Amplitude
- Amplitude × Base width
- Base width – FWHM
- Falling slope

Every individual parameter can be attributed a set of qualifiers with which a certain part of the distribution can be rejected. There are two ways to apply the qualifiers. One is to set the minimum and maximum value for a specific parameter. The accepted pulses are those in between these two values. The minimum and the maximum qualifier are marked with a blue and a red line in the subsequent scatter plots. The second way is to apply a linear cut to the distribution in the scatter plot. The user can choose the slope of the line and to accept either the pulses above or below the line. The colour of the line is blue if the part above the line is accepted and red if opposite. Currently two scatter plots have this option implemented: area vs amplitude and area vs amplitude×base width. The latter represents the Form Factor, which is discussed in section 5.6.2.

The sets of plots in figures 5.16, 5.17, 5.19 and 5.20 show the above listed parameters plotted against the pulse area for ^{241}Am background, electrons and holes, ^{90}Sr and ^{64}Co source, respectively. Any distinguishable difference between the plots of two sources would suggest that that particular parameter can be used to distinguish one type radiation from the other. For the most part the photons are considered the rejected pulses (greyscale colour palette) whereas α particles or neutrons are accepted (yellow colour palette). In special cases only a certain types of neutron interactions are accepted, as depicted in section 5.10.

5.9.1.1 ^{241}Am source

The source emits α particles at ~ 5.5 MeV and photons with a range of energies. Due to the losses in the air and the electrode the measured α energy varies – between ~ 5 MeV down to 1 MeV.

Figures 5.16 and 5.17 show the pulse area distribution with respect to the aforementioned parameters, for electrons and holes respectively. Focusing on the top left plot in figure 5.16, a distinctive horizontal stripe appears at a width of 9 ns, ranging from 100 up to 630 pVs. This is the aforementioned spread of α energies. The shape of the pulse from this type of radiation retains the width even at smaller energies. Only its amplitude is decreased. This is because the free charge carriers in the diamond are traveling with the same speed in all cases, inducing rectangular pulses of the same widths.

The other cluster in the [area, FWHM] phase space comes from the background photons. The two clusters are far apart from one another with no overlap. It is therefore straightforward to define a cut in the FWHM to distinguish between the α and γ entries. This is done by means of the minimum and maximum FWHM constant qualifier, which marked red and blue in the [area, FWHM] subfigure.

The [area, amplitude] subfigure also reveals two distinguishable clusters, which can be segregated using a linear qualifier. The angle of the α stripes in the [area, amplitude] subplots is significantly smaller than that of the photon stripe. The separation is much less pronounced in the other subfigures.

There is a third barely distinguishable island visible in the top two plots, both area and width values close to zero. This island is formed by noise, which triggered the analysis.

The situation is similar when inverting the bias voltage and collecting holes, as shown in figure 5.17. Here, however, the two clusters are much closer together even in the [area, FWHM] subfigure. This makes it more difficult to define a clear border between the two. The other five qualifiers are in this case less important than the FWHM. Nevertheless, it can be deduced from the plots that the difference BW-FWHM must be below 4 ns.

The slope is dependent of the amplitude, which can be seen in the bottom right plot, making it an unreliable qualifier in the lower area range. The amplitude, scaling with area, makes a distinguishable straight line in the middle left subfigure.

The amplitude increase with area in the [area, amplitude] subfigure is similar for photons and α particles. Therefore a linear qualifier can not be used to distinguish α radiation from γ radiation when measuring holes.

Figures 5.18a and 5.18b show a one-dimensional area distribution of the acquired data for electron and hole collection. The blue histogram represents all collected data whereas the red one marks the data whereby the pulse parameters are within the qualifiers. In both figures the α peak at 600 pVs is clearly visible, followed by a γ quasi-Landau distribution with an MPV of \sim 70 pVs and a noise peak at the very left of the area distribution. These two contributions have been rejected by the FWHM qualifier.

5.9. SOURCE CALIBRATION

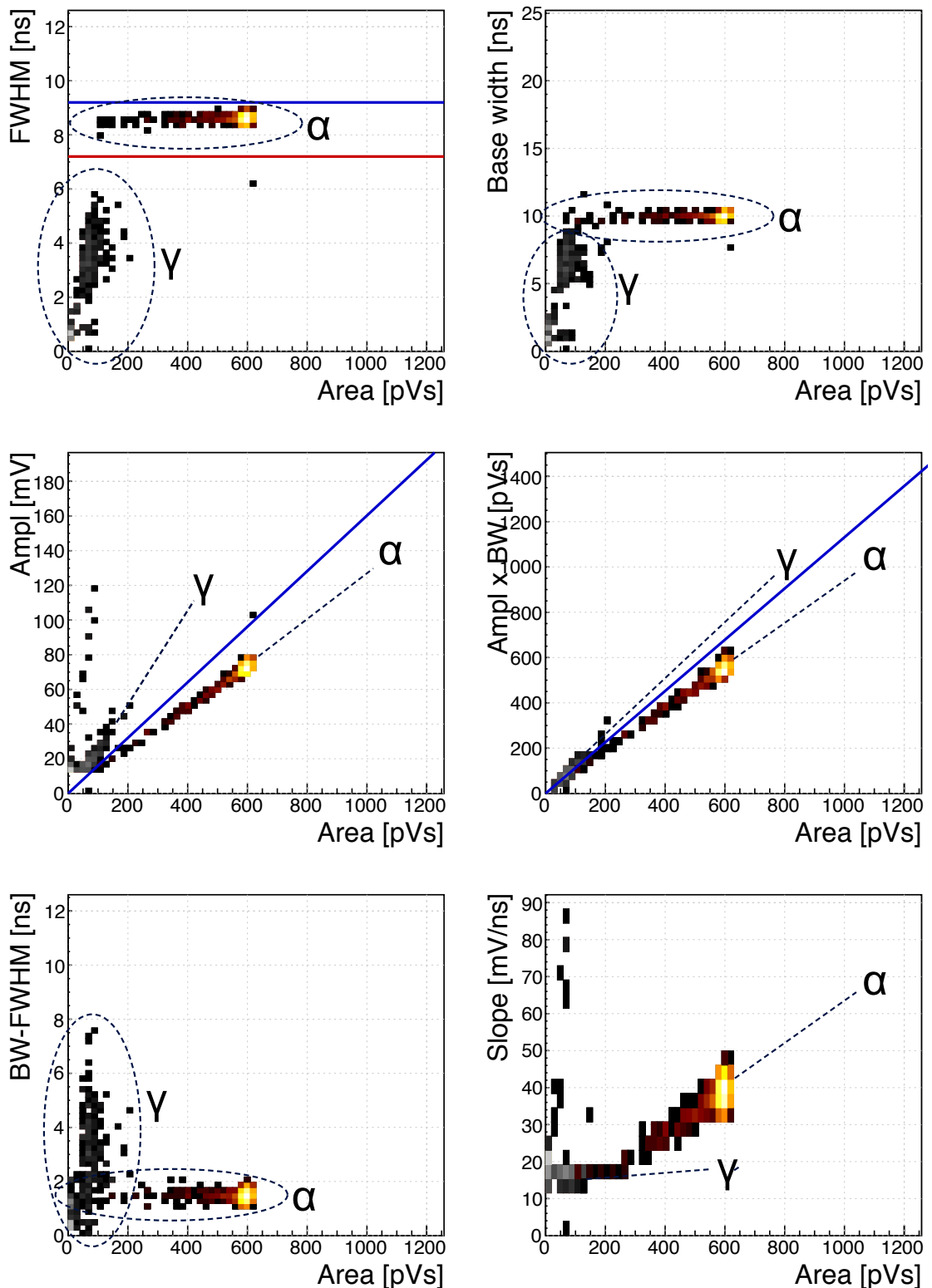


Figure 5.16: ^{241}Am , e^- collection. Qualifier: FWHM. Optional qualifiers: Amplitude, Form Factor.

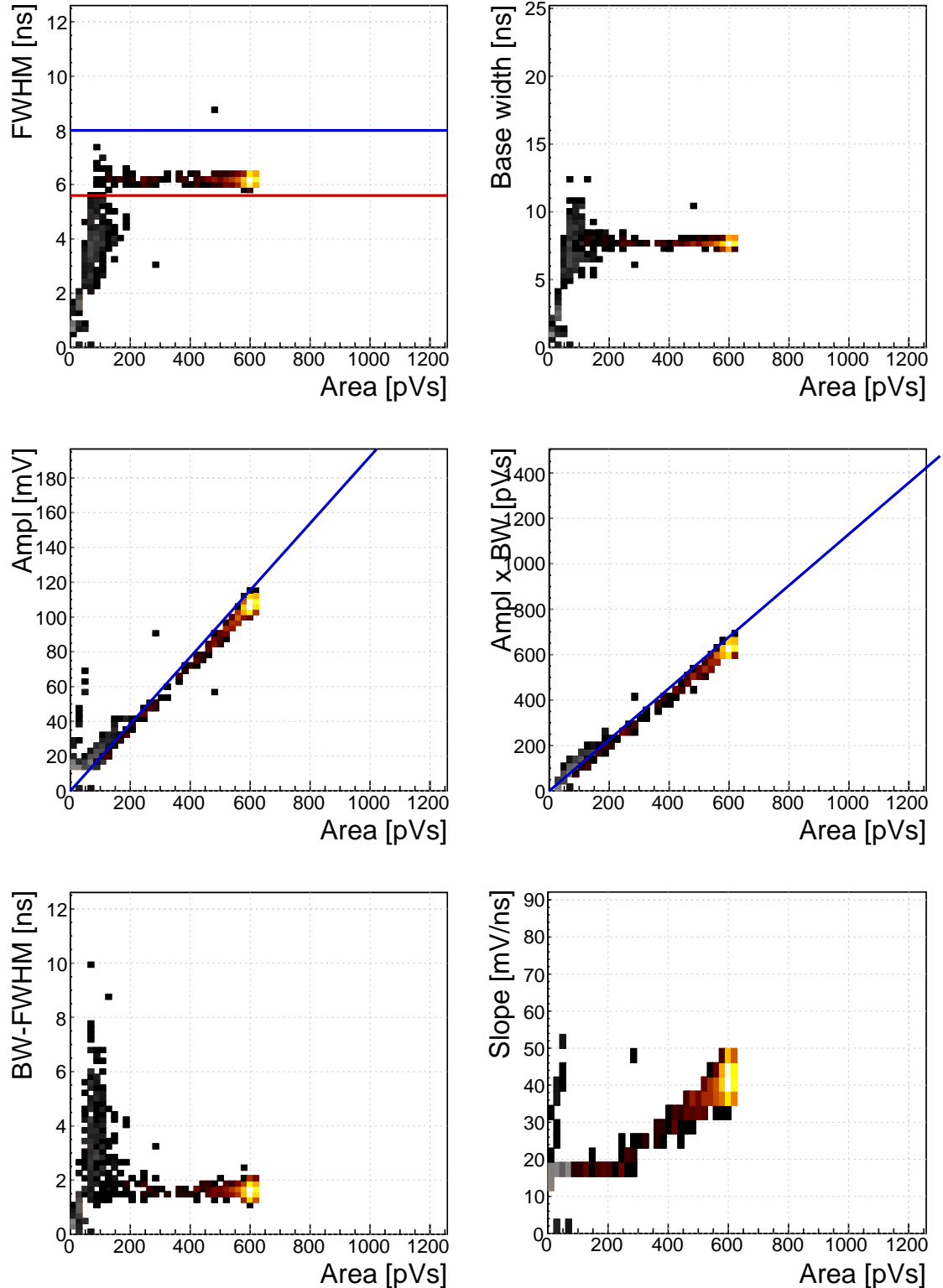
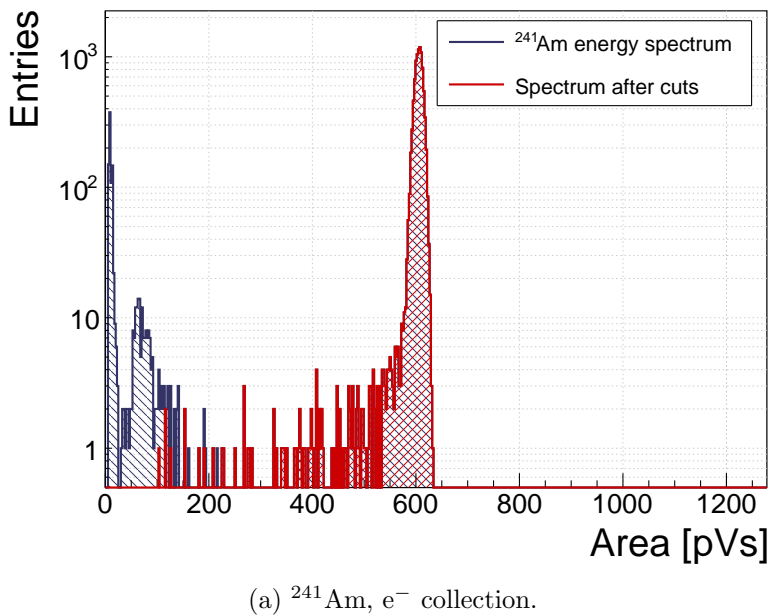
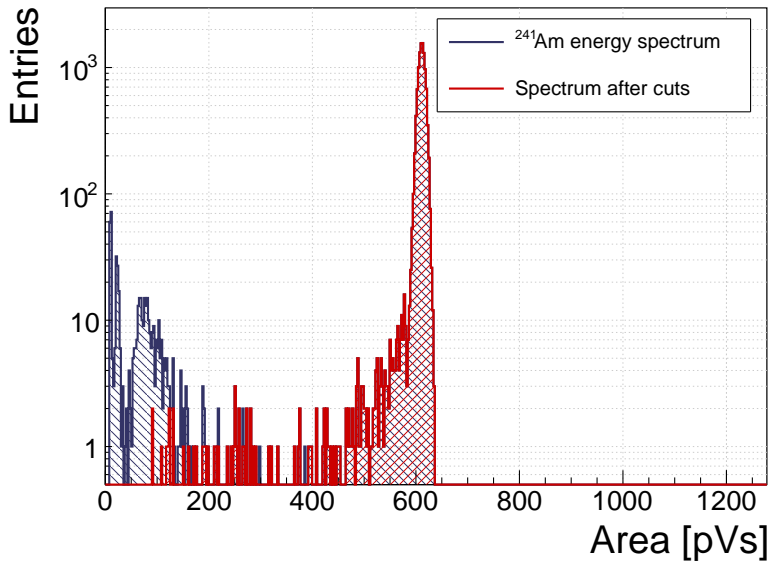


Figure 5.17: ^{241}Am , h^+ collection. Qualifier: FWHM.



(a) $^{241}\text{Am}, e^-$ collection.



(b) $^{241}\text{Am}, h^+$ collection.

Figure 5.18: ^{241}Am area histograms for electron and hole collection.

2577 **5.9.1.2 ^{90}Sr and ^{60}Co source**

2578 The phase space of the ^{90}Sr source overlaps entirely with that of the ^{60}Co source, as
2579 results from figures 5.19 and 5.20. This renders it virtually impossible to distinguish
2580 between photons and electrons (MIPs). Comparing the [area, FWHM] phase space
2581 of the photons and alphas and the high reach of the former, the electron collection of
2582 the alphas would need to be used to distinguish between the two types of particles.

2583 The one-dimensional histograms in figure 5.21 show a quasi-Landau distribution
2584 with the MPV at ~ 70 pVs, which is in agreement with the background γ radiation
2585 emitted by the ^{241}Am source, as shown in figure 5.18 in the previous subsection. This
2586 is however not a pure Landau distribution. Relative to the 600 pVs α peak, the ex-
2587 pected MPV of MIPs would be ~ 30 pVs, which is not the case in these distributions.
2588 This is because the PSA device is a self-triggering system, which cuts the lower ener-
2589 getic particles with the trigger threshold. The resulting distribution is therefore only
2590 the top portion of the real Landau distribution. Unfortunately this is the limitation
2591 of the device, governed by the analog noise of the current pre-amplifier.

5.9. SOURCE CALIBRATION

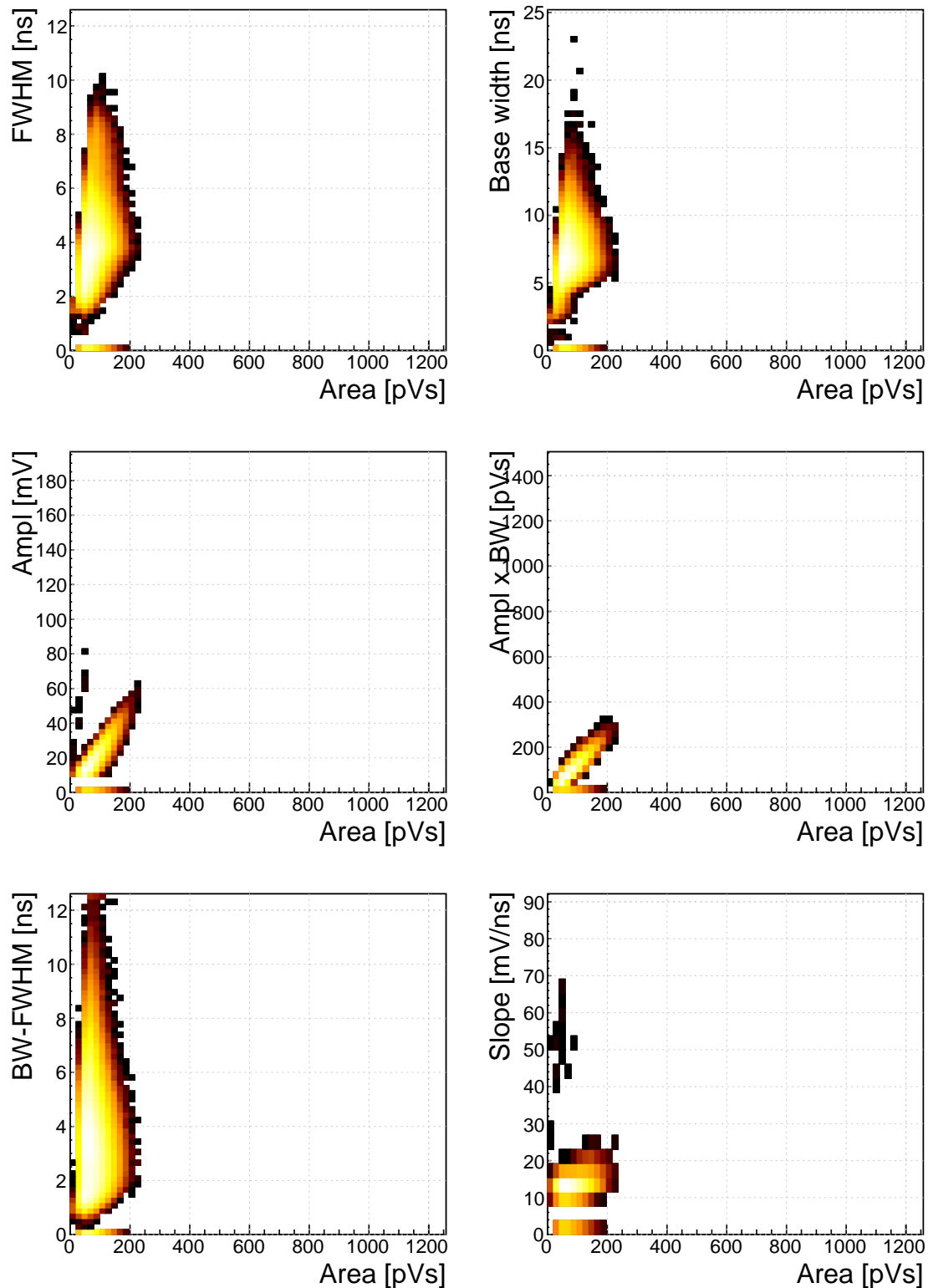


Figure 5.19: ^{90}Sr scatter plots.

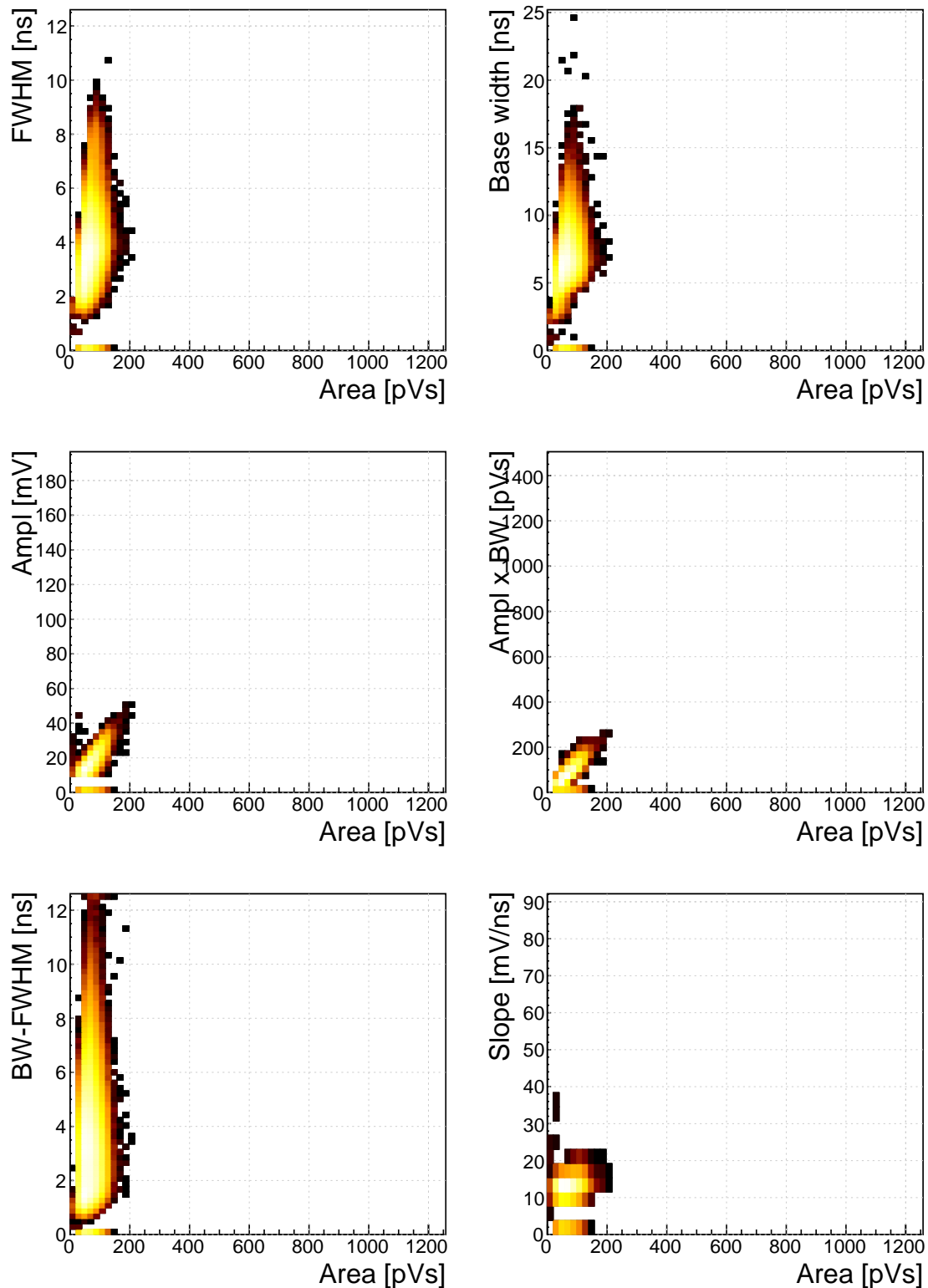


Figure 5.20: ^{60}Co scatter plots.

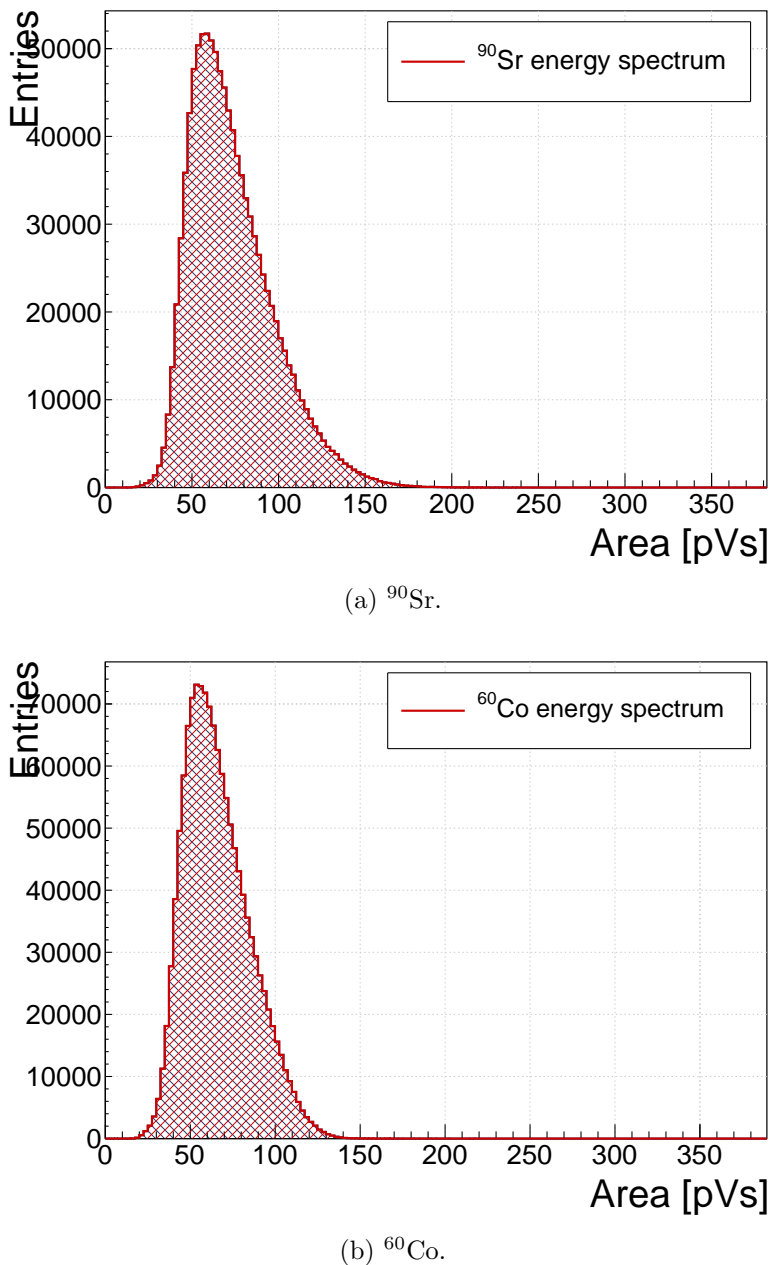


Figure 5.21: Energy distributions for γ and β particles.

5.10 Applications in neutron instrumentation

The real-time pulse shape analysis procedure can be applied to more complex systems.
This section includes three applications where the PSA has been applied.

Semiconductor-based neutron detectors provide a compact technology for neutron detection. However, the cross section of a neutron with the diamond bulk is very low, since it only interacts with the core of the atom. Diamond is mainly used to detect charged particles and photons.

Research neutron reactors radiate a mix of particles, apart from neutrons also photons. The photons are considered a background radiation, concealing the neutron spectrum. When measured with diamond, the signal from neutrons is difficult to distinguish from the photon spectrum. In addition, low energy neutrons do not cause nuclear reactions in the bulk. All in all, the neutron measurements in a reactor present a challenge with diamond. However, by means of the PSA, the neutron signal can be discriminated from the photon background to some extent. The following two cases show how measurements of fast (n^+) and thermal (n^-) neutrons have been carried out by making use of the PSA.

Note the changing scale on the X axis in the figures.

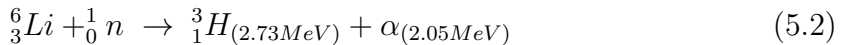
5.10.1 Thermal neutron flux monitoring

Research neutron reactors like TRIGA MARK II [?] at Atominstitut [?] in Vienna are capable of emitting neutrons at a wide range of energies. The neutron flux is proportional to the current power of the reactor. It is therefore instrumental to monitor the neutron flux to make sure that the reactor operation is within the specified limits. However, the byproduct of the radioactive decays in the core is γ radiation, which has an energy range that overlaps with that of neutrons, making it difficult to measure the neutron flux. This is where PSA and diamond detectors come into play. This section describes the application of thermal neutron flux monitoring by means of the PSA.

Thermal neutrons do not interact with the diamond bulk due to their low kinetic energy (of the order of 0.012 eV). Hence a converter foil has to be added to produce second order effects. Incoming neutrons interact with the foil, producing a set of secondary particles. These can then be detected upon hitting the detector bulk. Common neutron interactions that are used in thermal neutron detection are $^{10}\text{B}(n,\alpha)^7\text{Li}$ reaction and $^6\text{Li}(n,\alpha)^3\text{H}$ reaction (α stands for ^4_2He , see equation 5.2). The focus in this section is on the latter. With a foil installed, there are several possibilities for neutrons to interact with the detector system. Each of these interactions ionises the diamond bulk in its own way, resulting in a specific shape of the current pulse. A neutron can: 1) interact with the foil, producing an α and a ^3H , 2) interact with a carbon atom in the lattice, producing an α and a γ or even three α . The thermal neutrons do not have enough kinetic energy to interact with the lattice,

5.10. APPLICATIONS IN NEUTRON INSTRUMENTATION

2631 therefore the focus is on case (1). The equation for this reaction is the following:



2632 The particles in the first case are produced outside the diamond and get stopped
2633 immediately upon hitting the sensor. The resulting pulses for both particles have a
2634 rectangular shape of the same width, because the carriers drift with the same speed
2635 in both cases. The difference is in the number of free carriers produced - the tritium
2636 creates more (proportional to the deposited energy), which in turn induces a higher
2637 pulse.

2638 TRIGA MARK II neutron reactor emits large amounts of γ radiation in the
2639 energy range up to 3 MeV. This already affects the measurements of α particles, the
2640 energy of which peaks at 2.05 MeV in the case of 6Li converter foil. However, γ
2641 background radiation can be suppressed by discriminating current pulses of photons
2642 from those induced by α particles. This idea has already been implemented in offline
2643 analysis in [29, 23]. The results show that the background photons can be subtracted
2644 successfully. In order to make sure that every single incident thermal neutron has
2645 been accounted for, the algorithm has been ported to FPGA where it detects and
2646 analyses particles in real time.

2647 5.10.1.1 Measurements

2648 ROSY readout device with the implemented Pulse Shape Analysis was put to a test
2649 at Atominstut in Vienna. Their TRIGA neutron reactor is capable of delivering
2650 thermal neutrons with the energy 0.012 eV at a rate of $10^3 \text{ n cm}^{-2} \text{ s}^{-1}$, with a
2651 considerable γ background.

2652 First, the device was calibrated using an unsealed monochromatic ${}^{241}Am$ source
2653 with the emitted particle energy $E_\alpha = 5.12MeV$ (taking into account the losses in
2654 the air). Then the diamond detector was exposed to the beam. Secondary reaction
2655 products (α and 3H particles), created by neutrons hitting the converter foil, were
2656 detected by the diamond sensor, together with a significant photon background. Then
2657 the pulse identification algorithm was applied to discriminate between the reaction
2658 products and the photons.

2659 The main parts of the detector are an sCVD diamond sensor sized $4.7 \times 4.7 \text{ cm}^2$
2660 and a $1.8 \mu\text{m}$ thick LiF converter foil, both embedded in an RF-tight PCB. The
2661 diamond sensor is biased with a bias voltage of $1 \text{ V}/\mu\text{m}$ and capacitively coupled to
2662 CIVIDEC's C2 40 dB wide bandwidth current preamplifier. A 5 m long BNC cable
2663 connects the preamplifier to CIVIDEC ROSY box. The detector assembly together
2664 with the preamplifier has to be placed in front of an exit hole of the reactor.

2665 Note: this data set has been taken with an older version of the firmware, which
2666 only measured a limited number of pulse parameters.

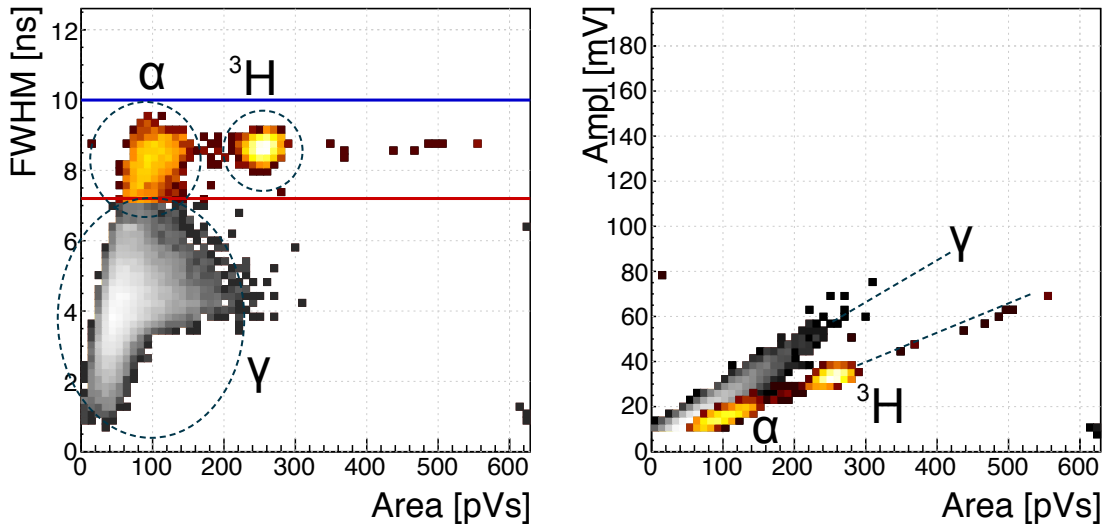


Figure 5.22: Thermal neutrons, photons. Qualifier: FWHM.

2667 5.10.1.2 Results and discussion

2668 The data collected by the PSA show a high flux of photons, which covers a wide area
 2669 range. The ^3He peak is clearly visible and has almost no overlap with the photon
 2670 cluster. The α cluster has a much lower energy and is in the same energy range as
 2671 the photons. However, if a FWHM parameter is observed, a distinction between the
 2672 photons and the α can be seen. By setting a qualifier to the right value, the photon
 2673 background is cut away, leaving only the thermal neutron decay products in the data
 2674 set, as shown in figure 5.22. The resulting one-dimensional area histogram before and
 2675 after applied cuts is shown in figure 5.23. The blue distribution is the mixed field
 2676 of background photons, tritium and α particles. The latter are completely hidden in
 2677 the γ energy distribution. After applied qualifiers the α peak suddenly appears.

2678 5.10.1.3 Conclusion

2679 By applying the FWHM qualifier to the acquired data from the TRIGA neutron reactor,
 2680 the α and tritium particles can be identified and separated from the γ background.
 2681 The resulting cleaned data can be used to correctly count the thermal neutrons de-
 2682 tected by the diamond sensor.

2683 5.10.2 Fusion power monitoring

2684 Many research collaborations around the world are trying to develop a functional
 2685 fusion reactor, which could provide a cleaner energy source. One of them is ITER [7],
 2686 a research fusion reactor being built in France. The idea behind it is to harvest
 2687 energy from the fusion of light atoms into a heavier one. For ITER the fuel chosen

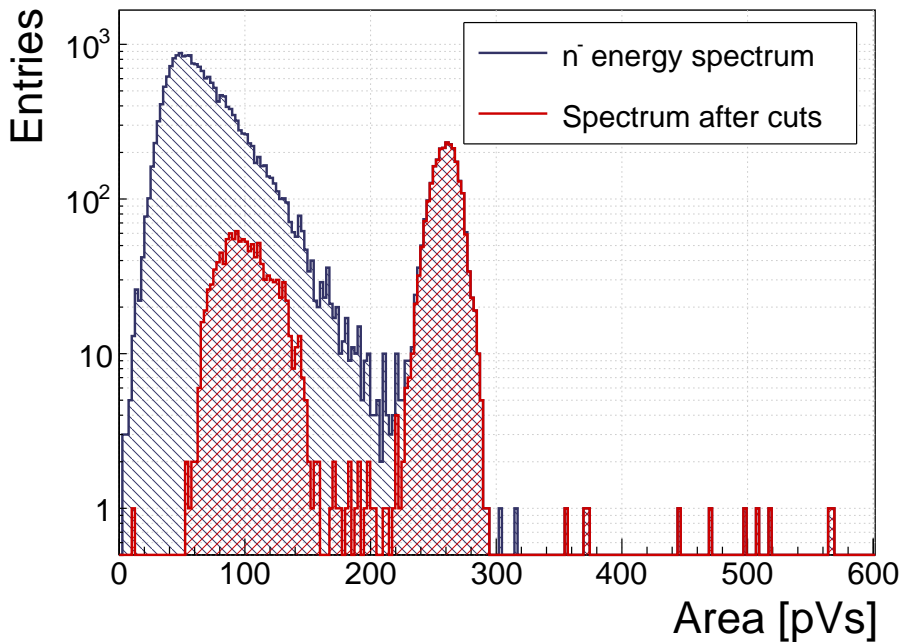
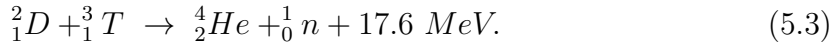


Figure 5.23: Energy spectrum after applied qualifiers reveals the tritium and α peak

2688 is a mixture of deuterium and tritium, which fuse into a helium atom at extremely
 2689 high temperatures (plasma), emitting a highly energetic neutron as a byproduct. The
 2690 equation is the following:



2691 The α particle immediately deposits its energy within the plasma. The neutron, due
 2692 to its neutral charge, continues its way out of the system where it is stopped. The
 2693 stopping power is converted into energy, which heats the water into steam, which in
 2694 turn spins the turbines, generating electricity.

2695 It is possible to monitor the activity of the reactor by measuring the flux of neu-
 2696 trons emitted. Neutron diagnostics such as neutron cameras, neutron spectrometers
 2697 and neutron flux monitors therefore provide robust measurements of fusion power. A
 2698 high γ background makes it difficult to accurately measure the neutron flux. This is
 2699 a motivation to use a diamond based detector with a real-time PSA algorithm.

2700 The neutrons emitted are 14 MeV mono-energetic fast neutrons. The most ac-
 2701 curate and efficient way to detect them with a diamond detector is by means of a
 2702 $C_{12}(n,\alpha)$ reaction with a carbon atom in the ballistic centre [30]. In this region the
 2703 positive and negative charge carriers created by α that start drifting in the opposite
 2704 directions need the same time to reach the opposite electrodes.

2705 **5.10.2.1 Measurements**

2706 The ${}^{239}\text{Pu Be}$ neutron source has been used to simulate the fusion reactor. It emits a
 2707 mixed field of neutrons and photons with a wide range of energies. The neutrons are

rarely detected with diamond – the interactions happen mostly in the electrodes on either side of the detector. The α particles created by the interactions are detected by the diamond. Depending on the side of the interaction, the created pulse is either due to hole– or electron collection. These two interactions make the two distinct lines in the [area, FWHM] phase space at 9 ns and 6 ns, as shown in figure 5.24, top left plot.

A very interesting interaction point is the ballistic centre [?] of the diamond. A ballistic centre is the position from which it takes the holes and the electrons the same amount of time to drift to the opposite electrodes. In this case the shortest possible pulse is created. Conversely, to conserve the collected charge and thus the pulse area, the pulse amplitude must be the highest at the ballistic centre. The entries in between are created by neutron interactions at random positions in the diamond, which produce pulses of various shapes.

5.10.2.2 Results and discussion

Coming back to the motivation, the most efficient way of counting the 14 MeV neutrons is through the measurement of the neutrons interacting in the ballistic centre [?]. To extract this type of interaction several qualifiers must be used. The first possibility is the FWHM set to 3–5 ns. However, this time the cuts on the [area, amplitude] and the [area, amplitude \times base value] phase space are preferred. First, a minimum constant amplitude qualifier is set to 22 mV, as shown in figure 5.24, middle left plot. Then a linear amplitude qualifier is set such that only the pulses with the highest amplitude for every area value are taken. This ensures that the high pulses from the ballistic centre are chosen. Second, a maximum linear amplitude \times base value qualifier is set such that only the pulses bearing the closest resemblance to a rectangle are chosen, as shown in figure 5.24, middle right plot. In this phase space the entries at the bottom of the distribution are bearing more resemblance to a rectangle whereas those at the top are more akin to triangles.

The resulting [area, FWHM] subfigure after applied qualifiers highlights the entries with a FWHM of 4 ns, which is the width of the pulses induced by neutrons interacting in the ballistic centre. This proves that these combined qualifiers indeed pinpoint these neutron interactions. The final one-dimensional area/energy distribution of the neutrons interacting in the ballistic centre is shown in figure 5.25.

The result could be further improved by further constraining the identification, e.g to define the minimum FWHM constant qualifier and the minimum slope constant qualifier.

5.10.2.3 Conclusion

By applying the appropriate qualifiers to the data, the neutron interactions in the ballistic centre can be identified.

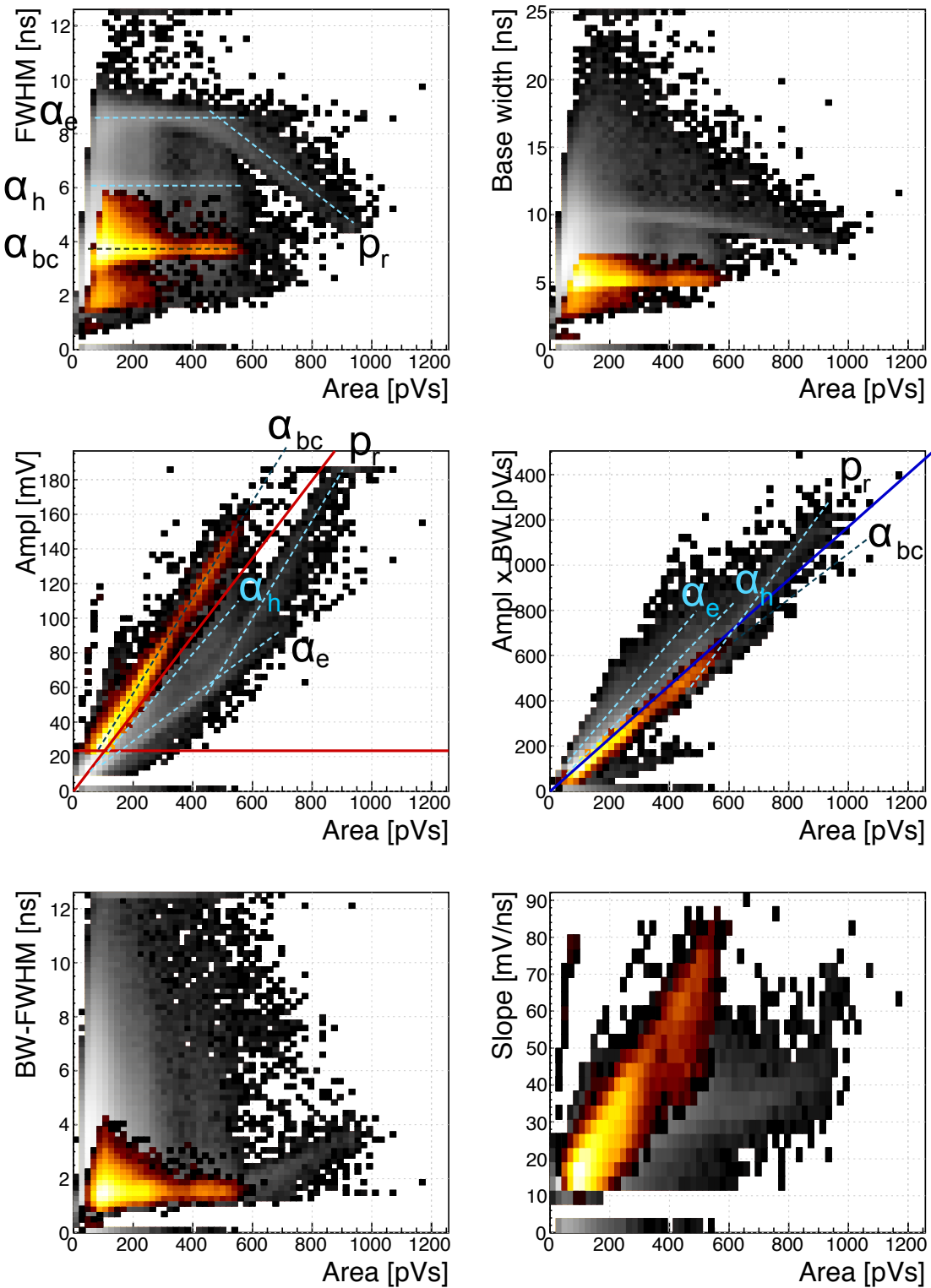


Figure 5.24: $^{239}\text{Pu Be}$. Qualifiers: BW-FWHM, FWHM, Form Factor

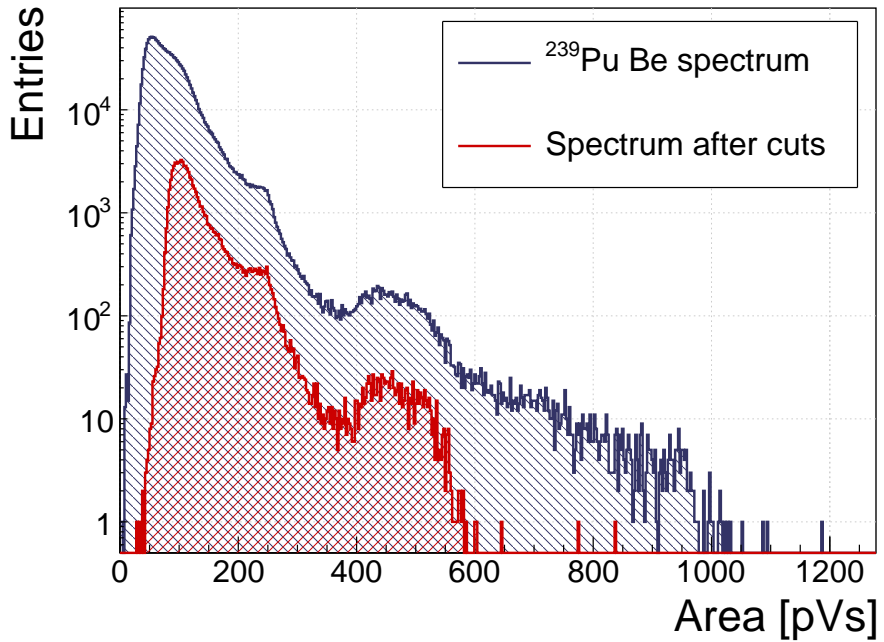


Figure 5.25: ^{239}Pu Be, energy distribution of the neutrons interacting in the ballistic centre.

2746 5.10.3 Fast and thermal neutron monitoring

2747 The CROCUS reactor at EPFL [2] is a research neutron reactor. The research group
2748 working on the reactor is interested in measuring neutrons with energies between
2749 1–2 MeV, which is overlapping with the γ background energy range.

2750 The highest output power of the CROCUS reactor is 100 W. Currently there
2751 are fission chambers that carry out the neutron counting, which is a measure of the
2752 activity of the reactor. The new goal is to measure both neutrons and photons,
2753 but separately. The pulse shape analysis is a good solution for this task. For this, a
2754 400 μm thick diamond detector with a specially designed casing was added to measure
2755 the activity. The LiF foil was added for conversion of thermal neutrons. The ROSY
2756 box with the integrated PSA routine was used for signal analysis.

2757 5.10.3.1 Measurements

2758 At the highest reactor activity the system counts particles at a rate of $\sim 1.5 \times 10^5 \text{ s}^{-1}$.
2759 The results from a test run at 10 W output power are shown in figure 5.26. The data
2760 include a mixed field consisting of fast neutrons, photons and of α and ^3H particles
2761 as products of thermal neutron decay in the LiF foil in front of the detector. The
2762 energy deposited in the diamond is not as high as that from the ^{239}Pu Be source.
2763 In addition, the analog noise during this measurement is higher than in the previous
2764 application. These conditions combined make particle identification at CROCUS a
2765 challenging task.

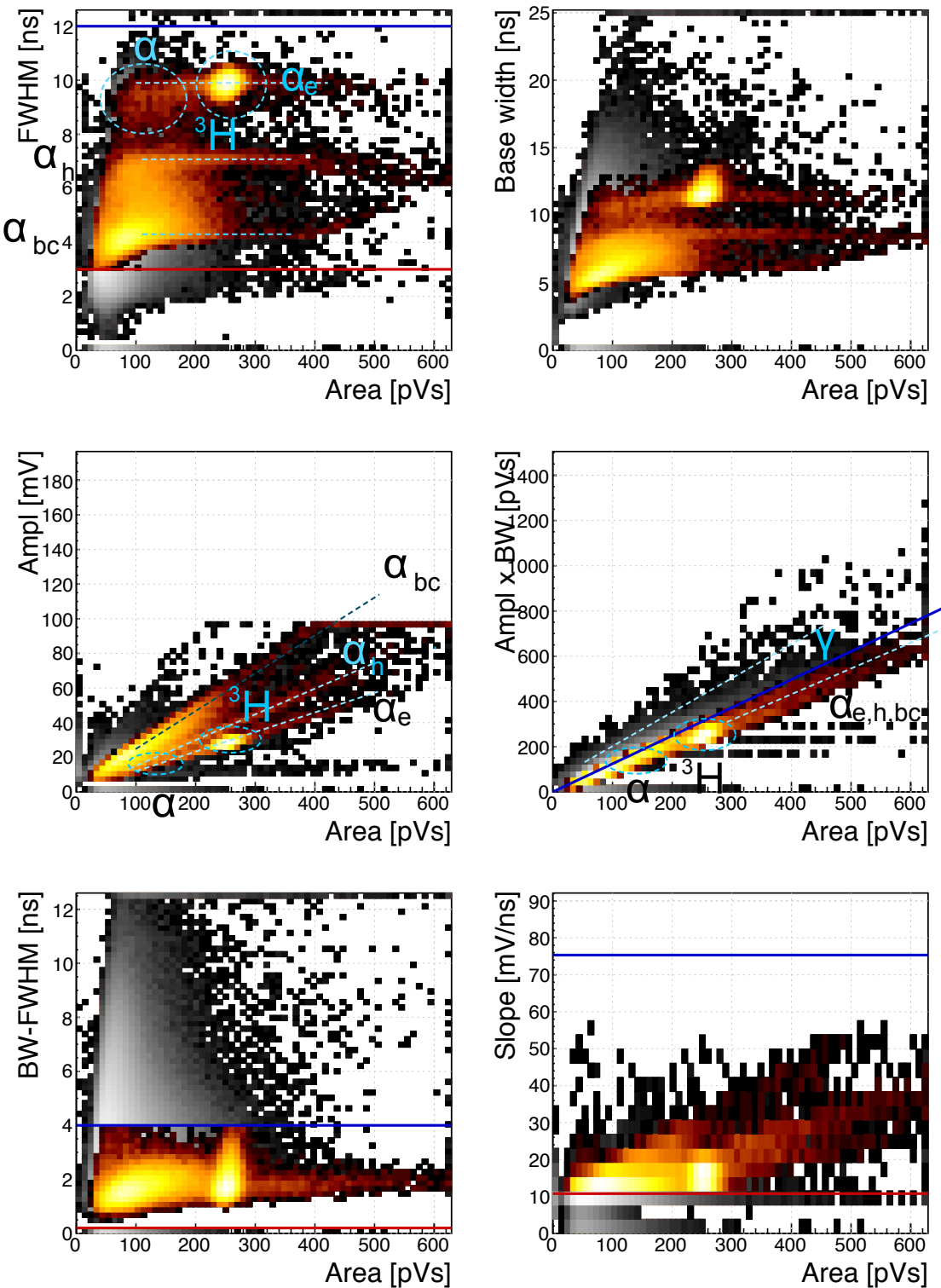


Figure 5.26: Fast neutrons, thermal neutrons, photons. Qualifiers: BW-FWHM, FWHM, Form factor, Slope.

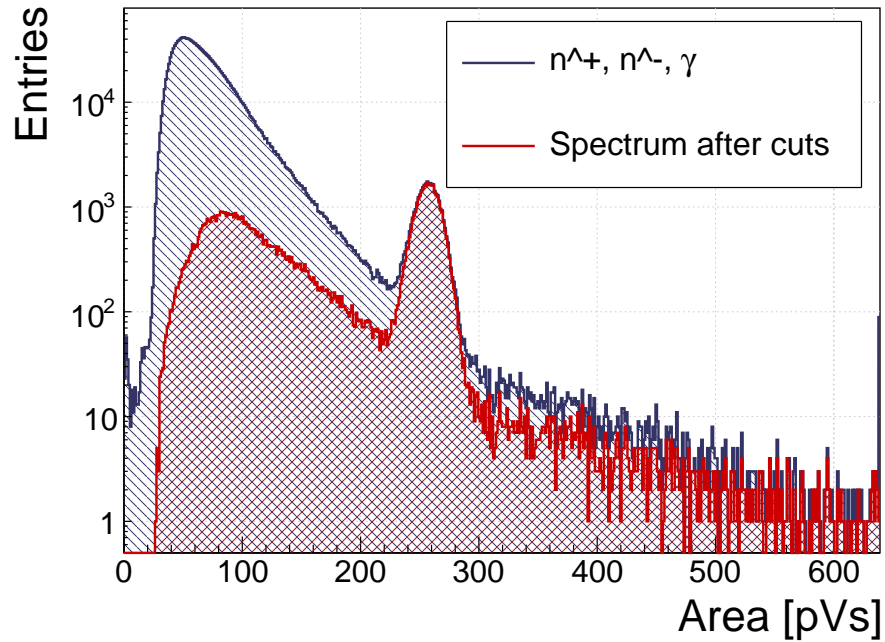


Figure 5.27: Energy spectrum in CROCUS before and after applied qualifiers

2766 **5.10.3.2 Results and discussion**

2767 The aim of this exercise is to identify both thermal and fast neutrons. For this the
2768 main qualifier used is the Form Factor - the linear line in the [area, amplitude×base
2769 value] phase space. Additional FWHM, FWHM-BW and slope constant qualifiers are
2770 used to clean the outlying entries. The resulting accepted entries in figure 5.26 have
2771 the distinctive three-line fast neutron signature in the [area, FWHM] subfigure with
2772 two superimposed islands by the α and ${}^3\text{H}$ cluster produced by thermal neutrons in the
2773 LiF foil. The γ background is sufficiently suppressed. The resulting one-dimensional
2774 histogram of the area/energy distribution is shown in figure 5.27.

2775 **5.10.3.3 Conclusion**

2776 By applying the Form Factor qualifier both fast and thermal neutrons can be identi-
2777 fied, suppressing the γ background.

2778 **5.11 Conclusion**

2779 This chapter describes a system that can identify the type of radiation in real time.
2780 The system is implemented on an FPGA in a CIVIDEC ROSY box and is used with
2781 diamond detectors. The signal from the diamond sensor is read in and analysed in the
2782 firmware. First the shape of the pulse is parametrised. Then the logic determines the
2783 type of particle according to the user defined cuts. Finally the parameters are written
2784 into a histogram, which is read out by the user. The firmware is designed to carry
2785 out the pulse shape analysis of a single pulse in ~ 200 ns, yielding a maximum pulse
2786 rate of 5×10^6 particles per second. The rate as well as the linearity the measurement
2787 stability with respect to noise have been verified using a pulse generator. Then several
2788 radioactive sources were used to calibrate the device. Finally the system has been set
2789 up in two neutron reactors to test the operation in a mixed field containing thermal
2790 neutrons, fast neutrons and photons. The identification can be optimised using a
2791 combination of qualifiers to achieve the desired effect.

₂₇₉₂

Bibliography

- ₂₇₉₃ [1] *Atominstut, Technical University of Vienna, Austria.*
₂₇₉₄ <http://ati.tuwien.ac.at/startpage/EN/>.
- ₂₇₉₅ [2] *CROCUS neutron reactor.* <http://lrs.epfl.ch/page-55655-en.html>.
- ₂₇₉₆ [3] *DRS4.* <https://www.psi.ch/drs/evaluation-board>.
- ₂₇₉₇ [4] *Element Six.* <http://www.e6.com>.
- ₂₇₉₈ [5] *European Centre for Nuclear Research, CERN.* <http://home.cern>.
- ₂₇₉₉ [6] *IHa Technologies Pte. Ltd.* <https://www.2atechnologies.com>.
- ₂₈₀₀ [7] *ITER fusion reactor.* <https://www.iter.org/>.
- ₂₈₀₁ [8] *Neutron Time-of-flight experiment.* <https://ntof-exp.web.cern.ch/ntof-exp/>.
- ₂₈₀₂ [9] *Paul Scherrer Institute.* <https://www.psi.ch/>.
- ₂₈₀₃ [10] *RD42 collaboration.* <http://rd42.web.cern.ch/rd42/>.
- ₂₈₀₄ [11] *TRIGA MARK II neutron reactor.* <http://ati.tuwien.ac.at/reactor/EN/>.
- ₂₈₀₅ [12] *Xilinx Virtex 5 FPGA.* <http://www.hdl.co.jp/XCM-109/top.560.jpg>.
- ₂₈₀₆ [13] *Determination of operational dose equivalent quantities for neutrons.* ICRU,
₂₈₀₇ Washington, DC, 2001.
- ₂₈₀₈ [14] General Atomics. *View of the TRIGA reactor.* 2015.
- ₂₈₀₉ [15] H. Bethe and J. Ashkin. *Experimental Nuclear Physics, ed. E. Segre*, page 253,
₂₈₁₀ 1953.
- ₂₈₁₁ [16] W. Blum, W. Riegler, and L. Rolandi. Particle Detection with Drift Chambers,
₂₈₁₂ volume 2 of 2. Springer-Verlag, Berlin Heidelberg, 2008.
- ₂₈₁₃ [17] Giorgio Brianti. SPS North Experimental Area. Technical Report CERN-SPSC-
₂₈₁₄ T-73-8. LabII-EA-Note-73-4, CERN, Geneva, 1973.
- ₂₈₁₅ [18] Maximilien Brice. *View of the nTOF detector.* Oct 2010.

BIBLIOGRAPHY

- 2816 [19] Maximilien Brice. *LHC tunnel*. Jan 2011.
- 2817 [20] Daniel Dominguez. *Standard Model. Le modele standard*. General Photo, Mar
2818 2015.
- 2819 [21] M. Garcia-Sciveres. ATLAS Experiment Pixel Detector Upgrades. 2011.
- 2820 [22] CIVIDEC Instrumentation GmbH. *sCVD diamond sensor*.
2821 <http://www.cividec.at>, 2015.
- 2822 [23] E. Griesmayer, R. Bergmann, H. Böck, M. Cagnazzo, P. Kavrigin, B. Mor-
2823 genbesser, and M. Villa. *A Novel Neutron Flux Monitor Based On Diamond*
2824 *Detectors at the Vienna TRIGA Mark II Reactor. submitted to the proceedings*
2825 *of ICRR 2015*, 2015.
- 2826 [24] E. Griesmayer and B. Dehning. Diamonds for beam instrumentation. *Physics*
2827 *Procedia*, 37:1997 – 2004, 2012. Proceedings of the 2nd International Conference
2828 on Technology and Instrumentation in Particle Physics (TIPP 2011).
- 2829 [25] Moritz Guthoff, Wim de Boer, and Steffen Mller. Simulation of beam induced
2830 lattice defects of diamond detectors using {FLUKA}. *Nuclear Instruments and*
2831 *Methods in Physics Research Section A: Accelerators, Spectrometers, Detectors*
2832 *and Associated Equipment*, 735:223 – 228, 2014.
- 2833 [26] M. Huhtinen. Simulation of non-ionising energy loss and defect formation in
2834 silicon. *Nuclear Instruments and Methods in Physics Research A*, 491:194–215,
2835 September 2002.
- 2836 [27] Hendrik Jansen, Daniel Dobos, Thomas Eisel, Heinz Pernegger, Vladimir
2837 Eremin, and Norbert Wermes. Temperature dependence of charge carrier mo-
2838 bility in single-crystal chemical vapour deposition diamond. *Journal of Applied*
2839 *Physics*, 113(17), 2013.
- 2840 [28] Hendrik Jansen, Norbert Wermes, and Heinz Pernegger. *Chemical Vapour De-*
2841 *position Diamond - Charge Carrier Movement at Low Temperatures and Use in*
2842 *Time-Critical Applications*. PhD thesis, Bonn U., Sep 2013. Presented 10 Dec
2843 2013.
- 2844 [29] P. Kavrigin, P. Finocchiaro, E. Griesmayer, E. Jericha, A. Pappalardo, and
2845 C. Weiss. *Pulse-shape analysis for gamma background rejection in thermal neu-*
2846 *tron radiation using CVD diamond detectors*. *Nuclear Instruments and Methods*
2847 *in Physics Research A*, (795), 2015.
- 2848 [30] P. Kavrigin, E. Griesmayer, F. Belloni, A.J.M. Plompen, P. Schillebeeckx, and
2849 C. Weiss. $^{13}C(n,\alpha_0)^{10}Be$ cross section measurement with sCVD diamond detec-
2850 tor. *submitted to EPJA*, 2016.

BIBLIOGRAPHY

- [31] Claude A. Klein. Radiation-induced energy levels in silicon. *Journal of Applied Physics*, 30(8):1222–1231, 1959.
- [32] Gregor Kramberger, V. Cindro, A. Gorisek, I. Mandic, M. Mikuz, and M. Zavrtanik. Effects of bias voltage during priming on operation of diamond detectors. *PoS*, Vertex2012:013, 2013.
- [33] W. Y. Liang. Excitons. *Physics Education*, 5:226–228, July 1970.
- [34] Claudia Marcelloni De Oliveira. *IBL installation into the inner detector of the ATLAS Experiment side C*. General Photo, May 2014.
- [35] M. Mikuž. *Diamond sensors for high energy radiation and particle detection*. TIPP, 2011.
- [36] W P C Mills. *The present performance of the SPS*. *IEEE Trans. Nucl. Sci.*, 26(CERN-SPS-AOP-79-9):3176–3178. 3 p, Mar 1979.
- [37] S. F. Novaes. *Standard model: An Introduction*. In *Particles and fields. Proceedings, 10th Jorge Andre Swieca Summer School, Sao Paulo, Brazil, February 6-12, 1999*, 1999.
- [38] Joao Pequenao. *Computer generated image of the whole ATLAS detector*. Mar 2008.
- [39] Heinz Pernegger. *The Pixel Detector of the ATLAS Experiment for LHC Run-2*. Technical Report ATL-INDET-PROC-2015-001, CERN, Geneva, Feb 2015.
- [40] S. Ramo. *Currents Induced by Electron Motion*. *Proceedings of the IRE*, 27:584–585, 1939.
- [41] V. Sarin. *Comprehensive Hard Materials*. Elsevier Science, 2014. p. 411.
- [42] W. Shockley. *Currents to Conductors Induced by a Moving Point Charge*. *Journal of applied Physics*, 9:635, 1938.
- [43] M. Červ, P. Sarin, H. Pernegger, P. Vageeswaran, and E. Griesmayer. Diamond detector for beam profile monitoring in comet experiment at j-parc. *Journal of Instrumentation*, 10(06):C06016, 2015.
- [44] C. Weiss. A CVD diamond detector for (n,α) cross-section measurements. PhD thesis, TU Wien, Vienna, 2014.
- [45] C. Weiss, H. Frais-Kölbl, E. Griesmayer, and P. Kavrigin. *Ionization signals of diamond detectors in fast neutron fields*. publication in preparation, 2016.
- [46] J. L. Yarnell, J. L. Warren, and R. G. Wenzel. Lattice vibrations in diamond. *Phys. Rev. Lett.*, 13:13–15, Jul 1964.